UNIVERSITY OF SOUTHAMPTON

FACULTY OF PHYSICAL AND APPLIED SCIENCES
Physics

Direct bonding dissimilar optical materials

by

Henry G. Stenhouse

Thesis for the degree of Doctor of Philosophy

May 2018

UNIVERSITY OF SOUTHAMPTON

ABSTRACT

FACULTY OF PHYSICAL AND APPLIED SCIENCES
Physics

Doctor of Philosophy

DIRECT BONDING DISSIMILAR OPTICAL MATERIALS

by Henry G. Stenhouse

This thesis presents the work conducted during this project on direct bonding of dissimilar optical materials at the Optoelectronics Research Centre, University of Southampton. It covers the history and background of the art, before progressing to the development of unique bonding processes used during the research detailed. During this project, direct bonding using chemical and plasma activation is successfully conducted on both amorphous and crystalline materials. Bonding of borosilicate glass is demonstrated in the production of planar structured fibre preforms to be caned. Development of Nd:YAG to sapphire bonds is reported, producing bonds of remarkable resilience, capable of surviving dicing and polishing procedures. Zinc selenide to diamond and sapphire bonding is presented using a plasma activated approach along with investigation of the resulting bond's limits, demonstrating the heat spreading benefits of a bonded diamond layer.

Contents

List of Figures

List of Tables

Acknowledgements

Thanks to all the colleagues who've helped me over the last four years, from other PhD students or post-docs to technicians and workshop staff. Without the support of everyone in Southampton, I doubt I could have made it through a single year.

I owe a huge debt of gratitude to Stephen Beecher, who was kind enough to guide me through much of my PhD and (hopefully) instilled at least a sliver of his endless knowledge banks in me.

A great deal of thanks are also owed to my supervisor, Jacob Mackenzie. I know I wasn't the perfect student for a laser physicist but I seem to have stumbled through successfully anyway, and that's in no small part due to your excellent guidance.

I'd also like to acknowledge the support of this project's industrial sponsor, Gooch and Housego, who supplied funding, bonding samples and their polishing expertise to the research conducted.

Thank you to all of my friends: Ryan, Jon, Amy, Jeremy, Alex, and all the rest - you know who you are. If you haven't helped my work directly, you've been there to provide support or at least some welcome distraction through board and video games. It was more than appreciated!

Thank you to my dad, Bryn, and my mum, Jenny, without whom I never would have found my feet in physics, let alone survive university and *then* a PhD. And to my sisters Sophie and Fran, who have continued to send me silly pictures or comics online to make me smile these last four years: keep them coming!

Finally, a huge thank you to my partner Charlotte, who continues to be the best person I have ever known, and one I am unquestionably lucky to live my life with. Thank you for providing the support, escape and fun I needed during some of the toughest (and hopefully grumpiest!) years of my life.

“Can it wait for a bit? I’m in the middle of some calibrations” - Garrus Vakarian

Chapter 1

Introduction

Materials bonding is an expertise of vital importance to both academic and industrial science. By uniting different mediums, the complimentary characteristics of each can be merged. With their work widely integrated into modern industry, the fields of opto-electronics and laser physics continue to push the limits of efficiency, functionality and power. To facilitate this ever changing boundary, the material physics which lays the groundwork demands equal effort to progress. Research into materials bonding is therefore focussed on expanding the viable roster of materials as well as improving efficiency either through strength, optical transmission or other desired characteristics.

Direct bonding (DB) is a technique of joining two macroscopic surfaces, without including an intermediate adhesive layer. This lack of a joining material is of notable interest to laser physics, where improving optical transmission or avoiding high-power absorption damage are crucial, as well as providing an optimal solution to heat extraction. Direct bonding is a widely applicable technique, the extent of which is still being tested. As a process, direct bonding has extensive background in the field of silicon wafer bonding [1, 2], but it can also be adapted to a range of materials through tailored activation, bonding and annealing stages.

In modern research, direct bonding holds noted interest as a method to combine the benefits of dissimilar materials, allowing direct contact between, for example, a heat-spreading layer and an active gain medium requiring cooling at higher powers. Applied in this manner, it is possible to join bulk materials such as laser crystals. On this front, direct bonding holds no dependence on factors such as lattice matching which are crucial for epitaxial growth, providing an alternate method to develop devices such as planar waveguide lasers [3, 4] or bulk, composite structures [5, 6]. However, while work on bonding of crystalline and dissimilar materials expands, the methodologies applied are not well documented.

This project aimed to develop a reliable bonding procedure at the University of Southampton before applying the knowledge to the joining of soft glasses and dissimilar materials.

Direct bonding's applicability to less conventional areas of research is demonstrated in the production of planar waveguide fibres. For this purpose, soft borosilicate and phosphate glasses which can be easily machined and polished are joined via fusing and bonding to produce planar-structured preforms. These preforms are then drawn using a fibre caning tower into planar fibres, retaining their preform design.

The iterative improvements during development are covered before demonstrating successful bonding of two distinct composite devices (YAG-sapphire bonding and ZnSe-diamond bonding).

1.1 The history of direct bonding

Direct bonding as an advanced research art has only seen the bulk of its use in the last 50 years, but its origin stretches as far back as the days of Newton. Newton observed the circular interference pattern produced between spherical and flat surfaces, now labelled Netwon's Rings. The occurrence was first noted by Robert Hooke in his book, Micrographia [7], but was (as with many of Hooke's works) attributed to Newton who took the time to investigate and explain the phenomenon in greater clarity.

The appearance of these rings remained of scientific interest for some time [8], but it wasn't until the later work of van der Waals in 1873, London [9] and eventually Hamaker in 1937 [10] that the mechanism by which two macroscopic bodies would attract was understood. Van der Waals (vdW) proposed the mutual attraction of molecules, while London detailed the appearance of transient, induced dipoles between atoms and molecules in gas (hence the dispersion force, usually the most prominent vdW interaction between macroscopic bodies is sometimes termed the London-dispersion force, or London-vdW force). Finally, Hamaker investigated the magnitude of forces between two spherical particles before extrapolating to the macroscopic scale between a sphere and wall.

Contacting of two solid materials was noted well in advance of theoretical understanding. Desagulier demonstrated in 1792 that two spheres of lead would bond when pressed together [11], albeit with great deformation. The tendency of well polished metals to stick together was termed "Ansprengen" by German workers, and found to occur similarly with glasses. In 1936, Lord Rayleigh produced the first investigative account of optical contacting [12], recording the joining of two well-polished, glass surfaces, joined after thorough cleaning and evaporation of an intermediate benzene layer.

This phenomenon did not find a wider use until the bonding of silicon and sodium-glass wafers by Wallis and Pomerantz in 1969, who joined surfaces through use of elevated temperatures and applied voltage (a technique which came to be known as anodic bonding) [13]. Since then, variants of direct bonding have largely been centred around silicon wafer bonding, introducing stages hydrophilic activation and post-bonding heat treatment to strengthen the end result [14], as well as the beginnings of work focused on the van der Waals joining of alternate materials such as GaAs layers to silicon, sapphire and other materials [15]. Comprehensive work was conducted by Gösele and Tong into understanding and improving silicon wafer bonding with regards to bond strength, activation and annealing stages [16]. DB finally found a purpose as a substitute for traditional epitaxial growth.

In 1994, Haisma *et al.* produced a more comprehensive catalogue of materials directly bondable to silica, silicon and between like materials [17], along with further progression reports in later years [18, 19, 20] and proposing ideas to expand the application for direct bonding [21]. This first study touched upon the dissimilar bonding of materials, and in recent years this has seen a more invested focus, with the umbrella of DB widening to include a multitude of techniques for dissimilar, bulk crystal bonding. It should be noted that research into non-crystalline bonding is also an active field, including investigations into the direct bonding of metals such as copper for chip stacking [22]. The bulk of modern academic research, however, is centred in photonics and optoelectronics, specifically around the joining of crystals and dissimilar materials, typically for use in active devices.

1.2 State of the art techniques

Modern day direct bonding follows a few distinct paths, but each of these is adapted based on the materials in question. No all-encompassing approach has been determined and thus for each unique bond, activation, bonding and annealing processes must be trialled to achieve the desired result. The general principles of the most commonly used techniques are discussed here.

1.2.1 Room temperature bonding (Ar-beam activation)

Currently in extensive use, the room temperature bonding process (sometimes also referred to as Surface Activated Bonding, or SAB) has been demonstrated by multiple groups, largely centred in Japan. In this approach, bonding faces are etched and activated using an Argon ion beam [23] or neutral Argon atom beam in a vacuum environment. The Ar atom beam both cleans and etches the surfaces which are then pressed together and form spontaneous contact [24]. Room temperature bonding has been achieved between silicon and silicon oxide wafers, polymers, metals and glass [25, 26], as well as crystals such as GaAs [27], BBO [6] and YAG [28]. Joining of silicon wafers through this method has achieved bond strengths high enough to allow for dicing of the composite. As the name suggests, a key benefit of the RTB technique is the lack of a high-temperature annealing stage. Through this, bonds between dissimilar materials of different coefficients of thermal expansion (CTE) can be joined.

1.2.2 Plasma activation

Another method applied to bonding of crystals and dissimilar materials is plasma activated bonding. In this route, microwave or Reactive Ion Etching plasma is used to both clean, etch and activate a surface, developing a hydrophilic surface state. Faces can then either be brought into contact directly or with application of further solution. Typically, oxygen or nitrogen plasmas are used for short time periods (1 minute or less) to avoid damaging the material used, but longer durations have been tested at lower powers [29]. However, for different materials, H_2, Ar and even fluorine plasmas have been applied to direct bonding.

Joining of bulk, dissimilar crystals (BBO and sapphire) has been demonstrated using plasma activation [30]. Cu-Cu bonding [22], silicon-quartz, silicon to diamond-coated wafers, and silicon-silicon wafer bonding [31, 32, 33] have also been demonstrated, with the later achieving strength comparable to bulk when annealed at 350°C in an N_2 atmosphere. In order to achieve bond strengths suitable for dicing between dissimilar crystalline materials, high temperature annealing stages (typically between 200-800°C) [34] are often conducted following contact. However, high temperatures can cause stress fractures between materials that differ in coefficients of thermal expansion.

1.2.3 Ultraviolet Ozone (UVO) activation

Fan *et al.* have reported UVO-activated bonding of Si wafers [35]. Bonding faces are exposed to UVO for time periods between 3 and 12 minutes to develop a hydrophilic surface state. UV is a well-established cleaning procedure [36]. High energy UV light (185 nm and 254 nm) is used to clean and activate the surface. Similar to Plasma bonding, post bond annealing is included to maximise strength.

1.2.4 Chemical activation

Depending on the desired bond and materials chosen, chemical treatment with acids and bases can act as both a cleaning and activation stage. Sulphuric acid is commonly used as a final cleaning stage for wafer bonds, and is often combined with hydrogen peroxide (3:1) to produce Piranha Etch, a volatile mixture which excels at removing organics as well as developing a hydrophilic surface state [37, 35]. Piranha etch is typically used in bonding of silicon and silicates and was applied as a final stage activation for bonding of borosilicate glass during this project.

Hydrofluoric acid has also been applied as a final activation stage to produce hydrophobic bonding [38] which may be of interest to avoid any residual water or OH at the interface. Hydrofluoric acid terminates the surfaces of silicon wafers with hydrogen and fluorine bonds which contribute to the bonding energy but typically result in a lower surface energy than hydrophilic bonds [39, 20].

1.2.5 Alternate bonding techniques

1.2.5.1 Anodic bonding

Anodic or electrostatic bonding is a well established technique for semiconductor wafer bonding, usually for joining glass and silicon wafers. Compared with most direct bonding techniques, anodic bonding desires clean, smooth surfaces, but requires a much less stringent surface roughness of $<20\,\mathrm{nm}$ RMS. Surfaces to be joined are placed into contact, then with optional pressure applied, the bonding surfaces are heated to temperatures between 300-500°C (depending on material) and a voltage between 100-1500 V is applied. This encourages the diffusion of sodium ions from the bonding interface, forming a depletion region. The bond forms as a combination of electrostatic and chemical effects, producing an SiO_2 layer in the middle. While surface requirements are reduced, anodic bonding is suitable only for a select number of materials, requires high temperatures and produces an interfacial layer.

1.2.5.2 Ion exchange & thermal diffusion bonding

Ion Exchange during annealing has been used with Direct-UV writing to produce a buried waveguide [40]. In this case, direct bonding is conducted, and then ion exchange occurs during a high temperature (350°C) treatment. An electric field is applied to encourage transfer. This develops a central, photosensitive layer which allows for UV writing. Similarly, during the annealing phase, thermal diffusion bonding uses a hot press to encourage development of a composite layer at the interface [41]. However, for the thermal diffusion process, extreme temperatures of over 1000°C were used.

1.2.5.3 Silicate bonding

The most common variant, silicate (or hydroxide catalysis) bonding, was developed for use in the Gravity Probe B space experiment [42]. It follows the same principles as hydrophilic direct bonding but includes a silicate-based solution between faces to encourage the development of siloxane chains.

Silicate bonding can be completed at room temperature and without the requirement for a high purity clean room environment. Due to the non-instant nature of bonding, alignment of samples can be made precisely. Additionally, flexure strength measurements have been shown to sometimes surpass that of the bulk material [43].

However, silicate bonding is, generally, limited to silica or oxygen based materials. Work has been conducted on bonding non-silicate, oxygen based materials such as sapphire [44]. Direct bonding holds a distinct advantage through its applicability to any material. Silicate bonding results in a ∼100 nm interface which, while small, leads to absorption losses or damage for high power applications (Sinha *et al.* recorded damage at $>70\,\mathrm{J/cm^2}$, but the threshold varies depending on the method of implementation and can be much lower) [45]. By comparison, direct bonding provides an entirely seamless interface, with no intervening bond medium. This allows for no absorption losses at the interface and, so long as thermal expansion mismatch effects can be circumvented, the capability for high power applications.

1.3 Report Summary

Following this introduction, a summary of each remaining chapter in this report is detailed. A brief overview of the content, including aims and results for each branch of the project, is provided.

1.3.1 Chapter 2 - Project methodology

In this chapter, the working methods used during the course of this research are explained. The fibre caning process including the principles of glass transition temperatures and the manual working of the fibre caning tower are covered. A brief look into alternate methods of producing a planar structured fibre is conducted.

The primary interacting forces and mechanics by which direct bonding occurs are explained, including the principles of van der Waals forces and hydrogen bonds. The intrinsic capabilities of a selection of materials for bonding are compared before discussing general principles of surface activation and testing bonds. Finally, the processes and equipment used in surface analysis and preparation are detailed.

1.3.2 Chapter 3 - Developing the bond process

This chapter details the development of a bonding procedure, from first attempts at joining borosilicate windows to fully tailored bonding procedures. Each material combination is detailed in a series of bonding trials, showing the different attempted routes. This chapter is designed to serve as a reference point for future chapters.

First, BK7 borosilicate windows are bonded using a hydrophilic approach. The successive trials are shown with efforts to improve the cleanliness of bond interface. Changes to each stage as well as the equipment used are detailed. Bonds are produced which, when annealed at 350°C, are able to survive dicing using a large glass saw.

Second, dissimilar materials bonding is discussed, with the bulk of emphasis on sapphire to YAG bonds. A selection of bonding methods are tested including hydrofluoric acid, sulphuric acid, plasma and carboxylic acid activations. The benefits and concerns for each route are discussed to identify the most suitable approach.

Finally, the up to date bonding procedures are listed, including key points of note for bonding, as well as detailed accounts of each cleaning, activation and annealing stage.

1.3.3 Chapter 4 - Planar fibre production

This chapter covers novel attempts to create a planar-structured, fibre-scale device through the production of planar preforms. First, the material of choice is characterised before a detailed record of each attempted fibre cane. These trials included preform fabrication through dicing, polishing and then fusing or bonding of glass, before draw attempts were conducted using a fibre-drawing tower.

Both preform production and the drawing process were refined through several iterations to develop a repeatable technique to output large quantities of planar devices. Initially, single segments and fused glasses were used to produce preforms before a bonded preform is tested, demonstrating a marked improvement of the interface quality. In each draw attempt, the resulting fibre is cleaved and inspected to record shape, dimensions and interface quality.

Finally, creation of an active device was attempted by sourcing a custom phosphate glass in both plain and neodymium-doped variants. Success was had in drawing a three-layered planar device to a wide spread of dimensions. Two glass batches were produced, but ultimately the intrinsic losses and inhomogeneity of the custom glass melt proved too substantial to progress this part the project further.

1.3.4 Chapter 5 - ND:YAG to sapphire bonding for active devices

In this chapter, bonding between sapphire and YAG (or Nd:YAG) is reported. The aim was to establish a bonding procedure which results in bonds resistant to high temperatures, submersion in DI water and solvents, and mechanical processing. A variety of activation methods were tested including hydrofluoric acid, sulphuric acid and plasma activation. In addition, the post-bond annealing stage was improved and tailored based on the activation method used. Each method was tested through subsequent bonding trials to establish the most suitable method.

Strong bonds were produced between sapphire and bulk YAG as well as 490 µm thick YAG windows using either hydrofluoric acid or plasma for activation. By applying an extended annealing stage at 800°C, these bonds proved capable of surviving dicing using a commercial wafer dicing machine. The bonds were tested for durability in a number of environments including water/solvent submersion and cryogenic cooling to -180°C.

One hydrophilic bond between Nd:YAG and sapphire was diced into a smaller segment before end facet polishing and coating with an AR layer of magnesium fluoride. This sample was then built into an active laser oscillator, pumped by a diode bar. The bonded composite showed no signs of damage with 27 W of incident pump power and produced over 5W of output.

1.3.5 Chapter 6 - Direct bonding zinc selenide to diamond

This chapter describes in more detail the development of a bonding process between ZnSe and diamond, two materials of vastly different physical characteristics. A series of activation methods were conducted, recording the effect on surface contact angle of de-ionised (DI) water. Eventually, plasma bonding was determined as the most suitable approach and a successful bond between 4 mm thick ZnSe and 500 µm diamond was formed. In addition, bonding between sapphire and ZnSe as well as sapphire and diamond was demonstrated.

The joined ZnSe and diamond composite was tested for temperature durability in trials between -40 and 80°C and at several different ramp rates. Failure of the bond was induced by continued heating. The subsequent inspection is discussed.

The composite was then tested in a simple heatspreading trial. Mimicking an active device, a focussed 442 nm diode laser was used to induce a localised heatload on the ZnSe surface. A probe-pump setup was positioned with overlap such that distortions in the probe beam caused by temperature increase could be recorded to calculate thermal lensing. A comparison is made between bare ZnSe and the diamond-bonded composite to show that the bond reduced thermal lensing by several orders of magnitude, reducing the thermal lens to beyond the setup detection limits.

1.3.6 Chapter 7 - Conclusion

The defining outcomes from each chapter are summarised here. Finally, proposed routes to continue and improve each project within the thesis are suggested in the Future work section.

Chapter 2

Project methodology

This chapter describes the working principles used in each area of research addressed in this project. First, the fibre caning procedure is detailed, in which the characteristic evaluation of glasses, preparation of planar preforms, pulling process and subsequent inspection are covered, along with notes on state-of-the-art research into planar fibres. Second, direct bonding, in which the relevant surface-to-surface interactions are explained, along with goals behind each method of cleaning/activation. Alternative bonding techniques are also briefly reported. Finally, the equipment and procedures used during mechanical preparation and evaluation of bonding samples are detailed.

2.1 Fibre caning

Caning represents one of the two core methods of fibre manufacture. Much like a standard fibre draw, a preform (usually glass) is held vertically within a coil furnace and heated until it softens. The glass is then pulled down and guided into a cane puller (where a standard fibre would be attached to a fibre drum). Unlike a standard fibre draw, caning is commonly used to produce fibres of larger dimensions (usually upward of ~400 µm) and a corresponding lower flexibility. The degree of reduction from preform to cane is lower than that of a standard, drum draw (caning is often used in a two draw process as a step between full preform and the final fibre draw). In this project, fibre caning of silicate glass was used to investigate the drawing of a planar structure down to fibre dimensions with interest in the retention of planar dimensions during the draw.

The process of fibre caning, much like bonding, relies on careful preparation rather than technical capability during the draw. When preparing for a cane attempt it is imperative to understand the physical characteristics of the preform material used. Detailed below are the key factors to be considered when conducting a draw.

2.1.1 Transition temperatures

Glasses transition from amorphous solid to molten liquid in a reversible process that holds key points between end states. The relevant temperatures are measured using the poise scale, which defines the material's viscosity. This is recorded in the form T^n where the higher the value of n, the more viscous the glass.

The glass-transition temperature, Tg (or T^{13} on the poise scale, indicating a viscosity of $10^{13} * 0.1\,\mathrm{kgm^{-1}s^{-1}}$), occurs at the lowest temperature, marking a change in various structural properties and reducing the viscosity of the medium. Following this, $T^{7.6}$ is the softening temperature, at which it is generally considered suitable for fusing and fibre drawing. At the other end of the spectrum lies the melting temperature, Tm, where the glass is marked to have become fully liquid. Between the softening and melting temperatures, and of paramount importance for pulling and pressing, lie various crystallisation temperatures.

The lowest temperature at which crystal nuclei can form in the glass is referred to as Tx (or Tc). Usually a slow process, crystallisation is circumvented in glass production by quenching extremely quickly past the crystallisation temperature range. However, even if successfully avoided during manufacturing of the glass, early nuclei formation may occur and form into crystals when heated to Tx subsequently.

During fibre drawing, the temperature must be kept below Tx, reducing viscosity enough to draw but without crystallising the glass. A sweet-spot temperature is usually targeted just below Tx to aid the draw as much as possible. Crystallisation can ruin entire fibre draws and is only removed by remelting. It is vital that no section of the glass is raised to near or above Tx for any length of time

When considering the values for Tx and Tg, they are often defined with arbitrary, small differences to the exact values and should therefore be looked at as guidelines rather than strict points. Each fibre drawn must be considered uniquely and adapted based on response from the glass.

2.1.2 Differential thermal analysis

If the specific values for a glass are not provided in literature, the temperature regions of interest can be identified via Differential Thermal Analysis (DTA). A small segment of the glass to be tested is heated from room temperature and measured with an especially sensitive thermocouple. An empty, reference container is also measured. Any exothermic or endothermic change in the glass container can then be identified.

Gallium Lanthanum Sulphide provides an excellent example DTA recording, with clear transitions shown in Figure 2.1, The endothermic Tg and Tm transitions are visible as a

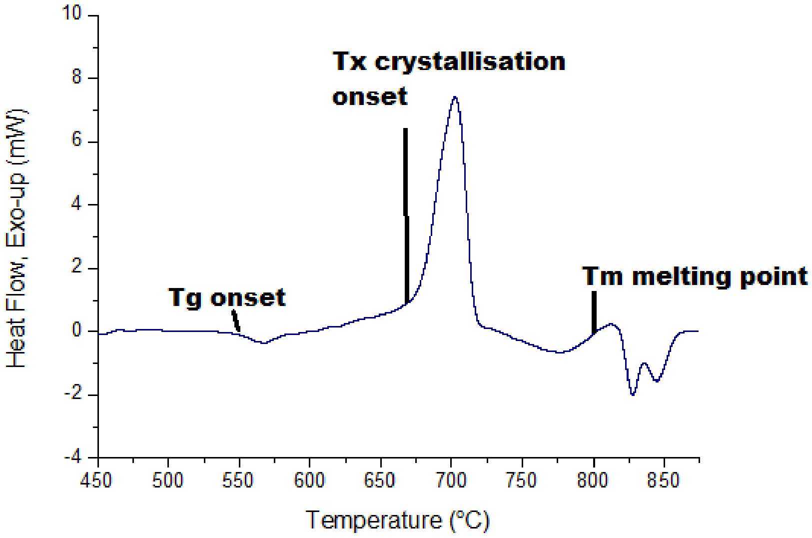

Figure 2.1: An example DTA curve for Gallium Lanthanum Sulphide glass showing a Tg onset at approximately 544°C, Tx at 669°C and Tm at 818°C [46]

small dip which onsets at approximately 544°C and a larger, double dip at around 818°C, respectively. The crystallisation temperature, Tx is seen as a tall, sharp, exothermic peak at 669°C.

2.1.3 Preform production

Once the relevant transitions are known, the fibre preform can be produced. To achieve a planar waveguide structure, multi-layered preforms are required. In this project, both fusing and bonding have been considered. The full bonding procedure is covered later in this chapter. Fusing involves raising cleaned pieces of glass slowly to the softening temperature and back down while resting on top of one another. This offers a fast and simple method but risks unreliability of interface quality (air can often be trapped within the fuse) and damage from CTE (Coefficient of Thermal Expansion) mismatch. Bonding involves a rigorous cleaning process but does not require as high temperature for the annealing stage, reducing the thermal shock risk and diffusion between layers. In both cases it is important to ensure that, if different materials are used, the CTEs are kept as close as possible. If any separation exists, even minor, the ramping temperatures for fusing and annealing must be kept low (1°C/min or less). Though no clear standards exist, this project proceeded on the principle of <5% difference in CTE was acceptable when ordering materials for fusing. Greater differences can be accounted for with lower ramp rates, however results become unreliable and prone to stress fractures.

Fusing of material within the tower had been considered, however former research at the University testing this resulted in catastrophic failure of the draw, pulling down two separate fibres without them joining.

Once the two desired pieces were fused (or bonded), the edges of the preform could then be machined again to correct any misalignment from the joining process. Notches were cut into the preform edges to allow mounting into the fibre tower for caning.

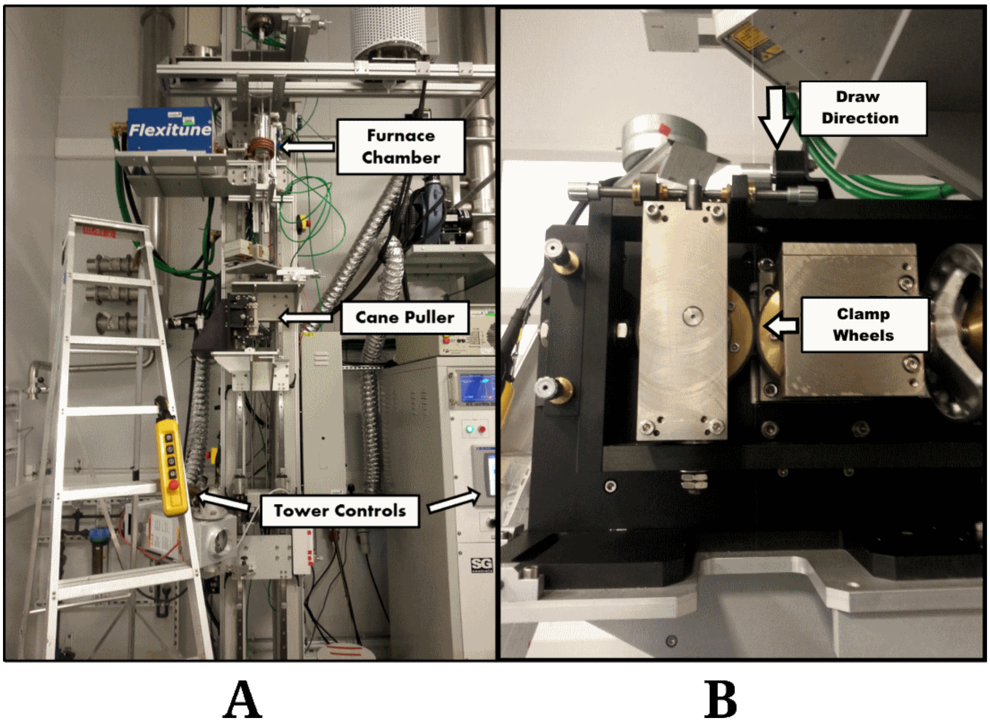

Figure 2.2: A) The fibre tower used for caning procedures and B) A side-on view of the cane puller showing the two wheels clamped onto a fibre segment

2.1.4 Caning

During caning, the tower shown in Figure 4.4 A was used. The preform would be weighted and heated in the furnace until necking (thinning of the preform width in the hottest region) was observed. The bottom end would then either drop through gravity or be drawn down by hand to the cane puller. Figure 4.4 B shows the function of the cane puller. One wheel rotates at a user-defined speed. The separation of the wheels could be adjusted according to the width of the drawn segment. The glass is drawn down from the tower above and fed into the cane puller. The wheels of the cane puller are then firmly closed onto the drawn down fibre, gripping it and pulling down at the wheel's rate of rotation. Caning is a slow process, with the puller usually running at tens of millimetres per minute, and requiring direct attention throughout.

The preform and cane puller feed rates can be adjusted before or during runs to tailor dimensions of the cane. Calculation of the dimension is based on volume conservation.

The rate of material passing through the cane puller should equal that of the preform feed such that:

$$A_P * V_P = A_C * V_C \tag{2.1}$$

Where A is the cross-sectional area and V is velocity. P and C subtexts signify preform and cane, respectively.

Assuming the aspect ratio of the sample is held during caning, the width and height of any drawn segment can be calculated from known preform dimensions.

Once the cane has been attached to the cane puller, all material drawn from the preform should be at the desired dimensions. Suitably long segments could then be broken off for investigation. In this project, lengths between 30mm to 30cm are of interest for investigation into interface inspection and testing absorption (or gain in active mediums) along the length.

2.1.5 Inspection

The priority for fabrication during this project is if the process conserves planar dimensions during a draw and produces a high quality interface for an optical waveguide. To inspect this a series of cleaves can be made along the length of a cane segment to ensure long distance quality is retained. The cross sections can be imaged by a microscope to look for any gaps or flaws throughout. Additionally, by comparison to a segment of known size, the dimensions of caned pieces can be recorded. This will allow the core thickness to be noted and adjusted for future runs depending on number of modes desired within the waveguide.

2.2 Direct bonding

The title of direct bonding belies an intricate set of chemical interactions, often unique to each material considered. While a wide number of interactions come into play throughout the bonding process, a few key molecular interactions provide the base upon which the bond develops. The principal stages of direct bonding tend to include a surface activation/cleaning stage, optical contacting and, sometimes, elevated temperature curing. Once contacted, direct bonding occurs due to range of microscopic effects, but the central, electromagnetic interactions are believed to be dipole-dipole forces (namely hydrogen bonds), van der Waals (vdW) forces and full chemical-bond chains.

In this section, the basic theoretical background to the most influential interactions in direct bonding are detailed, the relevant surface qualities required for bonding are also covered along with the techniques most commonly used during surface activation to encourage their development. The formulae detailed here are rarely used during direct bonding work, and, beyond comparing Hamaker values, will not be referred to in this thesis. However, it is important to understand the mechanics behind the interaction when applying the process to research.

2.2.1 Surface interactions

2.2.1.1 Hydrogen bonding

During the early stages, hydrogen bonds play a crucial role in encouraging and holding contact in a direct bond thanks to their longer range interaction compared to van der Waals forces.

Hydrogen bonds are an especially strong form of dipole interaction. The hydrogen atom has only one partially full 1s orbital, and as such can only form a single full covalent bond. Depending on the electronegativity between the two bonded atoms, the hydrogen atom can form an attraction to another atom or molecule. When bonded with a strongly electronegative atom like oxygen, the hydrogen electron cloud is attracted, drawing it away from the positive hydrogen nucleus. The result is an effective dipole. If two surfaces, such as those in direct bonding, are brought close together with dangling O-H bonds, the associated dipole interactions will help draw the surfaces together. This initial attraction can help draw the faces into the shorter regime of vdW forces.

Hydrogen bonds have energy in the range 0.1-0.4eV and are far weaker than covalent bonds (The Si-Si and Si-O covalent bonds often produced in bonding, have energies of 1.9 and 4.5eV, respectively) [47]. When surfaces to be bonded are made hydrophilic, any water molecules present may help produce a bridge between the two surfaces. While hydrogen bonds often form the initial contact force between surfaces, they are usually lost through evaporation during subsequent annealing stages.

2.2.1.2 Van der Waals

Van der Waal forces, despite their weak interaction energy, are often listed as the primary force of interaction behind direct bonding. Largely dependent on the quality of surface polish and cleaning, vdW interactions can provide significant levels of bond strength, combined with some unusual characteristics. The force stems from atomic-scale electronic dipoles which oscillate in synchronisation such that attraction is formed [47]. Three types of vdW forces exist:

- Keesom: Force between two permanent dipoles

- Debye: Force between a permanent dipole and a corresponding induced dipole
- London or Dispersion: Force between two instantaneously induced dipoles

Keesom, or orientation interactions [48], are due to electrostatic forces between permanent polar molecules. The angle-averaged interaction energy is dependent on the inverse sixth power of distance. Keesom interactions are temperature dependent, and only present between molecules containing permanent dipoles. The resultant force is so weak as to be insignificant when evaluating bond strength.

The Debye force arises when one polar molecule is brought close enough to induce a responding dipole in another, non-polar molecule through repulsion of its electrons. The polar nature of the interaction once again requires a medium with permanent dipoles and, while providing a much stronger force, acts on an extremely short range order. Due to the macroscopic nature of bodies to be bonded this factor has also been ignored during force calculations.

The final vdW force, London (or dispersion) interactions are present in all media, irrespective of their properties. The dispersion force arises from interactions between polarisable but non-polar molecules. Transient dipoles are formed through coupling of electron oscillations to lower mutual energy [49]. Dispersion force energy, much like Keesom and Debye, depends on the inverse sixth power of distance. However the key separating factor develops through the long range alignment of electron clouds. When considered additively, Hamaker identified in 1937 that dispersion forces could produce effects at a considerably longer range, relevant even to macroscopic bodies [50]. The consequence of each force's nature renders Keesom and Debye forces more relevant for microscopic scale gas and liquid interactions, while dispersion forces dominated in condensed, macroscopic media.

Because of their presence in all materials and long range additivity, the dispersion forces form the main basis for attraction considered in this project. Between two flat, parallel plates of infinite length the macroscopic dispersion force is measured as:

$$F = \frac{A_{Ham}}{6\pi l^3} \tag{2.2}$$

Where $\mathrm{A_{Ham}}$ is the Hamaker Constant and l is the separation between surfaces.

The Hamaker constant is therefore the main factor determining interaction strength. Unique to each bond, A_{Ham} is determined by the two materials to be bonded as well as the medium between them. Calculated through the absorption frequency and refractive index of each medium, typical values for Hamaker constants for solids lie around 10^{-19} J or 100 zJ [51]. The derivations of the Hamaker constant and the van der Waals forces are covered in detail in literature, including formulae for many forms of macroscopic interaction [47, 51, 49].

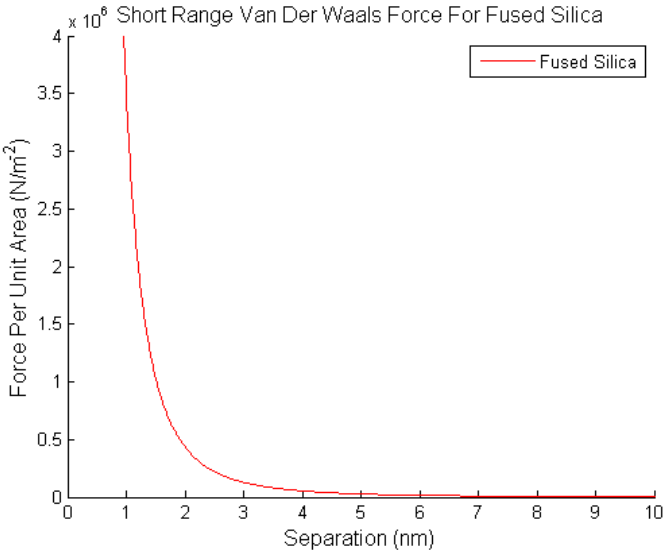

Figure 2.3: Simple model of van der Waal dispersion forces between two plane-parallel fused silica samples within a vacuum

It is important to note that Hamaker constants are not well defined for most interactions and can prove difficult to determine [52]. Studies into the calculating Hamaker constants for a variety of materials must take into account the intermediate medium and have largely been limited to approximations for silicon/silicates, with a few other select materials [53]. If values are known for like-like interactions across a vacuum, then an effective Hamaker constant can be calculated.

For an interaction of two different materials, i and j, separated by a third medium, k, the Hamaker constant can be estimated as:

$$A_{ikj} \approx (\sqrt{A_{ii}} - \sqrt{A_{kk}})(\sqrt{A_{jj}} - \sqrt{A_{kk}}) \tag{2.3}$$

In a like-like interaction (i.e. i=j) this can be reduced to:

$$A_{ikj} \approx (\sqrt{A_{ii}} - \sqrt{A_{kk}})^2 \tag{2.4}$$

Of fundamental importance to direct bonding is the short range of interaction on a macroscopic scale. In order to produce desirable bond strengths, surfaces must interact on the nanometre scale. Figure 2.3 shows the high potential strength but significant drop over the nanometre regime.

Hamaker values, and therefore interaction forces vary heavily between different materials. In general, amorphous mediums such as glass produce significantly weaker bonds than crystals. Table 2.1 lists relevant Hamaker constants, as recorded from literature [47, 54]. Diamond has a value roughly 4.5 times greater than Fused Silica. Using these values, a comparison between forces was plotted in Figure 2.4. As can be seen, fused silica sits at a notably lower level than all three crystal equivalents.

Material	A_{Ham}
Fused Silica	6.6×10^{-20} J
Sapphire	16.8×10^{-20} J
YAG*	22.75×10^{-20} J
Diamond	29.6×10^{-20} J

Table 2.1: Hamaker coefficients for like-like interactions in vacuo. Values obtained from [47] and [54] *YAG value recorded in air medium

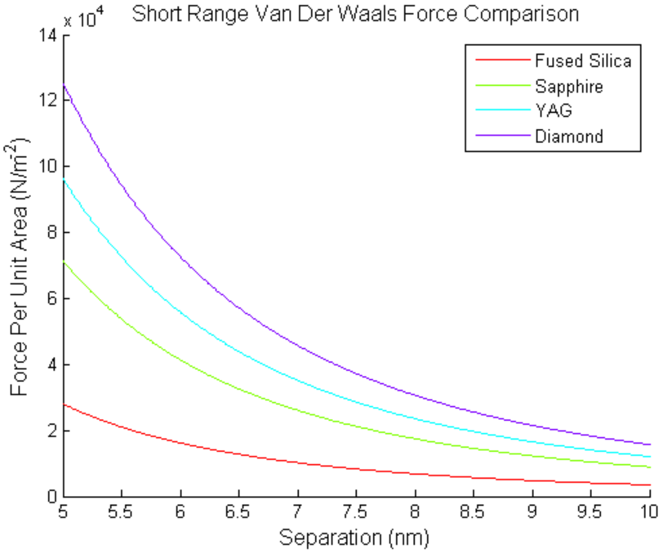

Figure 2.4: Short range comparison of vdW dispersion forces between two plane-parallel, similar samples

Extending Figure 2.4 to the range of 50-100 nm, the drop in strength is extreme. Figure 2.5 shows the strength of interaction for sapphire drop from 9000 N/m^2 at a distance of 10 nm to 9 N/m^2 at 100 nm separation. By comparison, optical adhesives suppliers typically list strengths between 0.5 and 2 MN/m^2 in shear strength tests. Though the direction for shear tests differs from the vdW forces normal to the surface, the several orders of magnitude difference is stark. It is clear then that for vdW to have a consequential impact, separation must be kept to at least under 100 nm, and ideally under 10 nm. It should be noted that while pure vdW force is much lower than that of optical adhesives, the combined strength of interactions for a completed and annealed direct bond is capable of surpassing the bulk strength of silicates.

Achieving this intimacy between bonding faces requires stringent levels of flatness and surface roughness on bonding faces. Identifying feasible materials for vdW bonding is therefore a careful balance between the potential bond strength of the medium and the difficulty in producing a high quality polish. Diamond, for example, has potential due to it having the highest known Hamaker constant but, owing to its strength, is incredibly

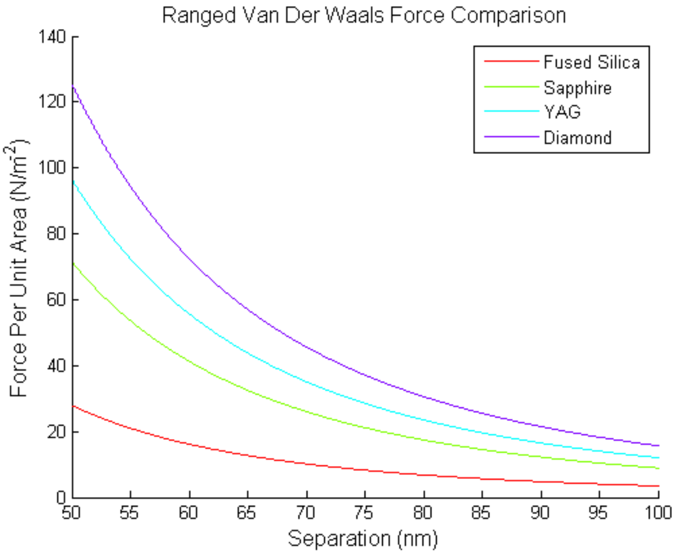

Figure 2.5: Longer range comparison of vdW dispersion forces between two plane-parallel, similar samples

difficult to polish to the desired level of precision. Investigations have been run to determine the best methods of polishing various materials types in order to acquire such a finish [18]. In general, a flatness of at least $\frac{\lambda}{10}$ (at $\lambda = 633\,\text{nm}$, over a range of 20mm) and an RMA roughness of $<1\,\text{nm}$ are desired for direct bonding.

2.2.1.3 Covalent bonds

Covalent bonds occur between atoms which share electron pairs, the bond represents the balance between electromagnetic attraction and short range repulsion of atoms. Covalent bonds represent the strongest interaction, an order of magnitude above hydrogen bonds. When measured in kJ/mol, Hydrogen bonds typically range from 5-30kJ/mol where covalent bonds can range into several hundreds on average [55]. Covalent bonds form the structural basis of bulk solids and as such, direct bonds which develop through these can produce strength results comparable to the bulk medium. Transfer to covalent bonds is encouraged during the annealing of hydrophilic bonds. Silicate materials in particular are believed to transfer from hydrogen bonds to chained siloxane bonds of a greater strength. Other, oxygen-based materials have been recorded to develop bonds in a similar manner [56].

2.2.2 Surface activation

Prior to contact, surfaces to be bonded are usually activated via chemicals, plasma or other routes to increase the surface energy, encourage surfaces to form an initial contact and improve the final strength obtained after annealing (if the process includes it). While each technique is different in application and results, most fall into one of two primary categories: Hydrophilic and hydrophobic.

2.2.2.1 Hydrophilic

The more common method, hydrophilic, encourages the growth of hydroxide (OH-) groups on the surface of each sample. Figure 2.6 shows an example hydroxylated silicate surface. During the bonding process, these dangling bonds encourage the development of linked, usually silioxane, chains during annealing, strengthening the bond into a robust, permanent hold. The effect is most prominent (for evident reasons) in silica and silicon bonds.

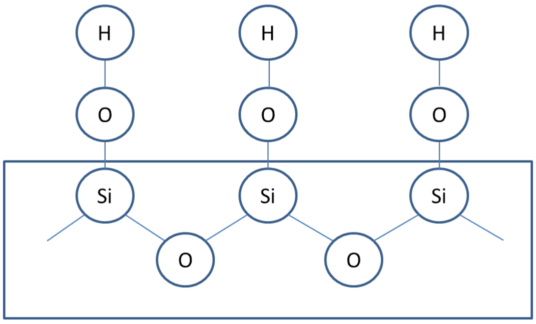

Figure 2.6: An example hydrophilic surface displaying dangling OH bonds

Hydrophilic surface activation usually involves a form of plasma/acid treatment [57, 31]. Piranha etch, a mixture of sulphuric acid (H_2SO_4) and hydrogen peroxide (H_2O_2), proves to be one of the most popular methods of cleaning prior to bonding. Used to remove organic residue, piranha also hydroxylates, leaving OH groups on the surface. These dangling groups increase the initial range of bonding forces between faces and help draw the surfaces down into the range of vdW forces. For silicon wafer bonding, surfaces joined following a hydrophilic activation typically exhibit bond energies an order of magnitude above those joined hydrophobically [39, 20]. Nitrogen plasma is also used as a method of removing impurities and increasing OH groups on the surface by bombarding the surface to open up dangling bonds of a high energy. The plasma can also produce photons in the short ultraviolet, or vacuum UV (VUV). These VUV photons are highly effective at destroying organic bonds of contaminants and breaking down structures. VUV treatment is used commonly to produce hydrophilic polymer surfaces [58, 59].

A large number of bonding investigations employ plasma activation [57, 34, 60, 61, 62] or treatment in an aqueous environment [39] shortly prior to bonding, ensuring that surfaces are as clean and hydrophilic as possible during the process. Ion beam bombardment [25] and fast atom beam smoothing [63] have also been tested as activation methods, as discussed in Chapter 1.2

Hydrophilic is, generally, the preferred method of bonding due to its ability to produce higher strength with less stringent surface requirements. The bonding can also be completed (to varying degrees of success) without the requirement for a high quality clean room environment. Due to the tightly-bound, chemical bonds it would be expected for hydrophilic bonding to produce rigid holds, with no ability for surfaces to slide against one another.

2.2.2.2 Hydrophobic

Conversely, hydrophobic activation emphasises the closure of open bonds, producing a surface repellent to OH molecules. The resultant change is a bond primarily supported by vdW forces, along with weaker hydrogen interactions depending on the surface termination. Where HF is used, surfaces can be terminated by hydrogen and fluorine atoms which interact weakly compared to OH. Alternate routes consider depositing large, terminating carboxylic molecule chains. These then interact via vdW forces with chains on the opposing surface. Additional bonding forces are provided via various chemical/-surface reactions which vary in type and strength depending on the materials bonded. Hydrophobic activations can also be strengthened via high-temperature annealing and, in the case of silicon/silicate wafer bonding, hydrophobic bond strength can exceed that of hydrophilic at the cost of a higher required temperature, as detailed in Figure 2.8 [47]. Details of the annealing process are covered in the following section.

Traditionally, hydrophilic surfaces are seen to produce the strongest bonds [39, 57] and have received the most attention scientifically in conjunction with silicate bonding. Hydrophobic bonding still holds advantages to be investigated due to its applicability to materials which cannot support the hydrophilic process and for CTE mismatched bonds. The potential to produce low stress bond interfaces is also of interest due to the lack of rigid, chemical bonds between surfaces. If a suitable hydrophobic bond could be produced, the resulting resistance to stresses induced through TEC differences could be increased. So long as the surfaces remain in close proximity, shifting relative to one other may be possible, mitigating stress fracture that would occur in a fixed bond. Moreover, the majority of hydrophobic/hydrophilic comparisons have been conducted using fused silica and silicon oxide. These materials have poor Hamaker coefficients, the primary factor determining the strength of the vdW interaction. Fused Silica, for example, has a Hamaker constant of A_{FS}=66zJ, while $A_{sapphire}$=168.7 zJ. Investigation into bonding non-silicon based materials is a largely open field. However, the majority of materials bonded using a hydrophobic approach are then strengthened using a similar process to the hydrophilic route.

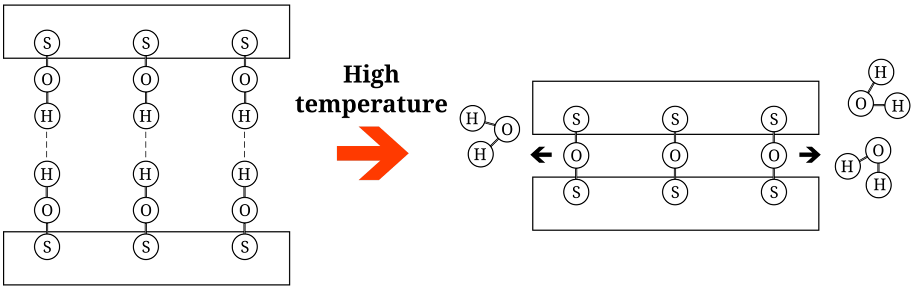

Figure 2.7: Simplified diagram showing the bond transfer for bonded hydrophilic silicon wafers when heated

2.2.3 Annealing and bond transfer

Both hydrophobic and hydrophilic bonds can be strengthened via a high temperature curing sequence. During this process, hydrogen and van der Waals interactions are converted to rigid, covalent bonds between surfaces. For a hydrophilic interaction the surface is initially saturated with dangling OH bonds. As the temperature of the bonded pieces increases, the transfer shown in Figure 2.7 begins to take place, increasing the bond strength as Si-OH - - HO-Si hydrogen bonds transfer to Si-O-Si + H_2O, forming stronger, covalent bonds [2, 64]. Bond strengthening can occur at room temperature, however the process is considerably slower and heating ensures the maximum strength can be achieved. This representation is not perfect, as surfaces will not be fully saturated with OH bonds, some regions will have purely hydrogen or alternate termination. The transfer to covalent bonds is particularly interesting considering one of direct bonding's unique selling points is a lack of lattice matching requirements. The maximum strength of an annealed bond may then depend on the capability of the two mated surfaces to form links across. This then makes strong bonding more viable for like-to-like bonds or materials of similar makeup.

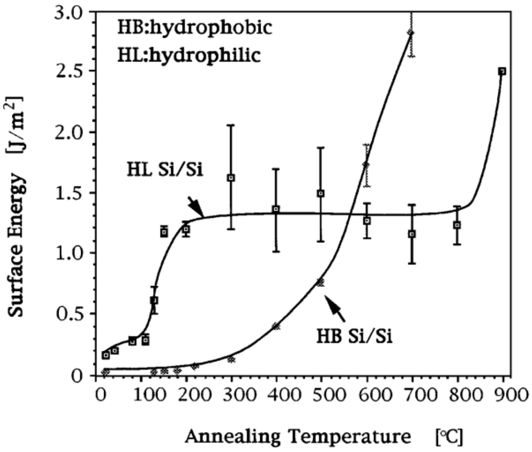

Figure 2.8: Silicon-silicon direct bond strength for hydrophilic and hydrophobic bonds with annealing temperature, demonstrated by Tong and Gösele [47]

In the case of Si-Si bonds, Tong and Gosele demonstrated in Figure 2.8 the initial higher strength available using the hydrophilic technique. When annealing at low temperatures (up to 150°C), the transfer detailed in Figure 2.7 occurs for hydrophilic wafers as silanol chains develop across the surface. Hydrophobic surfaces, however, see little change until above 200°C, at which point hydrogen and hydrogen-fluoride begin to desorb from the surface. From here the bond strength increases exponentially, overtaking that of the hydrophilic wafers. The hydrophobic bond then transfers from vdW and hydrogen/hydrofluoric terminations to direct covalent bonds between surfaces. The bond strengthening detailed by Tong and Gösele was used during this project to determine annealing approaches for both silicate glasses and dissimilar materials, with high temperatures of 800°C applied to the surfaces treated with hydrofluoric acid. The borosilicate glasses, however, required only an annealing temperature of 350°C to reach a suitable strength for machining.

2.2.4 Strength Comparisons

Strength or bond energy comparison has not been conducted during the research detailed here due to sample incompatibility or lack of dedicated machinery. However, understanding the methods by which strength testing is conducted on bonded samples is important to further understanding of different techniques. As such, the key strength testing methods used in literature and suggested for future work (see Chapter 7) are detailed here.

General testing procedures often include a four point flexure test, in which a bonded sample is held horizontally and bent by pressure applied either from above or below. Figure 2.9 shows an example set-up. Pressure is applied from above through two ball point contacts either side of the bond. The sample is flexed to breaking point, at which point the maximum applied force is recorded.

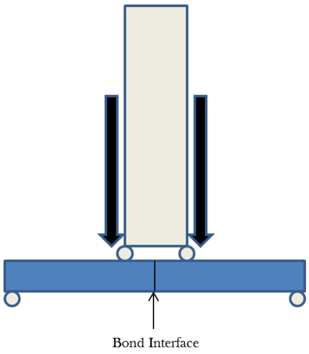

Figure 2.9: Example design of standard four-point flexure strength test, with the two bonded samples in blue and the pressure applied from above

Unfortunately, most direct bonding investigations involve dimensions which do not support testing through this method. bonded samples such as wafers tend to have large dimensions in the bonding plane and are relatively thin in the alternate dimension.

An alternative method, the razor blade strength test provides a rough measurement of bond energy for wafer bonding. In this case a razor blade is inserted between two bonded wafers. The interface will separate until an equilibrium is reached between the bond force and bending forces from the insertion. The bonding energy can then be calculated via:

$$\tau = \frac{3Et^3y^2}{32L^4} \tag{2.5}$$

Where E is the modulus of elasticity, L is the crack or bond separation length, t is wafer thickness and y is the blade thickness [2].

However, this method has been recorded only to provide a rough measurement. The manual insertion of the blade limits the accuracy of reproduction. Additionally, as with the four-point flexure test, the method irrecoverably damages samples tested, making it a poor choice for experiments in which sample numbers are limited. Bonds which exhibit too high a strength will also be prone to crack or reject the blade, destroying the sample without providing a measurement. Finally, asymmetrically-sized or larger samples make insertion of the blade and measurement of bond separation difficult.

In literature, a variation in bond strengths has been recorded. Hydrophilic bonds between thin, cleaned fused silica wafers were recorded by Spierings *et al.* [39] to have typically exhibited surface bond energy in the range of 0.05-0.2 $\mathrm{J/m^2}$. Hydrophobic bonds of the same kind were recorded to have an order of magnitude lower bond energies. This result is unsurprising considering fused silica's low Hamaker constant. In a more recent study, Kalkowski *et al.* recorded energies ranging from 0.8 - 2.3 $\mathrm{J/m^2}$ for $\mathrm{SiO_2}$ and Ultra Low Expansion glass (a low thermal expansion coefficient silica glass) when prepared using a nitrogen plasma [65].

Little research has been conducted on a direct comparison between direct bonding and methods such as silicate bonding. Silicate bonding strength tests have largely been conducted using the flexure test method described previously or a shear method. Silicon-silicon bonds at room temperature have been shown to have a characteristic flexure strength of $\sim$36 MPa at room temperature. Silicate bonds have been shown to occasionally surpass the bulk strength of the material [43]. Silicate bonding provides to closest approximation to the hydrophilic side of direct bonding due to the similar nature of both procedures. It is expected that hydrophilic bonding should produce strengths similar to those measured in silicate bonds. The lower bond energies recorded in hydrophobic bonds would indicate a lower bond strength for this process.

When compared to standard optical cements, direct bonding holds an advantage in the lack of absorption at the interface. Most optical adhesives show a significant reduction in transmission over a wide wavelength band. While strengths of traditional adhesives are high, typically supplied as shear strength in the range of 50-200 MN, they also suffer from quality deterioration over extended time frames, are thicker so have a greater separation between bond surfaces and are prone to thermal shock or other physical factors like water resistance [66].

For the research covered in this thesis, practical strength of bonds was tested via mechanical processing such as dicing across the bond interface. While this doesn't provide a qualitative assessment of bond strength, the limited number of samples available for testing made a rigorous strength testing procedure impractical. The bond was also largely conducted between two materials of differing dimensions, making the wafer-based Maszara crack method unsuitable. A custom shear bond strength device was proposed but ultimately fell outside the time-scale of this project.

2.3 Additional processing

2.3.1 Polishing

Samples used for direct bonding during these projects were polished to the required standard through a selection of techniques. Polishing standards for bonding samples were set to a root mean squared roughness <1 nm, with a flatness $\frac{\lambda}{10}$ (where $\lambda = 633\,\text{nm}$) across the area of interest. Details on these specifications are covered in Section 2.3.2.3.

In-house polishing was not used for most bonding samples, relying instead on commercial suppliers. However, during the production of fibre preforms, glasses were polished in-house using a cast iron lapping plate, with incremental stages using polishing slurry of decreasing size. First, a 9 µm slurry is used to reduce the sample to the desired thickness, second a 3 µm slurry is used before a final 1 µm slurry for fine thickness control. At each stage, it is ensured that the sample is worn down by 3x the diameter of the previous slurry particle size. This ensures that subsurface damage inflicted while lapping with the larger grit size is removed before fine polishing. Following lapping, chemical polishing is achieved using Logitech Syton on a polyurethane polishing pad.

Commercial polishing was conducted on BK7 and YAG/Nd:YAG by Gooch & Housego Ltd. using their superpolishing technique, and for ZnSe by Crystran's polishing process. Further details can be obtained from the supplier's websites:

`https://goochandhousego.com/capabilities/precision-optics-capabilities/superpolishing/`

`https://www.crystran.co.uk/tour-of-crystran-ltd/lapmaster-polishing-department`

2.3.2 Surface inspection

In order to ensure surfaces are suitable for direct bonding, surface inspection of all bonded materials was conducted in house to measure local roughness and obtain surface maps. Surface inspection was largely conducted using a ZeMetrics ZeScope Optical Profiler, as well as a KLA Tencor P16 Stylus Profiler and Nikon LV100D Microscope.

2.3.2.1 Optical profiler

The ZeScope Optical Profiler is a non-contact, white light interferometery profilometer. It works by splitting a beam of light down two paths. One path reflects the light off the sample surface to be inspected while the other reflects of a reference flat. When the path difference to the sample and reference flat is near zero, interference fringes become visible on the surface. With the sample surface adjusted to be flatly parallel relative to the reference, height levels can then be inferred through induced path differences. The Zescope white light interferometer is capable of both 2D and 3D surface profiling, with Angstrom resolution. The technology has capabilities for longer range flatness measurements, including the ability to stitch together individual surface maps to form a larger image. However, artificial curvature was noted when images were stitched, voiding attempts to record long-range height shifts. It is believed that this was encountered because the level of flatness of samples inspected was close to the flatness of the reference sample itself. With this high level of polishing, any curvature present in the reference sample would affect the recorded results.

2.3.2.2 Stylus profiler

The stylus profiler is a contact profilometer. 2D surface profiles are recorded by dragging a needle tip across the surface. The needle is joined to a flexible arm allowing it to rise or lower with changes in topology. Shifts in height are recorded in a line based on movement of the tip. The resolution of the equipment used was listed as small as several Angstroms, but due to machinery in the cleanroom environment a background noise of ± 20 nm was present. Figure 2.10 shows an example stylus profile reading across the edge of a thin film on highly polished BK7. A base noise level of over 20 nm is visible, including a lower frequency oscillation. Stylus profile measurements were largely used to confirm readings taken on the white light interferometer. As an optical technique, the interferometer is susceptible to local changes in refractive index or incorrect reading when measuring thin samples. It is possible to focus on a subsurface layer during alignment, or for different domains in polycrystalline materials to incorrectly give the impression of changes in height. The stylus profile then offers an alternative, physical confirmation.

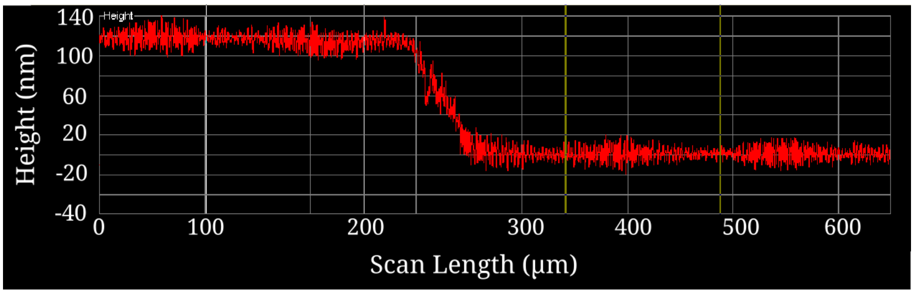

Figure 2.10: A stylus profile recording across the edge of a thin film deposited on BK7

2.3.2.3 Surface quality conventions

Surface quality is defined using a selection of measures depending on the desired end state when ordering materials. The naming conventions for these are defined here.

$\mathrm{S_q}$, $\mathrm{S_a}$, $\mathrm{R_q}$ and $\mathrm{R_a}$

The primary method for quantifying surface quality in this report is local, root mean squared (RMS) roughness. RMS roughness is the square root of the mean of the distance, $\mathrm{Z_i}$, from the mean surface level, squared - as shown in Equation (2.6). $\mathrm{S_q}$ refers to the RMS roughness for 3D surface maps, while $\mathrm{R_q}$ refers to 2D profiles.

$$RMSRoughness = \sqrt{\frac{1}{N}\sum_{i=1}^{N} Z_i^2} \tag{2.6}$$

Average roughness, $\mathrm{S_a}$ (and $\mathrm{R_a}$), is also commonly used in polishing specifications, and is simply the average of the absolute variations in surface height from the mean. With no large deviations, the values will be very similar. However, $\mathrm{S_q}$ is far more responsive to large holes or bumps, scaling much faster than $\mathrm{S_a}$. Due to the sensitivity of bonding to spikes $\mathrm{S_q}$ was used during this project. It's important to note that the recorded value of $\mathrm{S_q}$ changes depending on the machine used and lateral resolution of the image recorded. Thus, there is no 'true' value of RMS roughness [67]. For this project the localised roughness was of prime interest. Because of this and the artificial curvature detailed previously, surface roughness was recorded at the highest magnification available (100x).

Flatness is defined by overall height shift across the sample (peak to valley), and displayed as by the fraction of a chosen wavelength (typically shown as, i.e. $\frac{\lambda}{10}$, where $\lambda = 633\,\mathrm{nm}$). Alternative measures of surface quality include Scratch/Dig and total thickness variation (TTV), however Scratch/Dig provides specifications for damage on a far larger scale than is tolerable for direct bonding and can be misleading due to different definitions across the globe. TTV serves as an alternate and less commonly used definition of flatness. As such, RMS roughness and flatness (based on wavelength) were used during this project. Alternate specifications methods include the ISO-10110 standard in which a surface can be categorized based on the area of a surface covered by imperfections of a chosen size. The ISO standard offers a potentially superior method of defining surface quality, but is not commonly used as a polishing standard in industry and as such are not referred to within this thesis.

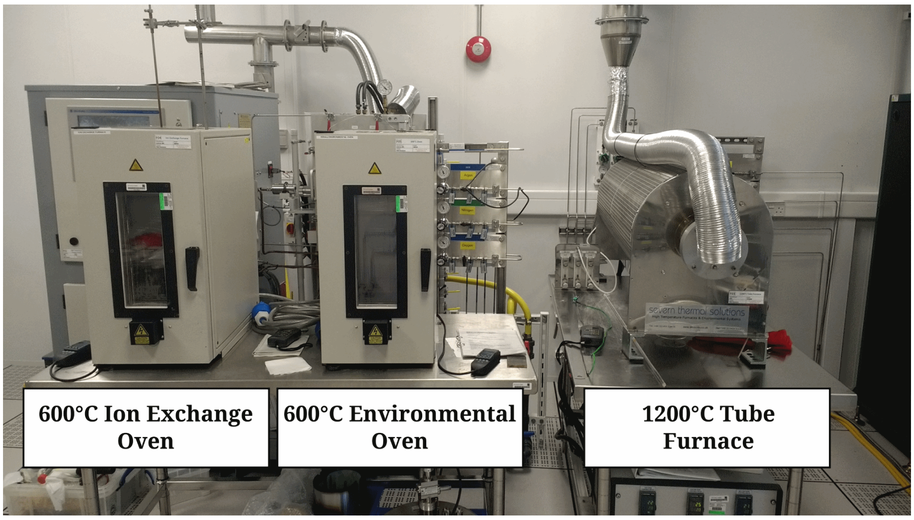

Figure 2.11: The ovens and furnaces used during this project

2.3.3 Annealing

Following bonding, most activation techniques used in this project involve an annealing stage at raised temperatures. These were conducted in a 1200°C tube furnace, 600°C environmental oven or 1200°C muffle furnace. The environmental oven was located in a clean room and offered the simplest and quickest method for annealing, at the cost of a limited temperature range, less controlled ramp rate and lack of control over the environment. A clean room environment is not essential for the annealing stage, but ensures samples remain clean during the full bonding process and did not require transfer between lab environments. The tube furnace was most commonly used due to its higher maximum temperature (required for certain bonds) and the ability to control the annealing atmosphere by flooding the chamber with Argon, Nitrogen or Oxygen. In this project, Argon was used to provide an inert environment. Finally, the muffle furnace was a large-scale environmental furnace not contained in a clean room environment. This unit was typically only used for follow-up annealing after the primary anneal was conducted in the clean room. The clean-room situated furnaces are shown in Figure 2.11. An Ion exchange furnace (identical to the 600°C environmental oven) was also used for a potassium exchange into Borosilicate, BK7 glass during Chapter 4.

These furnaces allowed for slow ramping at rates of degrees per minute to high temperatures which could be maintained for tens of hours. For faster heating processes, hot plates and a rapid thermal annealer (RTA) were used. The RTA was capable of heating at tens of degrees per minute.

Chapter 3

Developing the bonding process

3.1 Introduction

This chapter covers the progression of direct bonding capabilities over the course of this project, with the goal of developing repeatable, tailored activation procedures for a number of different materials. The focus of exploration within this project has been directed towards bonding silicon-based, soft glasses and a selection of crystalline materials. Each stage of the bonding process was refined through iterative improvements to both treatments and equipment. This chapter details the step-by-step route to creating each bond type, starting with like-to-like bonding of borosilicate, BK7 glass, then sapphire before progressing to dissimilar materials bonding with YAG, diamond and ZnSe.

BK7 is a“soft” borosilicate crown glass (produced by Schott AG) with common use in optical devices. BK7 was chosen due to a combination of desired traits, low-cost and availability. As a soft-glass, BK7 is easy to polish well, softens at a low temperature has a generous range between its transition temperatures, making it extremely hard to crystallise. As a widely used glass, the characteristics are detailed well by the supplier. While they possess a low Hamaker value, silicon and silicates have been tested rigorously with success in the history of direct bonding [18, 2, 64], offering the easiest test for hydrophilic activation processes.

Sapphire is commonly used in active laser devices as both a gain medium (Ti:sapphire) and heat spreader. It forms the basis of crystalline trials in this project thanks to its large Hamaker coefficient coupled with a high standard of polishing and relatively low cost. Sapphire and diamond offer heat-sinking capabilities courtesy of their high thermal conductivity, while YAG and ZnSe were chosen as potential host media suitable for active waveguides, amplifiers and lasers. The progress from initial tests of direct bonding to unique approaches tailored to the chosen materials is described in this chapter.

3.2 Bonding apparatus

Direct bonding was conducted with dedicated equipment which was adapted during the process to combat any problems encountered. The bonding apparatus is shown in Figure 3.1. The beakers are used for solvent and acid cleaning stages, with the glass beaker used for solvents, while the PTFE is used for hydrofluoric acid. The petri dish holds samples during plasma ashing. The vacuum chuck is used for handling samples of shape or size that prove difficult to manipulate with tweezers, and can be used to bring bonding faces into contact. The micropipette allows a precise quantity of water to be deposited. The pipette is used during contact angle trials as well as to apply droplets of water to activated surfaces prior to bonding. PEEK-tipped tweezers are the primary method of manipulating samples, minimising direct contact and providing resistance to aggressive acids. Finally, a number of sample holders (both commercially available and custom-made) allow cleaning and activation of a variety of different sample shapes and sizes.

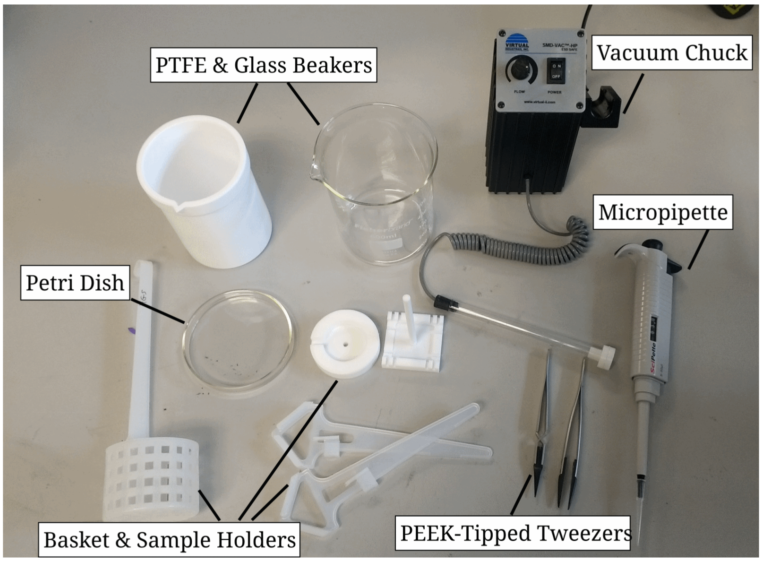

Figure 3.1: Dedicated direct bonding equipment

In addition to the preceding equipment, certain machines formed a core part of the bonding procedure. Figure 3.2A shows an ultrasonic bath used during solvent cleaning stages. The cleaning beaker (filled with a selected solvent or water) is placed in the bath and agitated for a set time period. Plasma activation was introduced during evolution of the bond process. Figure 3.2B shows the Tepla plasma asher used.

3.3 BK7 bonding

Preliminary bonding trials were conducted using borosilicate, BK7 glass. A series of trials were conducted bonding two polished BK7 samples of dimensions ∅36 mm x 5 mm.

Figure 3.2: A) An ultrasonic bath used during solvent cleaning stages, and B) The Tepla Plasma Asher used during plasma cleaning and activation

Based on the superior initial contact strength recorded previously for silicon and silicate wafer bonding processes [16], the early bonding attempts were centred around developing a hydrophilic activation procedure which would produce a reliable contact and clear interface between each sample. Later in the project, bonding was attempted using 50x50 mm BK7 pieces using the same process.

3.3.1 Surface inspection

The ∅36 mm x 5 mm, polished BK7 samples were finely polished on both faces to achieve the best quality for direct bonding. The edges of all bonding samples were chamfered to ensure edge curvature or lips could not deter bonding. The surfaces were inspected using a white light interferometer and found to have an RMS roughness of <0.5 nm for each sample. Figure 3.3A shows two surface profiles captured at 10x magnification. The fluctuation in surface height is seen to be contained to within ±1 nm. The local RMS roughness at this magnification was measured as 0.32 nm. Figure 3.3B shows the associated histogram from the surface inspection. The excellent polishing standard of these surfaces was deemed suitable for bonding. 50x50x5 mm BK7 square blanks were also inspected via white light interferometer. While the local roughness was found to be suitable (RMS 0.34 nm at 50x magnification), issues were noted with the longer range flatness of these samples when bonding. Repeated bonding attempts saw the central region fail to bond each time, indicating the surfaces curved away from each other.

3.3.2 Bonding trial 1

The first set of BK7 samples (∅36 mm) underwent a three stage solvent clean of acetone, isopropyl alcohol (IPA) and de-ionised (DI) water, followed by a cleaning and activation stage in Piranha etch. The DI water used in the clean room was of resistance 18.2 MΩ. The process conducted is detailed below:

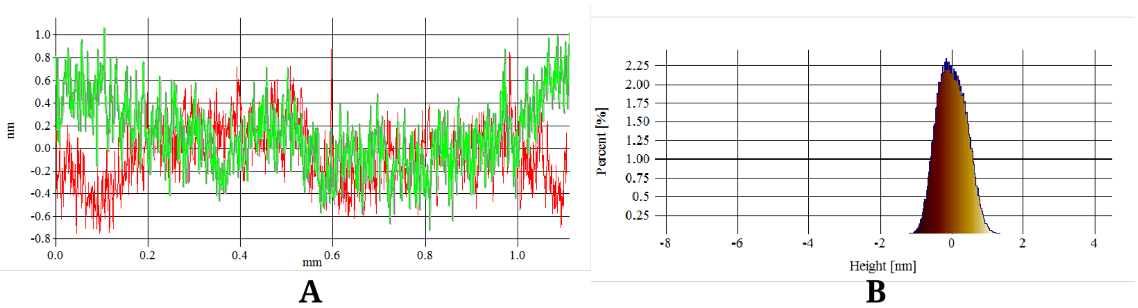

Figure 3.3: A) Two surface profiles of the BK7 surface captured at 10x magnification and B) A histogram showing the spread of surface height about the average. The surface fluctuation is within the range ±2 nm

- DI water rinse
- 10 minute ultrasonic IPA bath
- 10 minute ultrasonic acteone bath
- 10 minute ultrasonic DI water bath
- Inspection by eye under white light to ensure clean surfaces
- 20 Minutes Piranha etch
- DI water rinse
- Nitrogen blow dry
- Faces brought into contact

Ultrasonic solvent cleaning acts to remove large organic contaminants from bonding surfaces through agitation and dissolution. Piranha etch, a mixture (3:1) of sulphuric acid (H_2SO_4) and hydrogen peroxide (H_2O_2) has been proven an effective cleaning process for organic residue, but also acts as a hydrophilic activation stage, encouraging the development of Hydroxyl groups across the surface. Due to the aggressive nature of Piranha etch, samples were inspected before and after the acid stage to ensure no increase in roughness occurred. Following the initial BK7 trials, the IPA and acetone stages were reversed to improve the process. Acetone provides the strongest cleaning stage, but can potentially leave residue not easily removed by DI water. IPA is effective at removing small traces of acetone, and in turn can be removed via rinsing with DI water.

During the cleaning of multiple samples, two BK7 pieces were contaminated and deemed unsuitable for continuing the full process. These were instead placed into contact following a rinse with IPA and DI water to see if a bond could be produced despite the surface contamination. Optical contact was formed across roughly 50% of the surface (by-eye inspection), as shown in Figure 3.4.

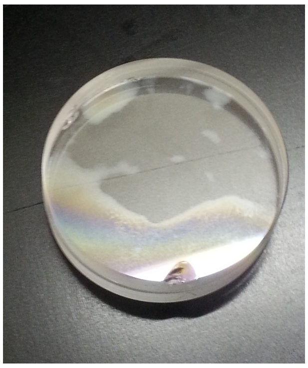

Figure 3.4: Optically contacted BK7 samples. Contact is formed over roughly half the interface, with interference fringes visible in the separated half. A large number of voids from contaminants are visible

The remaining samples completed the full cleaning process and were contacted by hand. Manual handling of samples proved difficult with full personal protective equipment (PPE) and led to poor alignment of samples. Spontaneous contact occurred in all cases and, due to the immediate strength over a wide area, samples could not subsequently be manipulated into better alignment. Attempts to do so resulted in damage to the samples and further contamination of the bond. One bond was attempted without a final nitrogen dry, to test if bonding could be completed with a water interface, following previous experience at the university. However, even with applied pressure no contact was formed and these samples were abandoned for this bonding trial.

3.3.3 Bonding trial 2

To improve handling of samples at the final stage, a vacuum chuck (as shown in Figure 3.1) was introduced to the bonding procedure. Following the final DI water rinse and nitrogen dry, the back faces of the BK7 were placed on the vacuum chuck, allowing for improved positioning of the bond during contact. Two pairs were successfully bonded, though contamination issues were still present during the transfer from drying to the vacuum chuck.

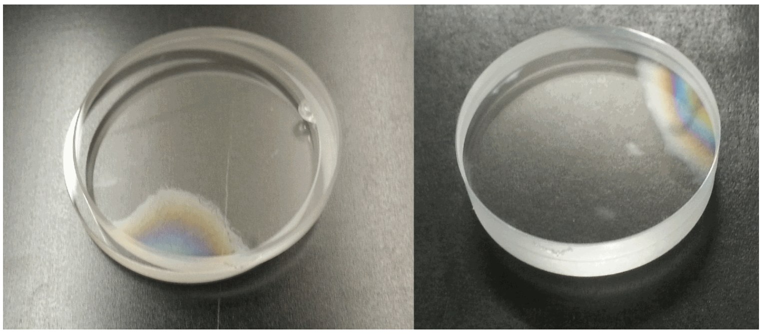

Figure 3.5: Direct bonded ∅36 mm BK7 windows. The first bond shows poor alignment and both exhibit regions with interference fringes

Figure 3.5 shows two BK7 bonds completed in the second bonding tria, with roughly 80% of the bond interface appearing clear. The interface is largely clear in both samples, but large regions with interference fringes are clearly visible in each, originating from water allowed to infiltrate the bond layer and intersperse contaminants. Reduction in these separated regions was improved gradually over the course of the project through both improvements to the procedure and capability in handling the samples before contact.

The samples were weighted under roughly 2kg for 24 hours before transfer to an environmental oven. The samples remained weighted while oven temperature was ramped to 350°C at 5°C/min. A dwell time of 20 hours at peak temperature was conducted before a 10°C/min cool. Inspection post-curing showed a significant decrease in bond visual quality, with large areas of debonding developing with interference fringes. It is possible that water trapped within the bond had expanded, separating the surfaces as it travelled to escape the bond. One sample remained largely intact, with a clear bonded area. The second bond, with a larger void, deteriorated severely, though the bond still held.

The transfer from hydrogen to covalent bonds detailed in Chapter 2.2.3 occurs slowly at room temperature, but is significantly expedited through high-temperature annealing, at the risk of developing an increased number of voids at the interface. Water can diffuse through the amorphous silicate bulk, but the process is believed to be slow. When heated, it is believed that surface tension and pressure from the closing bond around can force water together which, when evaporating in bulk, forms voids which separate the faces.

3.3.4 Bonding trial 3

Two further bonds were conducted using the same procedure, with a focus on improving the alignment and cleanliness of samples. As shown in Figure 3.6, the resulting bonds showed drastic improvements in clarity at over roughly 95% clarity across the interface. While each bond still had some voids visible at the interface, the size and number had been reduced. Due to difficulty capturing clear images of the voids present, the main points are highlighted. After 24 hours at rest, a number of additional, small voids had once again developed in each bond.

Annealing in an environmental oven was conducted once more, raising the max temperature to 360°C and annealing time to 24 hours. Temperatures above 300°C were chosen because the conversion from OH groups to Si-O-Si bonds occurs primarily in this region as H_2O disassociates from the surface [2]. An annealing time of 20-24 hours was found satisfactory to achieve bond strength sufficient to survive dicing. Inspection after oven treatment revealed a further increase in voids. To avoid concerns that contamination may enter the bond during the annealing stage, future annealing stages were transferred

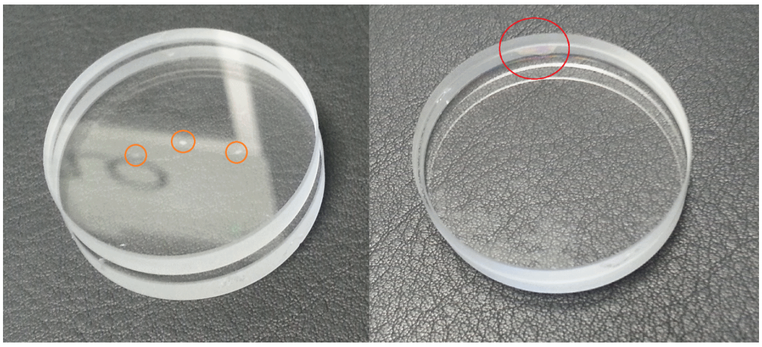

Figure 3.6: Direct bonded ∅36 mm BK7 windows. The first bond shows poor alignment and both exhibit small regions with interference fringes

from an environmental oven to a tube furnace with a controlled atmosphere of pure argon. It was also determined that for alignment-critical work, a custom alignment jig would be required to ensure correct positioning of the bonding faces.

3.3.5 50x50 mm BK7 Bonding

Three attempts were conducted to direct bond BK7 of larger dimensions. Despite suitable local RMS roughness, each attempt to bond the BK7 proved unsuccessful. While an initial contact was formed between each face, a large central void was present in all cases, as is visible in Figure 3.7. The repeated appearance of this central gap, with a circular interference pattern indicated curvature of the faces, blocking the bond from forming a close enough contact anywhere but the edges. This was confirmed via interferometer inspection of the centre of the samples. Bonding faces were found to have concave curvature. Attempts were made to encourage this central region to bond by lowering one face onto the other such that the edges were placed into contact first, the upper sample was then lain down across the lower to create a contact wave across the surface from one side to the other and stop air/liquid from being trapped in the centre. Unfortunately these efforts were to no avail. When annealed, the bond detached in each case.

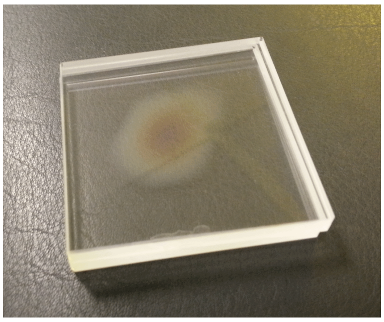

Figure 3.7: Contacted 50x50 mm BK7 blanks. A central void is visible displaying a circular interference pattern

As the edges proved a contact was possible, an alternate approach was tested. One 50x50 mm piece was then diced into 16x50 mm sized pieces, and the two edge slabs were bonded to the face of one of the 50x50 mm squares. Bonding faces were inspected following dicing to ensure no damage was caused. The dicing process caused damage only to the lower edge during cutting, and so it was ensured that the bonding face was protected by facing it upwards. While the edges were not given a new chamfer, no raised lip was visible on the bonding face edges which were diced.

Bonding was successful in this case, with the resulting sample shown in Figure 3.8. Some voids are still present at the interface, but the bond showed no central void and survived annealing. From this trial it is clear that ensuring long range flatness of samples is paramount to success in direct bonding large samples, though unfortunately the capabilities for this were not available on-site during this project. Should larger surface areas be required for bonding, flatness specifications must be stressed in sample orders, ensuring they are strictly adhered to. A peak to valley flatness of $<\frac{\lambda}{5}$ @633 nm was listed on all purchases. One method to compensate for large area bonds would be to reduce the thickness of the samples. Given a material with enough plasticity, thin samples can offer a degree of flexibility which will compensate for a difference in flatness, bending slightly to accommodate curvature. However, this would run the risk of fracture for brittle materials.

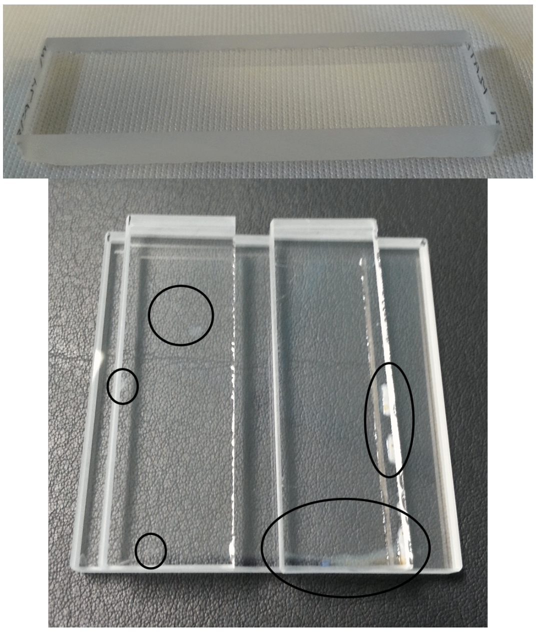

Figure 3.8: A diced, 50x16 mm sample, prepared for bonding, and two such pieces bonded to a 50x50 mm window. Voids in the interface have been highlighted for clarity

3.3.6 BK7 bond dicing

To test the durability of the bonds, a ∅36 mm BK7 bonded sample from the third trial, shown in Figure 3.6, was diced using a 150 mm diameter, 1 mm thick glass saw. The bonded samples were clamped and manually translated into the saw blade. Despite the aggressive procedure, the bond held securely, and was diced centrally into two pieces. The dicing process induced notable damage to the bottom face as the cut was completed, resulting in a large chip at one corner. This occurred through no fault of the bond, instead fracturing the bulk BK7 due to the high stress in a small area as the blade completed the cut.

In addition, one bond from the second trial was also diced, with the intention of cutting directly through a large void. Unfortunately, the loss of material during dicing (owing to the thickness of the blade) made it difficult to judge the previous position of the void. Again, no break in the material was visible.

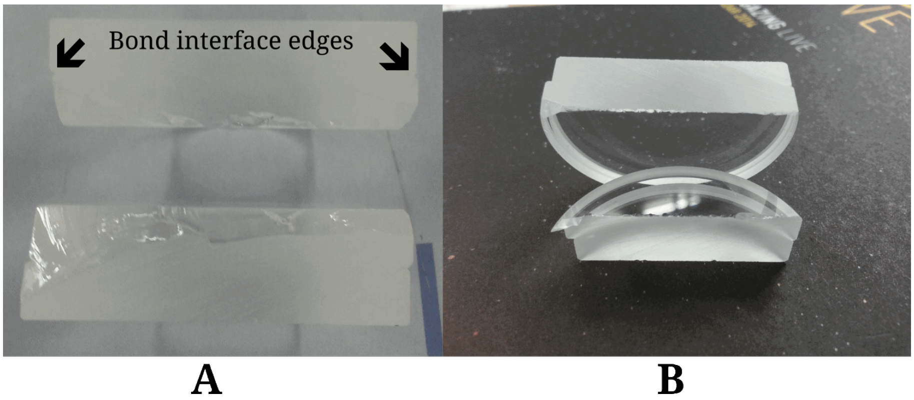

Figure 3.9: A) A top down view of a diced BK7 bond, large chip damage is visible along the bottom face, and B) A BK7 bond diced across a void

As shown in Figure 3.9, the diced samples reveal a homogeneous facet, with no clear line of the bond interface visible to the naked eye on the grey, cut surface. The point at which the faces were joined is visible through offsets at either edge, but following annealing, the two samples have effectively become one.

Figure 3.9A shows the damage caused to the bottom face during dicing, with a large chunk torn from the exit-edge. The damage caused during the dicing process was found to largely depend on the speed at which the sample was diced. By slowing the rate down, the damage induced was significantly reduced for the second dice shown in Figure 3.9B. The survival of bonds through invasive dicing procedures is testament to the strength of the bond produced.

3.3.7 Analysis

Through iterative trials, a hydrophilic bonding process had been established for borosilicate glass, achieving a strong, resilient bond with an interface clear to over 95% by eye inspection. The improvements in each stage are apparent through the reduction of contaminated regions and voids within the bond interface. With an initial basis formed for bonding, trials for crystalline and dissimilar materials could begin.

3.4 Dissimilar materials bonding

To develop the bonding technique to incorporate dissimilar materials, YAG and sapphire were chosen as materials for the initial trials, before testing bonding using diamond and ZnSe at a later stage. Bonding was first conducted between ∅12.8 mm x 4 mm thick Nd:YAG and a segment of a 660 µm-thick sapphire wafer. The Nd:YAG was recorded to have an RMS roughness of <1 nm, while the sapphire was <0.5 nm.

3.4.1 Hydrofluoric acid activation

Initially, the intention behind the dissimilar materials bonding process was to develop a transient, vdW-held bond, where each surface is able to slide over the other, as detailed in Chapter 2.2.2. The initial approach was based on HF-activated, hydrophobic bonding of silicon and quartz wafers [38, 68], whereby a low concentration of HF is used to etch the surface layer of the material, leaving dangling hydrogen and fluorine bonds on the surface. When brought into close contact, the bond would then be primarily held by van der Waals forces. Early trials were conducted between Nd:YAG and sapphire. The full development of the YAG-sapphire bond is detailed in Chapter 5.3. This section will focus on changes to the activation stage and the mechanics behind each improvement.

During this stage of the project, a plasma asher was made available, and was subsequently added to all processes as an additional cleaning stage. While plasma can act as a final bonding activation stage in its own right, its purpose within these alternate techniques was to provide additional removal of organics. Following a full solvent clean, Nd:YAG and sapphire samples were first cleaned in O_2 plasma for 1 minute, before being transferred to a 1% HF bath for ten minutes. HF can aggressively etch many materials, causing damage to the surface it contacts. In this case, the aim was only to only clean and etch the very top layer of the material, leaving dangling bonds, so treatment time was kept short. surfaces of both materials were inspected following HF treatment and found to show no deterioration in RMS roughness.

Several YAG-sapphire bonds were completed using HF activation, as shown in Figure 3.10. The interfaces were clear over roughly 90% of the interface, but had several voids present. These first stage samples were then ramped to 350°C at 3°C/min and annealed for 8 hours before ramping to room temperature (RT) at the same rate. However, when tested for resistance to liquid submersion and ultrasonic treatment, the bonds separated, indicating further development of the process was needed.

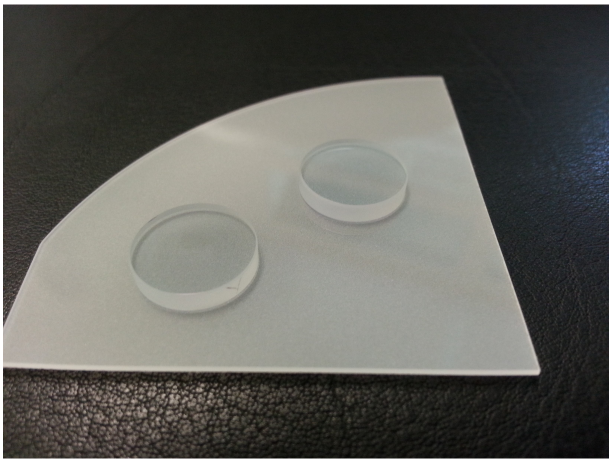

Figure 3.10: Bonded Nd:YAG and sapphire using HF as the final activation stage

To better understand the hydrophobic effects of the HF-treatment, contact angle measurements were performed on YAG and sapphire following submersion in the HF bath. However, no change in contact angle was noted, countering the hydrophobic basis of the bonding. Following expert advice on the topic, it is now understood that HF does not form stable bonds with the YAG or sapphire surfaces, instead simply etching the top layer to leave an active surface state, able to develop the dangling OH bonds required for the hydrophilic process. Furthermore, since samples bonded in this way proved to have insufficient resistance to liquid submersion without subsequent annealing, it was deemed that the transient, purely vdW-held bond could not be produced with a sufficient durability for use in mechanical processing and subsequent bonding stages. Instead, a high-strength bond suitable for use in active devices should be developed.

To increase bond strength, improvements were made to both the cleaning and annealing stages. Based on literature [61, 62], the plasma ashing stage was adjusted to a two stage oxygen and nitrogen plasma, for 30 seconds and 1 minute, respectively (further details on plasma cleaning an activation are covered in Section 3.4.3). The post bond annealing was lengthened to 50 hours, and the temperature raised to 800°C. While water was capable of diffusing through the amorphous (and more hygroscopic) borosilicate, the rigid crystalline structure of YAG and sapphire heavily inhibits this process, requiring the majority of water and hydrogen compounds to transfer outwards from the bond edge.

To encourage this process, a higher temperature is required for a longer duration to match the process seen with BK7. Above 300°C, hydrogen and hydrides increasingly desorb from the surface as temperature is increased [64], as covered in Chapter 2.2.3. This helps to convert the bond to the desired rigid, covalent bonds between surfaces, but increases the risk of further voids forming. Many high-temperature annealing techniques result in the formation of additional voids at the bond interface. It therefore is essential to thoroughly clean the bonding faces to leave surfaces as free of other hydrogen compounds as possible. Using the improved cleaning and annealing stages, higher strength bonds, resistant to liquid submersion, ultrasonic treatment and mechanical processing were completed. However, contamination issues from handling problems (bonding faces accidentally touched) persisted, resulting in voids present at the interface or forming during annealing.

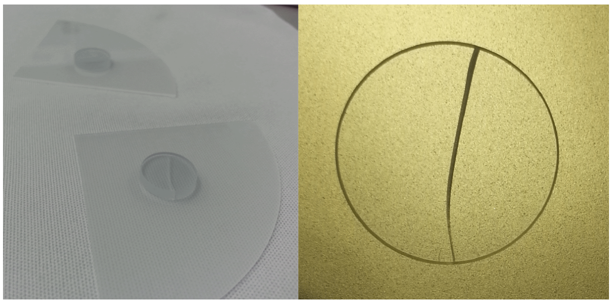

Figure 3.11: Two bonded Nd:YAG and sapphire composites, and a backlit image of the fractured Nd:YAG piece. The bond remains clear despite the damage

Demonstration of the bonding strength achieved through this method was made apparent through survival of invasive mechanical processing (dicing and polishing) of the bond. In addition, some thick YAG pieces were seen to fracture in the bulk due to thermal expansion mismatch, as shown in Figure 3.11. That the sample was seen to fracture in the bulk instead of breaking the bond suggests a strength above that of bulk YAG or, more likely, a flaw in the bond. Little information was available on the YAG used during this project which was purchased for the sole purpose of bonding trials. Higher quality, well characterised material should be used in end devices.

3.4.2 Piranha etch

Following the realisation that the HF-activation realised a similar bonding process to the hydrophilic routes, a Piranha etch stage was trialled for activation of dissimilar materials. By replicating the procedure for BK7, sapphire to sapphire bonding was achieved, with a contact wave rapidly spreading across the interface. As shown in Figure 3.12A, a large void is present at the centre of the two pieces, as well as several other voids arising from contaminants. The quality of the contact was deemed unsuitable for testing the bond process. Activation was repeated on separate samples, taking extra care to avoid any source of contamination, producing the clearer interface shown in Figure 3.12B. YAG to sapphire bonds were also achieved using the same process.

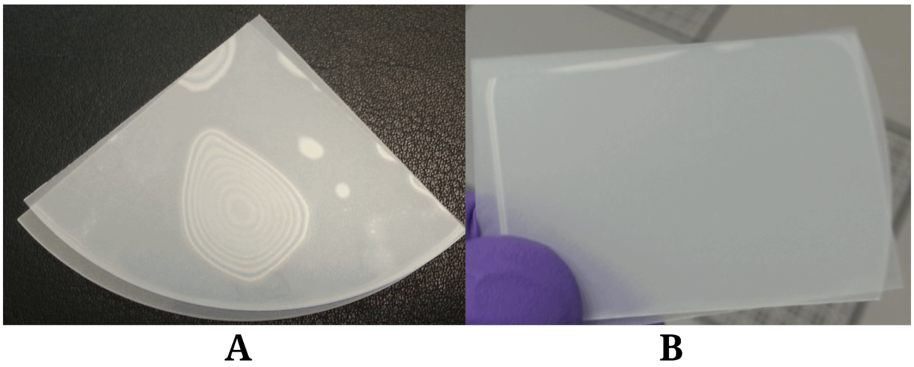

Figure 3.12: Contact between two sapphire pieces following piranha activation

Bonded samples were annealed at 800°C. Inspection following removal from the tube furnace revealed that some bonds had separated. The produced results proved highly unreliable, where samples bonded following a final-stage Piranha treatment would contact extremely well but separate during annealing. It is believed that the piranha results in an increase level of water held at the interface, even when dried with a nitrogen line. In some cases, rings of what at first appeared to be either burn marks or residue were visible in bubble shapes across the surface. To investigate the cause of this, a piranha-bonded sapphire-sapphire bond was monitored while heating on a hot plate, measuring temperature with a thermocouple placed on the top surface.

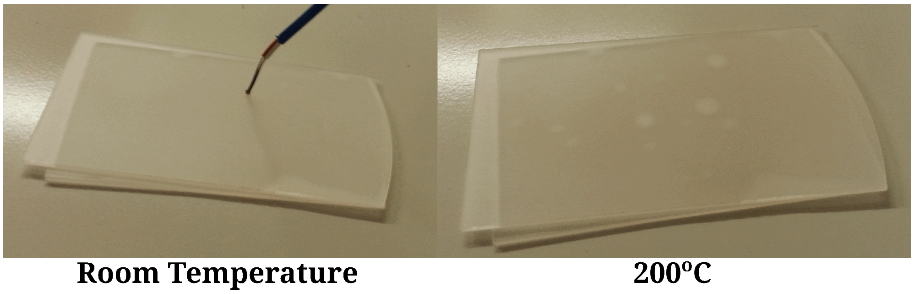

Figure 3.13: Piranha-activated sapphire-sapphire contact at room temperature and 200°C. Many voids are seen to form during heating

The comparison in Figure 3.13 shows the formation of voids during heating. Above a temperature of 190°C, voids began to appear across the central region, with the two surfaces eventually separating at 250°C. This aligns roughly with the data reported by Tong and Gosele in Figure 2.8 [47], in which heated silicon wafer bonds transferred from hydrogen to covalent bonds in this temperature range, with water produced as a result.

The piranha process induces a highly hydrophilic surface state which results in a monolayer of water absorbed to the surface that drying with a nitrogen line cannot remove. Due to the crystalline, non-hygroscopic nature of YAG and sapphire, the water is then trapped during the annealing process, unable to escape from the centre of the bond as it could with the porous BK7 glass.

Based on the observed behaviour, it is believed that the marks previously thought to be residue or burnt areas were in fact locations where the bond had begun to convert to a covalent hold during annealing. As the trapped water was heated, it was surrounded by bonded areas, expanding until the pressure was great enough to tear the two surfaces apart, damaging the faces in the process. Bonding must be completed as quickly as possible after the final stage of activation. As such, lengthy bake-out stages cannot be added to remove this layer prior to contact, making the Piranha etch activation unsuitable for these materials.

3.4.3 Plasma activation

Piranha etch and HF have proven suitable final-stages for certain activation paths, but many materials are unsuitable for submersion in strongly acidic environments. In addition, processing without the requirement for dangerous acids is an appealing target in manufacturing for both safety reasons and easier handling of samples without PPE. Plasma treatment has previously been tested as an activation process for direct bonding of crystalline Garnets [34], and was already incorporated into the cleaning stages in both routes during this project. Trials were therefore conducted using plasma ashing as a final activation stage, avoiding the necessity for an aggressive chemical activation. A Tepla plasma asher was used during plasma cleaning and activation, producing a low-pressure, microwave plasma with pure O_2 or N_2. Figure 3.14 shows both a ZnSe and a diamond sample undergoing O_2 plasma activation/cleaning.

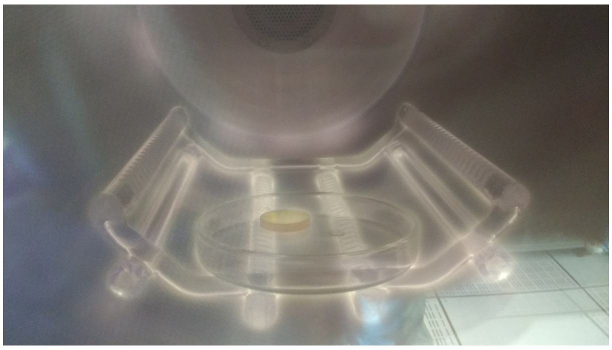

Figure 3.14: ZnSe and diamond in the plasma chamber during O_2 plasma activation

Trials were also conducted using sapphire to sapphire, and Nd:YAG to sapphire bonds. Samples were subjected to a full solvent clean before plasma activation. The plasma consisted of a two-stage oxygen then nitrogen plasma. Samples to be cleaned are placed in the activation chamber which is sealed and pumped down to vacuum before flooding with a desired gas to a low pressure. A high frequency alternating current then ionises the gas within creating particles of high energy which isotropically bombard the surfaces. The oxygen plasma removes organic molecules, while the nitrogen bombards the surface, mildly etching and freeing up highly active, dangling bonds. It was hoped that the plasma could act as a weaker hydrophilic activation, preparing the surface for a strong bond but without trapping the same level of water on the surface as Piranha activation.

When treating silicon, extended treatment with plasma can result in roughening of the surface, reducing the bond energy. To ensure no damage was caused, sapphire and YAG surfaces were inspected using a white light interferometer prior and post short plasma-treatment. No signs of roughening were noted. The length of plasma activation can be tailored to each material based on contact angle measurements and concerns of induced surface damage. For this project, a "short" and "long" plasma treatment were established.

The short plasma treatment consisted of 30s O_2 plasma followed by 1 minute N_2 plasma with an applied power of 1000W, based on literature [34, 30] and the reduction of contact angles to <5°. The long plasma treatment extended each stage to 1 minute of O_2 plasma followed by 1 minute 30s N_2 plasma with an applied power of 1000W. This longer stage was established as the cleaning time required to reduce diamond surface contact angles to <5°. Due to the increase in temperature to near 100°C, a cooling stage of 2 minutes (maintained in the low-pressure, nitrogen atmosphere) was included in the long plasma stage. Measured using Drop Shape Analysis (DSA) [69] using DI water of resistivity 18.2 MΩ, YAG and sapphire exhibited average contact angles of 70.1° and 48°, respectively. Following plasma activation, these angles dropped to <5°. Figure 3.15 shows a water droplet on the untreated YAG surface, captured during DSA measurements.

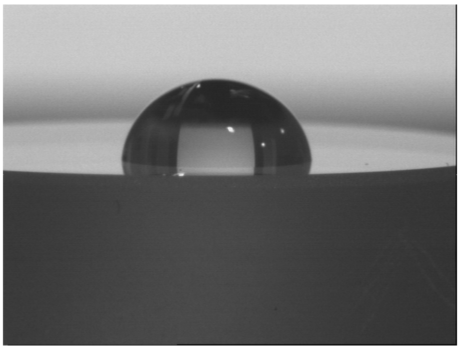

Figure 3.15: Drop Shape Analysis image of water on the YAG surface. A drop of around 12 µl is deposited on the surface and contact angles recorded

YAG and sapphire were activated using the short plasma treatment. Shortly after, samples were given a brief, 5 minute dip in DI water to saturate the open bonds with dangling hydroxyl groups. Faces were then brought into contact. No contact was formed upon immediate contact, but when the surfaces were shifted and pressure applied, the bond wave could be induced across the interface if the right location was found.

During this investigation, it was found that contact could be formed more easily by inserting a small quantity of water (~50 µl) to the interface between samples. As the water evaporated, capillary forces would pull the two faces together, forming a rigid contact. Figure 3.16A shows a plasma-bonded Nd:YAG-sapphire composite. YAG and sapphire bonded after plasma activation were then annealed at 800°C, ramping at 1°C/min up and down, as conducted during the HF activation route. However, the plasma bonds separated during a subsequent dicing process, indicating the resilience was lower than those activated via HF. Increasing the annealing stage to include a second 50 hour anneal improved the strength enough to allow mechanical dicing and polishing - rivalling the HF-activated approach.

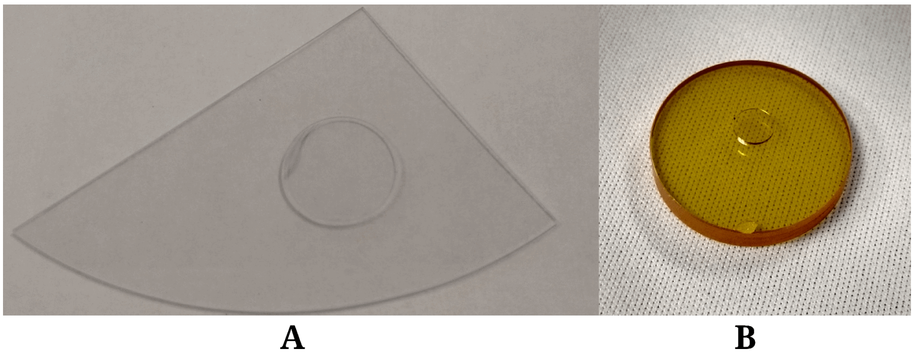

Figure 3.16: Plasma-activated direct bonding of A - Nd:YAG to sapphire and B - ZnSe to diamond

With an effective method for achieving contact, plasma activation was tested on different materials, including ZnSe and diamond. ZnSe is a soft material, and not resistant to aggressive acids like Piranha etch. As such, plasma activation is the most appropriate method. To compensate for ZnSe's low toughness compared to diamond, the ZnSe and diamond were both given the "short" plasma treatment, before removing the ZnSe and giving the diamond a further "long" treatment. Contact was successfully made by applying water as conducted in the YAG-sapphire bond. Figure 3.16B shows a ZnSe-diamond bond with a clear interface. The full development of the ZnSe-diamond bond is detailed in Chapter 6.

3.5 Hydrophobic trial

In an effort to produce the solely vdW-held bond originally sought for using HF-activation, alternative chemicals were tested for bonding capabilities. Previous work with propionic and thioglycolic acid has demonstrated an increase in contact angle for sapphire wafers after submersion [70, 71]. Carboxylic acids contain long chains of hydrocarbon, and form esters with hydroxyl groups on the surface. The interaction between acid and surface hydroxyl groups is shown in Figure 3.17. The aim of this trial was to establish if a hydrophobic surface could be generated on polished sapphire wafers, and whether the hydrocarbon chains extending from the surface could increase the relative range of vdW forces, forming a close contact with and attracting chains from the opposing surface to form a strong vdW bond.

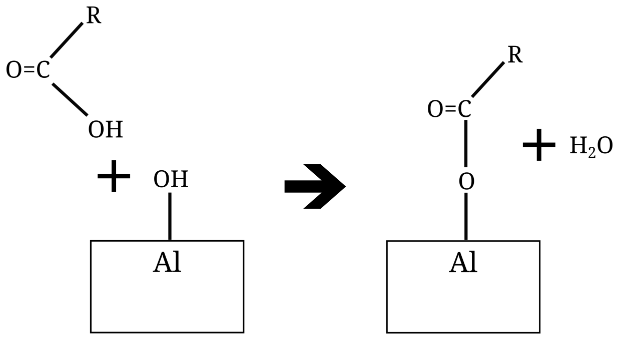

Figure 3.17: Schematic showing the development of carboxylic chains on an alumina surface, where R indicates the remainder of an extensive molecule

3.5.1 Propionic acid trial

Four pieces of sapphire wafer were cleaned using plasma ashing to reduce contact angles to <5°C. Two pieces were submerged in 10^{-1} M propionic acid for 2 hours at 50°C, and two in 1 M thioglycolic acid for the same temperature and time period. A small increase was noted in the propionic contact angle, while no change was recorded with thioglycolic acid. A further experiment was then run using propionic acid of different molar concentrations to determine the best procedure for increasing contact angle.

Concentrations of 10^{-1} M, 0.5 M and 1 M were tested. Temperatures of roughly 23°C(room temperature, RT), 50°C and 75°C were also tested. Samples were submerged in propionic acid for 30, 60, 90 and 120 minutes before recording contact angles. Before acid exposure, samples were cleaned using the full solvent and plasma cleaning process described in Section 3.7. 10^{-1} M and 1 M solutions were tested at all temperatures, while 0.5 M was tested only at 50°C.

3.5.2 Contact angles

The wafers submerged in 10^{-1} M solution saw a general increase in contact angle with time of exposure, peaking at 34°for 120 minutes at 50°C. A large dip is seen in the results at 90 minutes exposure. This may well be due to the surface of the sample not receiving proper exposure during treatment, rather than the specific time causing a drop in angle. Both RT and 75°C treatments exhibited much lower contact angles. Temperature is believed to increase the effectiveness of the surface interaction by exciting the carboxylic chains within the acid, increasing the rate of interaction with the surface. However, at 75°C significant condensation and evaporation was noted for the acid, producing a strong odour which may have indicated the acid was boiling off, reducing its effect on the contact angle. Figure 3.18A shows a contour plot for angles following the 10^{-1} M solution, while B is for the 1 M solution. It is possible that the contact angle could be increased further for the 10^{-1} M by extending the treatment time, however at two hours of exposure while monitoring and maintaining the temperature, the process had become impractically long when compared to alternate bonding activations, and raised concerns of contamination entering the bath during this long timeframe.

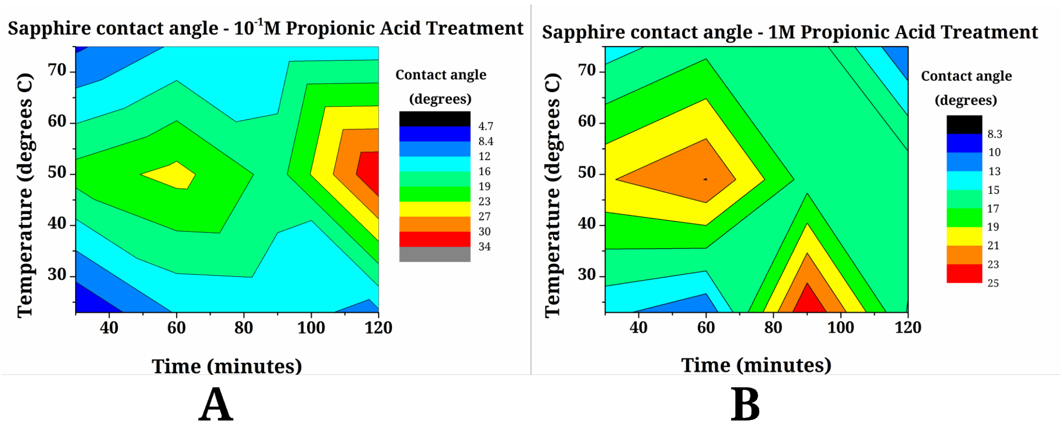

Figure 3.18: Contact angles for sapphire wafers submerged in different molar concentrations of propionic acid

The 0.5M and 1M solutions behaved far less reliably, with erratic measurements recorded across times and temperatures. The 0.5M angles recorded for 50°C were a degree lower than other concentrations so further temperatures were not tested for it. With 1 M, the greatest angle of 25° was achieved for 90 minutes at RT, closely followed by 23° for 60 minutes at 50°C. Due to the general inconsistency and lower angles of the 1 M solution, it was determined that the 10^{-1} M, 50°C, 120 minute treatment would be tested for bonding. Subjecting the treated samples to a short plasma treatment reduced the contact angles to <5° once more.

3.5.3 Propionic bonds

Bonding of sapphire to sapphire and YAG was attempted using propionic acid as the final activation stage. Sapphire to sapphire contact was successfully achieved, but resulted in numerous voids at the interface. Annealing of a propionically bonded sapphire-sapphire sample was tested at 800°C. The high temperature annealing process was successful, strengthening the bond to the point where dicing did not separate the two pieces. However, the temperatures involved would burn off any hydrocarbons present on the surface, removing the desired non-rigid bond.

Attempts to join YAG to sapphire achieved only marginal success. A bond front would only form over a partial region of the interface, as shown in Figure 3.19. Multiple bond attempts using this approach produced similar results, and as such this route for activation was not advanced further. With difficulty identifying and clear optimal concentration/temperature/time balance and only partial success seen in tests, it became clear extensive testing would be required to see if this method bore fruit as a bonding technique. At this stage in the project, success was being seen in alternate activation routes such as the plasma activation and as such, development of the hydrophobic technique was halted.

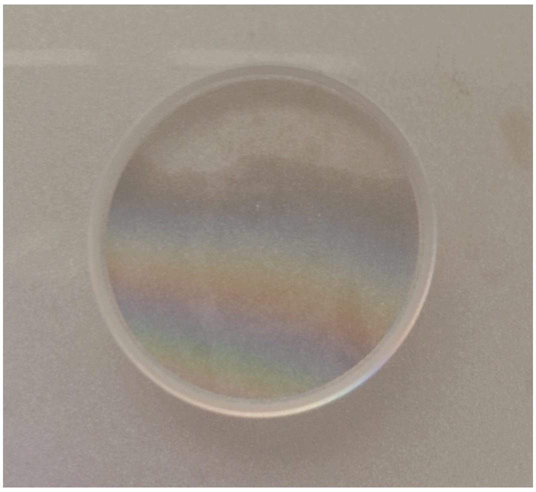

Figure 3.19: A YAG-sapphire bond conducted with propionic acid. Only the top portion of the interface appears clear

3.5.4 Heated sulphuric acid

When selecting an activation process for diamond, alternative routes besides plasma bonding were considered to produce an active surface. High-temperature sulphuric acid is commonly used as a cleaning agent for diamond, and as such was considered for use as an activation stage. It was hoped that submerging the diamond in an acid bath for an extended duration could develop a hydrophilic surface state. Diamond samples were subjected to a sulphuric acid bath within the temperature range 160-180°C for one hour. Contact angles following exposure were reduced significantly, with water wetting to the surface.

However, when the entire process was repeated on new samples, only a small reduction in angle was recorded. Repeated trials of the sulphuric acid process produced little-to-no effect. A stable temperature was difficult to maintain when raised to this degree using a hot plate, and evaporation of the sulphuric acid became prominent in this temperature range, which may have affected the concentration and ability of the acid to activate the diamond's surface. Due to the length of time required for the procedure, and success seen with the shorter plasma activation, this route was not progressed further as an activation method.

3.5.5 Analysis

Attempts to produce a hydrophobic bonding route for dissimilar materials identified a potential chemical activation method. However, when tested, increases in contact angles were small, with a maximum recorded angle of 33°, far below the 90° required for hydrophobicity. The recorded contact angles were also inconsistent, requiring further study to establish clearly ideal parameters. Contact was successfully achieved between two sapphire wafers, but the process was deemed unsuitable for dissimilar materials bonding without significant further investigation.

3.6 Conclusion

The versatility of direct bonding has allowed activation methods to be tailored to specific materials. By testing a selection of routes for feasibility, succcessful and repeatable bonding procedures have been established for bonding of borosilicate glass, sapphire, YAG, ZnSe and diamond. In each case, the bonding procedure has been improved to develop clearer and stronger bonds. BK7 was used as a trial bonding material and demonstrated the ability to direct bond on site, allowing for equipment and handling issues to be improved before work on dissimilar materials began.

Bonding of YAG and sapphire has been achieved using two routes; the HF-activation has developed a strong bond through a refined annealing process, capable of withstanding mechanical processing; the plasma-activated route removes the need for aggressive acids, producing a clearer interface at the cost of a longer annealing process to achieve similar strengths.

Plasma bonding also opens up the possibility of bonding a wider range of materials, and has been demonstrated joining zinc selenide to diamond. An attempt was made to develop a chemically-activated, hydrophobic bonding route through use of propionic acid, but proved unsuccessful. Bonding was achieved only between two sapphire faces, with many voids present. Only a small degree of contact was created between YAG and sapphire. To develop this route further, a more rigorous investigation into inducing a hydrophobic surface state is required.

3.7 Finalised bonding procedures

The final state of each developed bonding route is covered in this section. First, individual stages are detailed, before collating these into the overall bonding procedures described. Some key points regarding each stage of the process are listed below.

3.7.1 Key points on bonding

- Before cleaning of samples, all equipment to be used during the bonding procedure (tweezers, flasks etc.) should be cleaned using the same solvent cleaning stages as the samples will receive. A 5 minute ultrasonic bath at each stage is recommended.
- During solvent and acid cleaning stages, liquid-to-liquid transfer should be conducted. Samples should not be dried between stages to avoid any contaminant on the liquid surface from fixing itself to the bonding face.
- Visual inspection under white light should be conducted by eye on samples following solvent cleaning to ensure surfaces have no large contaminants.
- Bonding should be conducted in as short a time as possible following the final activation stage. The more time between activation and bond, the more likely it is that contaminants will attach to the highly active surfaces.
- Direct handling of bonding sample should be avoided at all cost and all handling minimised. If possible, use cleaned tweezers or vacuum chucks to hold samples.
- To produce piranha etch, add hydrogen peroxide to sulphuric acid, and never vice versa. Do not enclose the liquid.
- Piranha Etch rapidly rises to a temperature of around 80°C when concocted. Ideally heat upon a hotplate to maintain a temperature above 30°C for the full cleaning process.
- If pressure is to be applied to bonded samples, ensure a precision flat surface is used as a base or flexible samples will warp away from the bond rather than increasing contact.
- If possible, annealing should be conducted in a pure, clean environment.
- For materials of different CTE, low ramp rates (1°C/min or lower are encouraged).
- DI water used during processes listed here was of resistivity 18.2 MΩ.

3.7.2 Bonding procedures

Detailed below are the different cleaning stages used during bonding in this project.

3.7.2.1 Individual stages

<u>Solvent clean</u>
Nature: Hydrophilic

1. 5 minute ultrasonic DI water bath
2. 10 minute ultrasonic acetone bath
3. 10 minute ultrasonic isopropanol bath
4. 10 minute ultrasonic DI water bath
5. Dry with pure nitrogen

Short plasma treatment
Nature: Hydrophilic

1. Chamber pumped down to <0.2 mbar
2. Oxygen plasma activation at 1000W for 30 seconds with pressure between 0.2 and 2mbar
3. Nitrogen plasma activation at 1000W for 1 minute with pressure between 0.2 and 2mbar

Long plasma treatment
Nature: Hydrophilic

1. Chamber pumped down to <0.2 mbar
2. Oxygen plasma activation at 1000W for 1 minute 30 seconds with pressure between 0.2 and 2mbar
3. Nitrogen plasma activation at 1000W for 2 minutes with pressure between 0.2 and 2mbar
4. Cooling for 2 minutes

Piranha etch
Nature: Hydrophilic

1. Piranha etch (H_2SO_4:H_2O_2, 3:1) bath for 20 minutes
2. DI water rinse (<5 minutes)
3. Dry with pure nitrogen

Hydrofluoric acid
Nature: Hydrophobic

1. 1% Hydrofluoric acid bath for 10 minutes
2. Thorough DI water rinse (5 minutes)
3. Nitrogen plasma activation at 1000W for 2 minutes with pressure between 0.2 and 2mbar
4. Cooling for 2 minutes

Propionic acid
Nature: Hydrophobic

1. 10^{-1}M Propionic acid bath for 10 minutes @50°C
2. DI water rinse (<5 minutes)

Heated sulphuric acid
Nature: Hydrophilic

1. Sulphuric acid at 180°C for 1 hour
2. Cooling for 10-20 minutes in acid
3. DI water rinse (<5 minutes)

Dry bond
Bonding surfaces placed in contact edge-first and adjusted until spontaneous bonding occurs. Pressure is applied to assist spread of contact wave if necessary.

Wet bond
Bonding surfaces are placed in contact with a small quantity of DI water (~50 µl) at the interface. Top sample is adjusted until the majority of water is evaporated and faces grip.

3.7.2.2 Full processes

Piranha etch bonding
Materials Bonded: BK7-BK7

1. Solvent Clean
2. Short Plasma Treatment
3. Piranha Etch

4. Dry Bond
5. Anneal at 350°C for 8 hours

Hydrofluoric acid bonding

Materials Bonded: YAG-sapphire, Nd:YAG-sapphire, sapphire-sapphire

1. Solvent Clean
2. Short Plasma Treatment
3. Hydrofluoric Acid
4. Dry Bond
5. Anneal at 800°C for 50 hours

Plasma bonding

Materials Bonded: YAG-sapphire, Nd:YAG-sapphire, sapphire-sapphire, ZnSe-diamond, ZnSe-sapphire, diamond-sapphire

1. Solvent Clean
2. Short Plasma Treatment
3. Optional Long Plasma Treatment for tougher materials (e.g. diamond)
4. Wet Bond
5. For YAG, Nd:YAG and sapphire-sapphie, anneal at 800°C for over 100 hours

Chapter 4

Direct bonding for planar fibre preforms

4.1 Introduction

Direct bonding is established as universal technique, widely applicable with regards to materials. However, much of its use has been relegated to silicon and silica wafer bonding, with a focus in modern research on joining bulk dissimilar materials (usually crystalline) for heatspreading properties. However, direct bonding also holds potential as a unique manufacturing path in alternate areas.

Planar fibres represent an opportunity to combine the benefits of compact optical fibres with the large mode area of a planar waveguide, a structure suited to diode laser pumps. Additionally, a planar design allows for, depending on the dopant, the potential to easily write optical functionality directly into the fibre structure, e.g. gratings or channel waveguides. This project investigated a new approach to the fabrication of such a planar fibre, stemming from the manufacture of planar preforms, with the intent to develop small-scale, active devices as amplifiers pumped by diode bars.

BK7 is a "soft" borosilicate crown glass with common use in optical devices, and was chosen as the primary material for this project. A silicate glass was initially chosen over phosphate due to silica-based glass showing wide success in optical fibres, and to avoid complications posed by the negative refractive index coefficient and its dependence on temperature, typical of the latter [72]. BK7 was chosen due to a combination of desired traits, low-cost and availability. Earlier bonding trials discussed in Section 3.3 established a repeatable bonding process for the material. As a soft-glass, BK7 can be polished to the high standards required for direct bonding. Additionally, it provides a generous range between transitions, softens at a low temperature and is extremely hard to crystallise. As a widely used glass, the characteristics are detailed well by the supplier

(Schott AG) and readily available online. In addition, a number of neodymium-doped BK7 slides were previously produced in-house at the University of Southampton, and were available for use immediately. Combining doped and undoped variants of the same glass was intended to alleviate thermal expansion coefficient mismatch between the core and cladding during high temperature treatments.

This chapter investigates the production of a planar fibre preform, focusing initially on the full process development, from material sourcing to developing the preform production and fibre caning process. Before integrating bonding to the procedure, fused preforms were used to trial the caning procedure. As the ideal preform preparation method had not been identified, initial caning trials were limited to two-layer fused pieces without a doped core. This decision was made to allow testing of the draw process without use of the limited doped samples. Fusing of both rough and polished surfaces was compared to judge which method provided the cleanest interface. Canes were conducted using the equipment as detailed in Chapter 2.1. Once an optimal preparation method was identified, fusing of a preform including a Nd:BK7 core was investigated, along with direct bonding of the preform. Finally, a custom glass melt is sourced in order to test fibre caning of a three-layer planar preform as a proof-of-concept trial.

4.2 Planar waveguide fibre research history

Planar fibres, sometimes referred to as ‘flat’ fibres have only recently received attention. In 2014, Kalli *et al.* investigated the production of laser-inscribed flat fibres for the use of biosensing [73]. Combining fibre advantages such as immunity to electromagnetic interference and high temperature environments with the use of a planar chip to overcome the issues usually found coupling standard fibres to planar devices. The preforms were manufactured using a standard modified chemical vapour deposition (MCVD) before preform collapsing. This approach is used widely throughout conventional fibre development [74, 75, 76]. The MVCD production method depends on a large array of specialised equipment, requiring a significant time and cost investment when compared to the fusing method detailed in this project.

Figure 4.1a shows a cross section of the fibre. The layers represent each deposition stage. The planar structure is generally held, though both the cladding and core display a dumbbell profile, enlarging at either end. The aspect ratio of the core is kept impressively high with a a thickness of just 7.5 µm and length of 947 µm pictured. One downside of the MCVD process appears to be a residual air gap between the layers shown in Figure 4.1b. The interface appears to be visible across the core though it is not clear if this continues or affects losses (recorded as 0.12 dB/cm). A primary advantage to the flat fibre development appears to be its horizontal width, allowing the deposition and writing of intricate systems to the fibre surface.

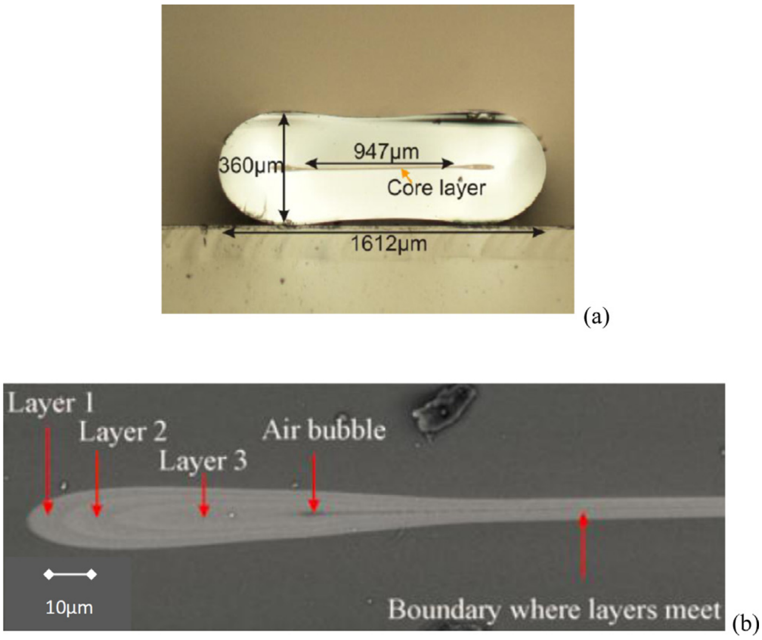

Figure 4.1: ‘Flat fibre’ developed at the University of Southampton by Kalli *et al.* [73]

An alternate planar fibre design has been considered by Marciante, *et al.* [77]. A planar fibre designed with large mode area in mind. The semi-guiding high-aspect-ratio core (SHARC) is detailed schematically, as shown in Figure 4.2. The outer cladding refractive index, n_{scl}, is kept at a small increment above the core, n_{co}, meaning that guiding is inhibited in this axis. Higher order modes which would impinge on theses edges are therefore impeded, favouring the fundamental mode.

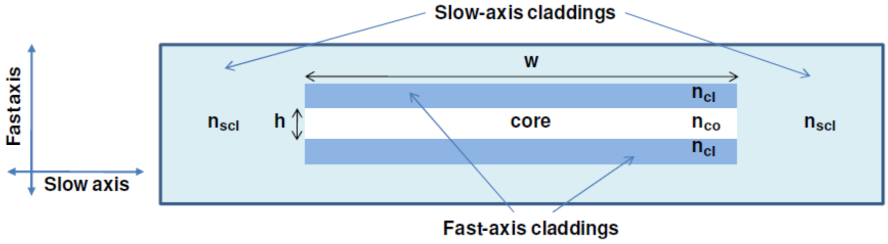

Figure 4.2: SHARC fibre cross section schematic designed to guide light only in one, fast dimension by Marciante *et al.* [77]

The principles of the fibre described by Maricante *et al.* follows a similar path to that covered in this thesis, offering an additional method to minimise higher order modes from guiding in the slow axis through inclusion of the close-index outer cladding. The fast axis cladding is kept thin to maximise flexibility of the fibre, a technique which could be applied during this project, though the aim to develop a cladding-pumped active core may restrict this. The primary benefits of the SHARC design focus on the combination of a large mode area (LMA) geometry and the flexibility to allow for compact coiling and packaging. Because the paper focuses on the theoretical modelling of such a fibre, little attention is given to a practical manufacture process. Developing a fibre structure such that the ends of slow-axis core are open to a separate cladding index would, if possible, require modification of the standard fibre production techniques. The planar preform fusion method detailed in this report could provide a simple, suitable method to achieve this either by the inclusion of further fusing stages of the slow axis cladding or choice of an appropriate polymer cladding.

4.3 Material analysis

Initial trials were conducted with fused preforms due to the simpler and shorter means of production. Before fusing glass could be conducted, the glass transitions for BK7 needed to be well understood in order to avoid crystallisation. A DTA run was attempted on a sample of BK7 Glass. The result, shown in Figure 4.3, proved inconclusive. BK7's transitions are extremely subtle, and the glass is hard to crystallise. As such, the Tg and Tx transitions aren't visible. The lack of a crystallisation peak can be attributed to the slow nucleation rate within borosilicates. The glass would have to be held at the point of crystallisation for an extended period of time before any effect was noticed or, more commonly, doped with an additional material [78, 79]. This reinforces the choice to use BK7 as a proof-of-concept glass, allowing the freedom to adjust parameters of each draw without fear of damaging the glass. Supplier values for the transistion temperature Tg (557°C), and softening temperature $T^{7.6}$ (719°C) were used.

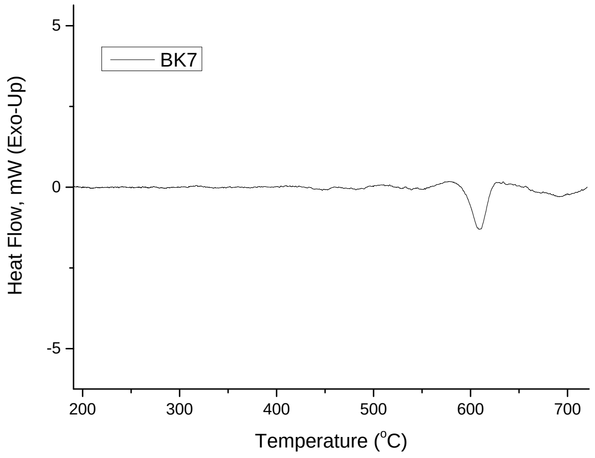

Figure 4.3: DTA reading for BK7 glass

4.4 Preform production

Preforms were formed either through fusing or direct bonding. The BK7 pieces used were polished to a local surface roughness of <0.5 nm. Individual BK7 segments to be fused were usually of dimensions 50x50x5 mm, while bonded samples were diced to 16x5x50 mm pieces prior to bonding. The specific dimensions and details of each draw are detailed through the course of this chapter. Samples to be fused were given a full solvent clean and rested upon one another before slowly raising both to the softening temperature within an environmental tube furnace. Temperature was raised rapidly until within 50°C of the target, at which point it was slowed to 1°C/min to avoid overshooting. An inert argon atmosphere was maintained during annealing. Once this temperature was reached, the samples were cooled slowly (1°C/min) to room temperature. In order to minimise deformation of the preform, no dwell time was included at softening temperature. Bonding was conducted using the hydrophilic Piranha Etch activation process detailed in Chapter 3.7. Fusing is a simple process with much less stringent demands on surface quality of the glass involved. However, fusing of glasses produces unreliable results at the interface, often resulting in large air-bubbles forming between samples due to contaminants or trapped air. Direct bonding provides a far more consistent result. While some voids are still present,they are few and far between, providing far more suitable interface to be drawn down during the caning process.

4.5 Fibre caning trials

A series of fibre caning attempts were conducted to establish the procedure. The preform preparation, caning procedure and subsequent inspection for each trial is detailed below. Temperatures listed are that of the "set" temperature, recorded by a thermocouple within the susceptor itself. A degree of offset is recorded between susceptor and the sample position. For each coil and susceptor combination, this value is listed. The offset was accounted for manually by raising the set temperature until the temperature at the preform position was as desired Figure 4.4 shows the design for the fibre tower used to cane glass during this project. The preform is secured and heated within the susceptor coils of furnace. The cane puller is used to achieve the target dimension by drawing the glass at a set rate by pressing it between two wheels which rotate at a desired speed.

4.5.1 First fused cane

The first fibre preform was produced by fusing two rough-surfaced (unpolished) BK7 slabs of approximate dimensions 56x8x4 mm (size varied between rough pieces and, at this process testing phase, precise measurements were not taken. flatness and RMS roughness of early test samples was also not recorded). The samples fused easily but

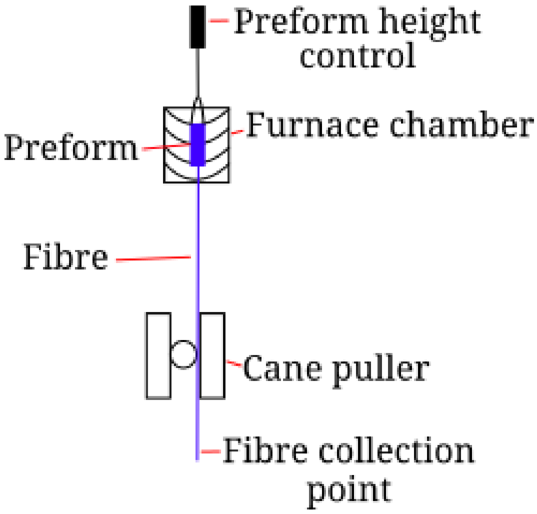

Figure 4.4: Schematic for the fibre tower used to draw preforms down to fibre dimensions

showed clear regions of trapped air. The rough surfaces provide a lower contact area, resulting in a full seal not being formed across the interface. The visual quality of the fuse appeared uniform along the sample.

4.5.1.1 Draw process

To encourage the preform to neck naturally, a mass was hung from the lower end of the preform. The mass used depends on the speed at which the necking segment is desired to draw down. For this project an 80g metal mass was found suitable for drawing the neck down. During heating on the tower, the temperature was stepped up in low increments when close to $T^{7.6}$. The preform was tested by hand at each stage, gently pulling on the hanging mass to test how loose the neck had become. The stages of the draw process are detailed below.

- Set susceptor temperature raised rapidly to 650°C
- Set temperature was heated to 840°C before any give was felt in the preform
- Large offset noticed between susceptor and preform temperature of around 100°C
- Preform drawn down by hand at 860°C. Due to the effort required the temperature was increased to 870°C and noted for further draws
- Material successfully drawn down to cane puller level but broken before loading into it
- Repeated attempts to draw glass down resulted in segments broken off each time. As such, the cane puller was not used in this draw

4.5.1.2 Analysis & inspection

Viewed by eye, the rectangular cross section was still clearly visible on the caned segments, indicating the aspect ratio had been maintained well. Twisting of the cane was visible from hand drawing; it was believed this would be fixed when successfully connected to the cane puller. Failure to use the cane puller meant that dimensions were not measured for the first pull. Retaining of the rectangular structure was considered extremely promising for this method of planar fibre production. Inspection by microscope through the top surface showed extended air gaps along sections of the cane segments. While no direct measurements or analysis were made, the draw provided a process test for the caning method, highlighting key areas for improvements. When necking occurred, the glass did not achieve a suitable viscosity to drawn down without manual assistance. To combat this, the temperature of the susceptor was increased for the following trial.

4.5.2 Second fused cane

The second cane attempt was conducted much in the same manner as the first, with suitable adjustments made to aid use of the cane puller. Another rough-to-rough preform fuse was completed by the same routine as before, resulting in a preform of approximate dimensions 70x8x4 mm. The stages of the drawing process are detailed below.

4.5.2.1 Draw process

The preform was weighted again by the 80g mass. Through volume conservation calculations, the cane puller and preform rates were run at 40 mm/min and 0.1 mm/min, respectively to produce a fibre of dimensions 0.2x0.4 mm.

- Based on the previous cane pull the set temperature was raised rapidly to 800°C
- Set temperature was ramped to 850°C and, subsequently, 870°C
- Preform necked and dropped without assistance at 870°C
- Fibre was drawn down easily to the cane puller
- Several segments successfully caned through puller

4.5.2.2 Analysis & inspection

Five long, successfully caned segments were inspected after the draw. Twisting in the preform was immediately noticeable once again. With no alignment in place, twisting of the preform occurred before the cane puller. Fortunately, the drawn segments tended to have long regions without any twists, followed by a sudden rotation. The twisting appeared to be localised to within a region of roughly 5cm. It was also noted that the preform feed rate for the tower was unstable, which could have caused fluctuations in the fibre dimensions.

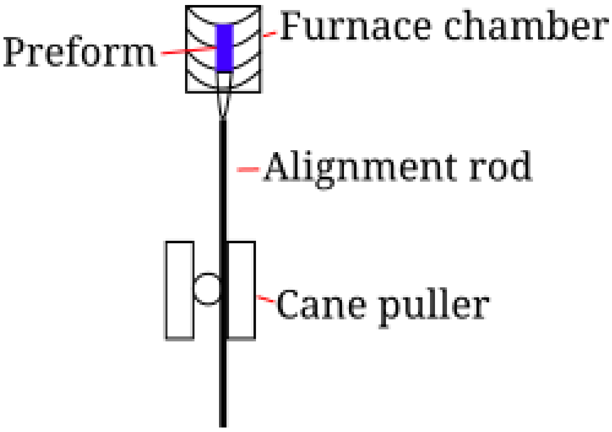

Figure 4.5: Schematic showing the alignment rod hanging from the base of the preform, secured into the cane puller before the draw commences

To prevent the twisting, a guiding mechanism was proposed. By hanging a long, flat rod of plastic or metal from the base of the preform, the wide axis of this could then be aligned to that of the preform and pre-positioned in the cane puller before commencing the draw, as shown in Figure 4.5. Because the cane puller wheels rotate at the speed required to produce the target dimensions, the wheels could then be clamped onto the flat guiding rod at the start of the necking phase, drawing the rod - and therefore the fibre cane - at the desired speed and dimensions from the start. This measure would also stop the cane from rotating freely as the neck lowered due to it being tied to the guiding rod. The preform feeder was unable to maintain a steady rate at the slow speed it was set to, so to solve this the rates of the preform feed and cane puller were adjusted, reducing the cane puller speed to allow for a faster preform feed rate.

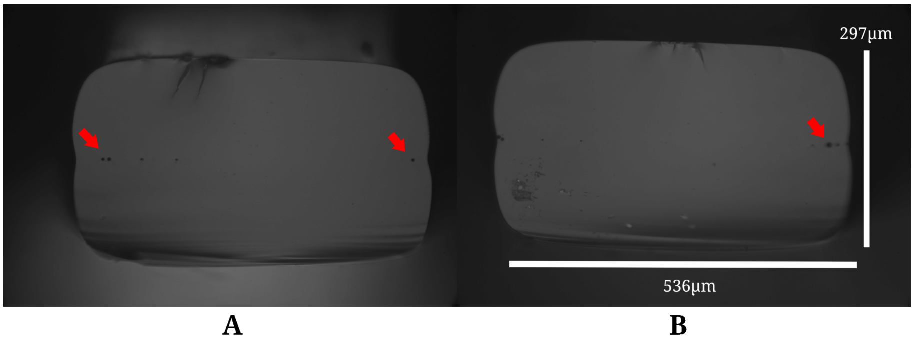

Figure 4.6: A) A cleave showing air-holes at the side, and B) A cleave with dimensions showing interface air holes. Air holes are marked by arrows

Microscope inspections of the cross-section were conducted at several places along the canes, with cleaved fibre facets giving clean areas to examine. Despite the large air regions prior to drawing, the inspected canes had relatively few bubbles or small gaps at the interface. Although when inspected along the length of the cane, most segments displayed a collection of air holes along either edge, as seen in Figure 4.6A. While the majority of the surface had drawn together for a complete seal, it was noted that in sections such as that shown in Figure 4.6B, air holes/bubbles existed throughout the central region (where light would be guided if a core had been included).

By comparing microscope images with a fibre of well-known dimensions it was possible to estimate the horizontal and vertical dimensions of one segment at 536 µm x 297 µm, respectively. This result gave an aspect ratio of 1.8x (horizontal to vertical) and a reduction in cross section of approximately 15x. Also of note was the rounding seen at both the corner and interface edges of the cane. The interface dip was likely caused by a minor misalignment of the preform which induces rounding. An overhang or dip can be seen in the side of the cross sections in Figure 4.6. Closer attention would be paid on fusing alignment in future draws as this could affect the one dimensional guidance desired for a planar waveguide.

Overall, the result showed great potential for the drawing process, indicating that a planar structure could be held well when reduced by a significant factor. The dimensions recorded did not perfectly match those calculated for the chosen preform and cane puller rates. Due to the slow speed of cane pulling, the time required to achieve the desired dimensions can be very slow, producing a large quantity of fibre at the wrong size. It is believed that, given a longer drawing time, the desired dimensions would be met more accurately.

The air bubbles clearly visible in the cane point to the need for improvements to the interface quality. In an attempt to reduce the air bubbles seen, a draw was conducted using a polished-polished fuse to compare quality post-caning.

4.5.3 Third fused cane

Following the second cane, two 50x50 mm by 5 mm thick, polished (<1 nm RMS roughness) BK7 squares were fused in a 1200°C tube furnace at 720°C. As before, the samples were raised just up to the softening temperature before decreasing slowly. Prior to fusing, the samples were given a brief acetone and IPA clean and gently contacted. Care was taken to align the squares as best as possible when entering to the oven. A lack of support during the initial fuse lead to the structure bowing slightly under its own weight. To correct this, the two-layer fuse was heated up to softening temperature once more on a flat surface. This corrected a great deal of the deformation, though minor curvature was still visible.

After fusing three large air bubbles were visible in the interface. Fortunately, a bubble-free region of suitable preform size remained. The fused BK7 was diced into three

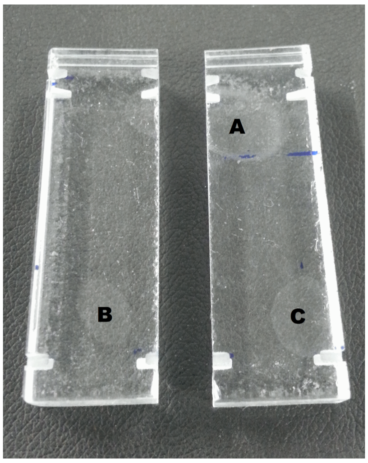

Figure 4.7: Diced BK7 preforms showing air bubbles at sites A, B and C. Bubble A is split across the cut

16 mm wide preform segments, two of which are shown in Figure 4.7. The first segment, completely free of bubbles, was chosen for the fibre draw. The remaining two piece were planned to be drawn at a later date. The position of the bubbles towards the ends of each preform, as visible in the points of interest A, B & C, meant that it was likely they would be lost during the necking or end segments, leaving a clear caning region in the centre. Extra interest was paid to whether the separated region would pull together during the drawing process.

4.5.3.1 Draw process

The resulting preform had dimensions of 16x10x50 mm. Due to the larger size of preform, a larger susceptor and coil were installed into the fibre tower to accommodate the 16 mm dimension. It was expected, that with a larger susceptor, a larger temperature disparity would be noted between the preform and recorded susceptor temperatures, requiring a higher set temperature before necking occurred. The preform was weighted again by the 80g mass to encourage necking. As before, a reduction of 20x was attempted, to see how well the draw process matched the target dimensions Notches were diced into the corners at either end of the preform to allow easier holding of the preform and tying of the mass below. The stages of the draw process are detailed below.

- The set temperature was raised rapidly to 720°C
- 20°C increments were made until necking was observed
- At 870°C minor necking was observed at a much higher point in the preform than expected

- In order to maximise use of the remaining preform material (approximately 50% lay below the neck point), the temperature was raised to 890°C and then 925°C to ensure the sample neck would lower quickly
- The cane puller was ruled out in this instance due to the lack of available material to pull; instead, as the mass lowered, segments were drawn loosely by hand and cut off at an appropriate length

4.5.3.2 Analysis & inspection

The draw process identified key factors to be reconciled in further pulls. The bigger preform housing lead to a change in the temperature focus point (and so, the necking position). Additionally, a new disparity between susceptor and preform temperature was identified to be around 200°C. These were easily corrected in future draws.

Cleaving and inspection were carried out as before, with photographs captured with a 40x objective lens. As can be seen in Figure 4.8, the rectangular shape of the preform was preserved better than the previous attempt, showing only minor curvature at the edges. The right edge, as viewed in the Figures, is seen to hold a smooth, flat shape, while the other displays a curved notch in the side. This difference is attributed to the dicing of the 50 mm BK7 squares into preforms. Diced faces create a flat, uniform surface, correcting any misalignment during bonding or fusing. These flat faces then draw down with a smooth edge, where faces with any separation in alignment (or a chamfer) maintains this feature when drawn down. If desired, the cane could be made uniform by running the dicing blade along the remaining edge to produce a similar, smooth effect.

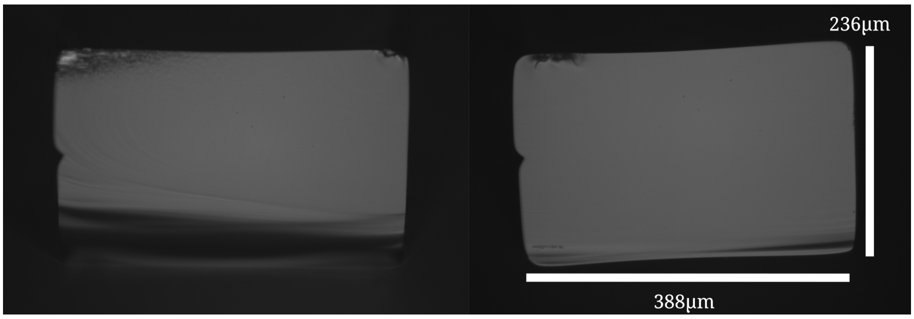

Figure 4.8: Two cleaves of the third fused cane. No air holes are visible in the cleaved fibre

A series of cleaves were conducted along the length of multiple fibre segments to ensure the fuse quality remained throughout. No air gaps were visible along the length, implying a good quality fuse. It was therefore decided that polished-polished fusing was noted as the superior method to be used in doped-undoped pulls. However, only a limited section of the preform was able to be drawn, and with large air bubbles present in other areas, it is unclear if bubbles would have been present.

The dimensions of the cane shown in Figure 4.8 were calculated as around 388 µm x 236 µm. These correspond to a reduction of 40x and an aspect ratio of 1.64, preserving the 1.6 aspect ratio of the original 16x10 mm. A greater reduction could help elimination of higher order modes in the propagating laser light due to a reduced core thickness. Coating of the preform can also assist this by increasing flexibility of the fibre. Coiling of the fibre can then be used to encourage bend losses for higher order modes. The 40x reduction when compared to the previous pull stems from the thinning of the sample during the initial drop stage. This level of reduction could be intentionally achieved by increasing the rate of the cane puller relative to the preform feed.

4.5.4 Doped to undoped BK7 fusing

Following the success seen with two undoped layers, the next step to be attempted was a doped-core, three-layer, polished fuse. In order to minimise any thermal expansion issues, 1.5% neodymium doped BK7 was used for the core region between undoped BK7. By using a doped version of the same material, CTEs were assumed to be close enough to allow comfortable fusing of the layers. The core piece of doped BK7 proved difficult to polish, resulting in one side having a finer polish than the other thanks to it being commercially polished in the past. Dimensions of the doped layer were 50x50x3 mm thick. Prior to fusing, two smaller test pieces of doped and undoped BK-7 were fused together in pairs. No problems were identified between the two samples, so it was believed that a three-layer fuse of larger samples could be completed.

Unfortunately, the first three layer stack was heated to a temperature too high and melted, rendering it unable to be used further. Tests revealed that the doped piece appeared to suitably fuse at 700°C, so to avoid any risks of deformation, further runs would be raised to this slightly lower temperature than used for just undoped glass. A second doped piece was polished to the same degree and ramped at 3°C/min to 700°C for fusing. The stack was inspected following the attempted fuse and it was found that the central, doped piece had fractured, as shown in Figure 4.9A. It was first believed that the ramping rate had been set too high, leading to fractures during expansion. To counter this, the rate was reduced to 1°C/ min for a second trial. This time, a doped test piece was placed between two ⌀36 mm BK7 samples. Once again, cracking and warping was visible only in the central, doped region, as shown in Figure 4.9B.

The appearance of thermal stress fractures during slow heating indicated either inherent stress in the doped glass, or a notable difference in CTEs between the two materials. The history and material characteristics of the in-house produced Nd:BK7 were unknown. It is also possible that the doping process for the glass introduced flaws through contamination or stress, rendering it more prone to fracture. During inspection of the doped BK7 is was noted that trapped bubbles were visible throughout the sample, providing further potential seeds for flaws to develop during heating. If testing was to be

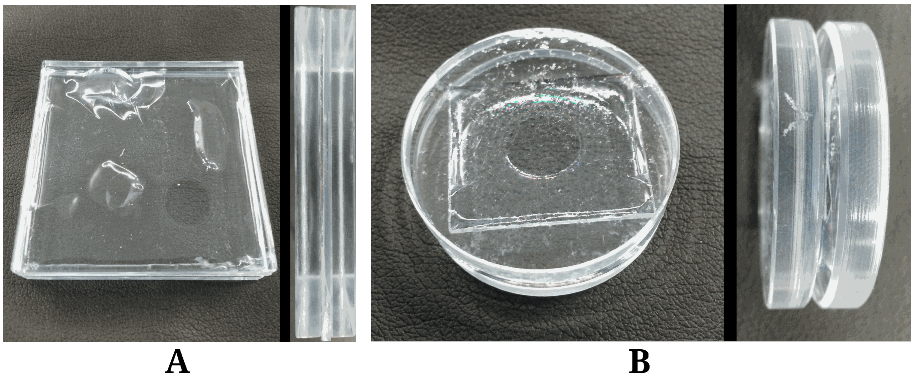

Figure 4.9: Vertical (left) and horizontal (right) view of three test fuse of A, 50x50 mm square BK7 at 3°C/min ramping, and B, 36 mm BK7 at 1°C/min ramping. Warping and cracks are visible in the central, doped layers

progressed in fusing of doped to undoped samples, joining of thinner cladding layers to match the thickness of the core is suggested as a potential method to encourage survival despite differing CTEs. However, sample numbers were limited and so rather than risk destroying more, other routes were followed.

Direct bonding requires a much lower temperature for annealing than the softening temperature for glass fusing, therefore caning of a direct bonded preform was proposed as the next trial. In addition, sources for new doped and undoped glasses of close CTE and index were investigated.

4.5.5 Direct bonded fibre cane

To develop a preform for the direct bonded draw, 50x50x5 mm BK7 blocks were acquired and trialled for bonding as detailed in Chapter 3.3.5. Following intial failed trials, a 50x50 mm window was diced to remove two 16x50x5 mm slabs, as shown in Figure 4.10. These were then bonded onto a larger 50x50 mm square, shown previously in Figure 3.8. The resulting piece was then diced to produce two 16x50x10 mm preforms. As can be seen in Figure 4.10, one edge of the glass suffered slight chip damage during the dicing process.

Damage from dicing occurs as the blade exits the glass. As the blade leaves, the final area to be separated suffers localised stress without the support of the bulk material, resulting in common chipping at the edge of the side faced downwards. It is therefore important to ensure that, where possible, the bonding surface is placed facing upwards during dicing. This will minimise cracks and chipping from damaging the stringent roughness and flatness required for bonding. The surface quality was inspected prior to, and post, dicing, with no loss in surface quality noted. The bond was annealed for 20 hours at 350°C to ensure a fully developed bond. Some minor voids were visible at the interface, but of a scale far smaller than encountered during fusing trials. As before, notches were cut into the corners and the 80g mass was applied. Cane and preform feed rates were set to attempt a 20x reduction. The larger size susceptor and coil were used once again.

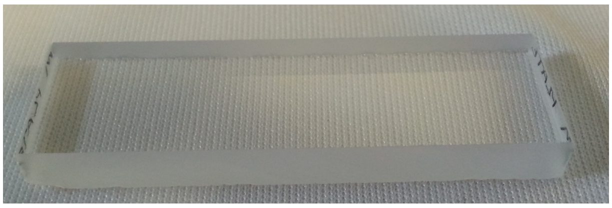

Figure 4.10: A direct bonded, 16x50x10 mm BK7 preform

To encourage the preform to neck rapidly and allow quick drawing down into the cane puller, the temperature was instead intentionally overshot to 1000°C. As soon as necking was visible at this temperature, the set temperature was reduced to 890°C to obtain a suitable speed for the draw. Once again, twisting presented a difficult issue to prevent, with the necking sample rotating as it was lowered to the cane puller. An attempt was made to rectify this by intentionally cutting the material above the twisted region and pulling it down, but some twisting was still noted. Besides this recurring issue, the draw was completed successfully, producing a large number of long length planar fibre segments.

4.5.5.1 Analysis & inspection

Cleaved faces of the bonded fibre are shown in Figure 4.11. Cane segments were cleaved using a simple ‘post-it note’ cleaving technique. Short cane segments were taped on both edges of a small flexible piece of paper (post-it note). A diamond or sapphire scribe was then brought down as gently as possible to contact with the top face of the cane before lifting it off again. The paper was then flexed to encourage the cane to snap. The minor damage caused by the scribe contact acts as a seed point for the fracture. Damage from the contact is visible at the top of most cleave images.

The vast majority of cleaved segments displayed clear interfaces, with no visible separations, as shown in A. One region cleaved displayed a small air bubble towards the outside edge of the bond. This aligned with a small void visible in the preform. Despite this minor bubble, the direct bonding process was deemed to have shown its superiority to the fusing method based on a reliably improved interface. For a manufacturing process, throughput is a crucial factor in determining which methodology to apply. With bonding providing a larger region from which to produce planar fibre segments, it was believed to be the optimum method.

Dimensions of the fibre cane cross-section towards the end of the draw were recorded as 500x900 µm, around a 17.5x reduction. These dimensions were larger than expected, likely due to the large amount of time required to obtain target dimensions. During the

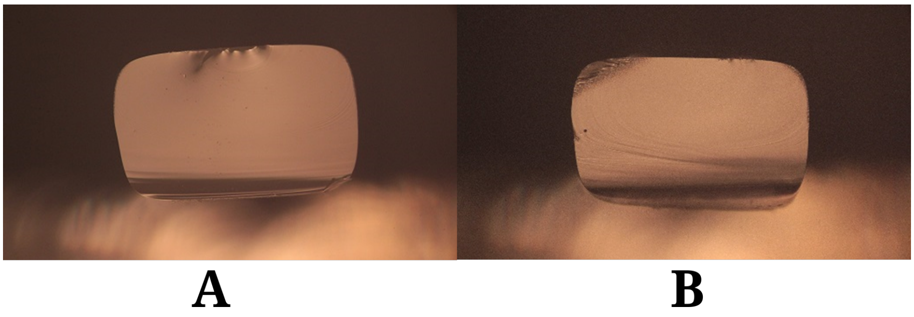

Figure 4.11: Cleaved faces of the bonded fibre cane at 10x magnification. A) A face showing a perfectly clear interface, and B) A small air gap is visible on the left-hand side

initial pull-down to the cane puller, the dimensions are reduced far below the target. Once entered to the puller, the caning process is slow, producing mm per minute. As such, it takes a long time before the desired dimensions are reached. For future draws, a metal alignment rod would be used, feeding it into the cane puller before the draw begins. This should produce two benefits: halting the twisting seen by forcing alignment and more rapid production of the desired dimensions. By drawing at the correct rate as soon as possible, the desired dimensions should be produced earlier in the draw.

The alignment rod was tested on draws unrelated to this project and was found to work effectively in pulling the necking material into the cane puller. However, the portion of the preform below the neck must still be cut to fit the fibre into the puller itself. At this stage it is important to securely hold the cane such that twisting cannot occur.

4.5.6 Ion exchanged draw

While identifying a source for doped glass to be used for the project, trials were run to test reduction of a guiding layer within glass. For this purpose a potassium ion-exchange was conducted on one 50x50x5 mm polished BK7 piece to raise the surface layer's index. Potassium was chosen for the exchange due to its availability as well as experience within the research group in exchanging it with silicate glasses.

4.5.6.1 Ion exchange process

A KNO_3 salt bath was heated to 395°C. The salt was allowed to reach temperature stability before submerging the BK7 slab for 20 hours. Upon removal from the bath, the BK7 sample was cleaned in an ultrasonic DI water bath, before undergoing further annealing (2 hours at 405°C) to ensure maximum in-diffusion had occurred. The slab was then diced into three segments. The surfaces of each were inspected, and the two best (lowest RMS roughness, fewest bumps) were chosen for fusing. Direct bonding was considered, but the ion exchange process deposited material on the surface, creating tens of nanometer jumps in height, as shown in the 3D surface map in Figure 4.12. These were not removed by a solvent cleaning stage. Following the exchange, the index shift over depth was recorded with a Metricon prism coupler, and found to have a recorded depth of around 10-15 µm and an index shift of 5.02x10^{-3}. If two pieces with an exchanged region of 10-15 µm were fused together, a core region of 20-30 µm could be created.

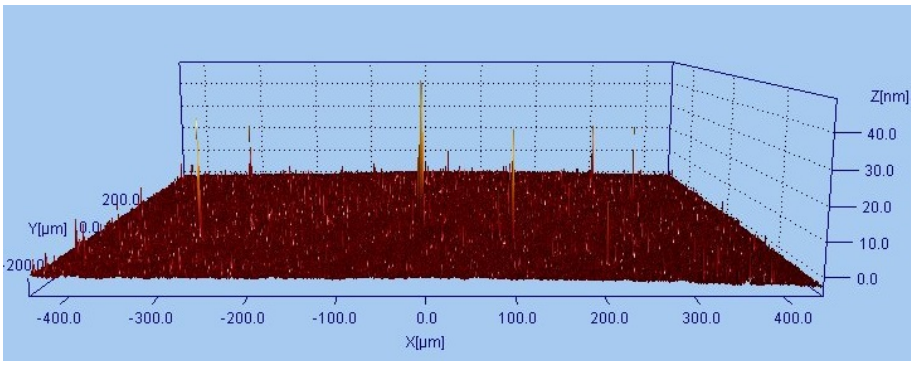

Figure 4.12: 3D surface map of the ion exchanged BK7 sample. Surface spikes of 40 nm in height are visible. RMS roughness was recorded as surpassing 1 nm in regions with a large number of spikes

4.5.6.2 Draw process

The preform was produced by fusing two 16x50x5 mm KNO_3-exchanged BK7 slabs together (at 720°C) to create a preform of dimensions 16x50x10 mm. Following the fuse a large air bubble appeared at one end of the preform, trailing off towards the lower edge. This end was chosen for the lower region during the fibre cane draw, expected to be wasted during the necking and size adjustment phases. Notches were cut on corners of each end of the preforms for wire wrapping. The preform was aligned and weighed down using the metal rod tested previously, which was fed into the cane puller.

Initially, the cane puller was run at 5 mm/min with preform feed 1 mm/min to produce a 5x reduction, however the cane puller struggled to achieve such a slow rate. Speed was then raised to 10 mm/min with a preform feed of 2 mm/min. With the alignment rod fed into the cane puller, using a method to overshoot the temperature and encourage necking was not desired, as this would lead to the cane dimensions reducing drastically. It was instead aimed for the glass to be brought just up to necking point, loosening enough for the cane puller to be activated before setting the furnace temperature stable for the draw. The stages of the draw process are detailed below.

- The sample was raised to 800°C in 100°C increments at 100°C/min
- At 800°C a rest of 10 minutes was given to watch for signs of necking
- Minor deformation was seen and the temperature was then raised to 850°C to encourage the neck

- Neck was spotted at 850°C, the temperature was dropped to 830°C and the cane/preform feeds were started
- Temperature was raised to 850°C and, subsequently, 870°C to increase dimension reduction
- Necking section was pulled manually to a thinner dimension and cut before feeding into the cane puller
- Exhaustion of preform

4.5.6.3 Analysis & inspection

For this draw, the metal alignment rod was placed in the cane puller and run as soon as necking was seen, intending to obtain desired dimensions as quickly as possible without the sharp initial change seen in previous draws. In this case, the cane puller successfully began to pull the neck down, but this would cause material to travel outside of the hot zone too quickly, resulting in dimensions that were too large. The cane was drawn down manually to reduce the cross section a small degree before continuing. In future slow draws like this, a small degree of manual draw down is recommended to bring the cane close to desired dimensions before leaving to run in the cane puller.

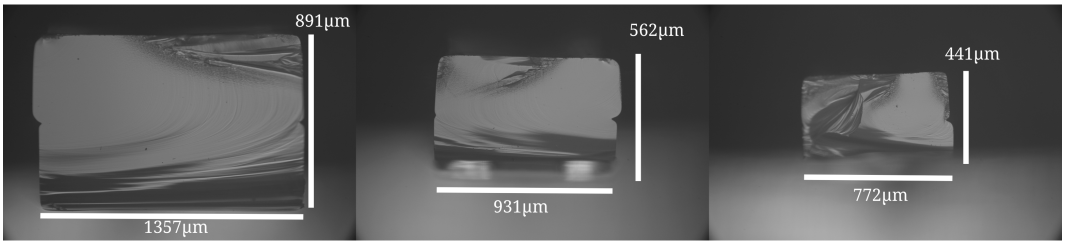

Figure 4.13: Three cleaves of different dimensions obtained during the ion exchange draw

Overall, the pull was successful despite a stable cane dimension not being obtained. Various segments were produced and, following cleaves and inspection, seen to have pure interfaces without air gaps. As the cleave inspection photographs shown in Figure 4.13 make clear, a variety of thicknesses were obtained, with reductions of 11.2x, 17.9x and 22.7x obtained. The reduction in preform dimension were found to fall within the range of 10-23x. Cleaved segments were measured to have cross section of dimensions 833x1326 µm to 435x700 µm. Larger segments were available but could not be cleaved cleanly using the same method, as significant damage would be induced in the cleave plane. For each cane dimension, the aspect ratio of the planar structure was maintained.

4.5.6.4 Waveguiding

To inspect if the ion exchanged layer had been successfully drawn down, short segments, cleaved at either end, were given a cursory polish and backlit, highlighting a clear region of different index within the centre, visible in Figure 4.14A and B. The index shifted layer is highlighted in B, with dimensions measured from the image as 13 µm. To demonstrate the guiding capability of the caned glass, a HeNe laser was coupled into a short segment using a 25 mm lens. Figure 4.14C shows the re-imaged output (rotated 90°), with a clear central, guided spot. Additional noise on either side is attributed to the poor quality of polish on the fibre end facets. The size of the central beam was recorded and used to calculate the mode size diameter as around 54 µm.

The value calculated from the beam was far larger than the 13 µm obtained through visual inspection of Figure 4.14B, but it is not expected that the full mode size could be identified accurately through measurement of backlit images. In addition, the gradient index induced by the ion exchange would support a larger mode size than the width of the exchanged layer. An interesting point noted in this trial, was that the reduction for the core layer during the draw process does not match that of the preform glass. Compared with the visual measurement, the "core" region was reduced by just 2-3x. As such, it is possible to speculate that further in-diffusion occurs during the draw process itself. As the glass is heated to the softening temperature, the potassium ions may penetrate further into the sample. For distinct glass layers, this wouldn't be expected to occur, but should be kept in mind for draws conducted on glass doped via ion-exchange with active materials.

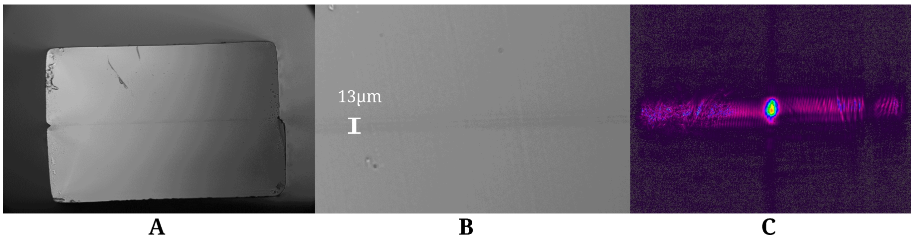

Figure 4.14: A) Backlit image of a ion exchange BK7 cane, B) Expanded image of the central core, and C) Re-imaged output of a HeNe laser coupled into the waveguiding layer, rotated 90°relative to images A and B

4.6 Custom phosphate glass

In the final stage of this part of the project, it was planned to produce an active device using the planar caning process. A number of commercially available glasses were considered, but a suitable combination of CTE and index could not be found. For this purpose, a custom, phosphate glass was commissioned from a local glass supplier, with desired characteristics of closely matched CTE and index between a neodymium-doped and undoped variant. Phosphate glasses tend to be less sturdy that silicate based glasses, but allow for higher doping concentrations of rare-earth metals. In addition, phosphate glasses tend to have lower softening temperatures than silicates, making fusing and reaching drawing temperature faster. Requirements for the glass specified a glass stability parameter (range between glass transition and crystallisation temperatures) of over 200°C, with less than 5% difference in transition temperature, CTE and thermal conductivity between doped and undoped variants. A Nd-doping concentration of 0.3wt% was requested, with an index increase ($\delta\eta$) between 0.0001 and 0.002 with respect to the undoped glass. The intention for this design was to produce a short, planar amplifier, capable of guiding in one axis, while allowing the beam to free-space propagate in the other. A device was planned such that the signal would be core guided and limited to single-mode, while a multimode pump beam was guided by the cladding layer.

4.6.1 Trial 1

The first supplied glass batch did not meet the required characteristics. Glass Refractive Index Measurements recorded the doped and undoped glasses to have an inverted index difference, with indexes of 1.52696 and 1.529785 (@ 25°C), respectively. In addition, the glass itself was found to lack the optical clarity desired for use in laser optics. Striations were clearly visible by eye in the glass itself, indicating the components had not mixed correctly. Within the doped glass, trails of concentrated neodymium were clearly visible through the tell-tale purple hue. Figure 4.15A shows a glass melt in the process of cooling, while B shows a view through the final glass composition. pockets of contaminants and air bubbles are clearly apparent, along with visible striations in the glass.

Figure 4.15: A) The custom glass melt cooling, and B) A backlit view through the final composition displaying clear lines of striations and other contaminants

The glass transition temperatures for the doped and undoped pieces were supplied as 475.9°C and 464.6°C, respectively, with predicted softening temperatures of 513.5°C and 497.2°C, respectively. Differential thermal analysis (DTA) was conducted in house to confirm these values, and recorded values for Tg as 468.53°C and 463.37°C. In order to confirm the softening temperature, test samples were heated in oven environments to note when fusing occured. The glass was found to fuse at 510°C.

4.6.2 Preform preparation

These optical issues rendered an active device based on guiding between a doped core and the undoped cladding impossible. However, it was determined that, seeing as the physical properties were within spec, the draw process would be conducted as a proof-of-concept for the manufacturing process. A three layer stack of undoped and doped materials was produced by dicing segments of dimensions 20x75 mm from the larger doped and undoped blocks. The areas with least visible striations, air bubbles and contaminants were selected. The core piece was lapped and polished in-house to a thickness of 4 mm, while the cladding pieces were polished to thicknesses of around 1 mm and 3 mm. Both cladding pieces were intended to be 2 mm, but due to limitations in the polishing slurry available this could not be achieved. For a test draw to demonstrate the process, however, the thicknesses of cladding was not crucial.

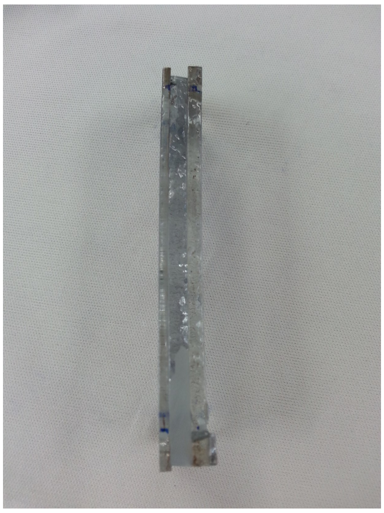

Figure 4.16: The three-layer fused phosphate glass preform

Fusing was conducted at 510°C in an argon environment tube furnace. The temperature was raised at 3°C/min to 450°C before a 1°C/min rise to fusing temp before reducing back to room temperature at 1°C/min. The three layers were all fused in one process to ensure equal treatment. The glass fused well but displayed large air bubbles between layers (as expected from fusing). Fortunately, bubbles at each layer overlapped, leaving other regions in the interface bubble-free. Notches were cut in each corner to hold the preform via wire during the draw. The preform was weighed down by the guiding rod which was fed through the cane puller. The cane puller was run at 56 mm/minute with the feed rate at 1.4 mm/min to attempt around a 20x reduction. Due to limited availability of equipment, a new furnace setup was used during the draw with an untested combination of susceptor and heating coil. Unfortunately no calibration data was available for this combination so positioning of the preform was left up to eye. It was planned to heat the preform carefully near the softening temperature, watching for necking and adjusting the preform height to maximise use of material. The draw process is detailed below.

- Temperature raised to 400°C at 100°C/min
- Temperature raised to 500°C
- Temperature raised in increments of 50°C to 600°C before a 5 minute wait to see if necking occurred
- Temperature raised to 650°C and given 5 minutes to see if necking occured
- Minor necking observed higher than desired so the preform was raised to counteract. Temperature raised to 660°C. Preform feed and cane puller started
- After disconnecting mass, the cane snapped off before being entered to the cane puller. The preform had then to be lowered and temperature raised to 730°C to encourage necking again
- Second neck occurred and was successfully drawn down into the cane puller. Some twisting occurred but was later corrected. The temperature was dropped back down to 700°C once the cane was running
- Draw completed

4.6.3 Analysis & inspection

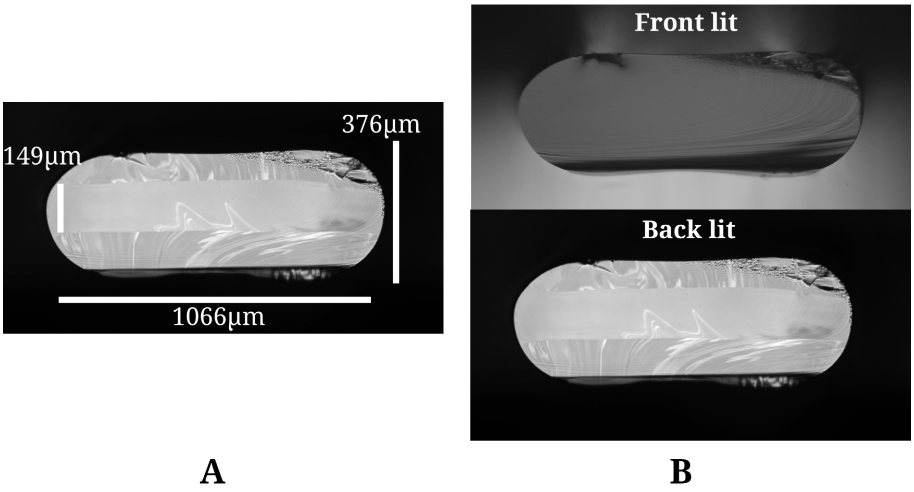

Figure 4.17: A) The cleaved phosphate glass cane with dimensions, and B) A comparison between front and backlighting of the cleaved fibre. Compositional problems in the glass are apparent in the backlit image

Figure 4.17A shows a cleaved cross section of the drawn cane. Dimensions of fibre canes were recorded between 20 and 21x reduction, indicating that the process, including the alignment rod, is sufficient to produce targeted dimensions. Notable rounding is present at the edges of the fibre. As the aspect ratio of the fibre is increased, more rounding occurs due to the difference in temperature from the edge to the centre of the sample. This can be mitigated by ensuring a sharp edge is present on the preform. As seen with the BK7 preforms, a dicing saw blade can be run along the edge of the preform following bonding or fusing to ensure a flat edge.

Figure 4.17B's comparison between front and backlit inspection makes apparent the compositional problems within the glass. Striations are evident throughout the undoped cladding, with a clear region seen in the core layer too. To ensure that these were not flaws at the interface induced by cleaving, a number of segments of fibre were cleaved on alternating top and bottom faces of the cane, but the observed markings were independent of cleave side.

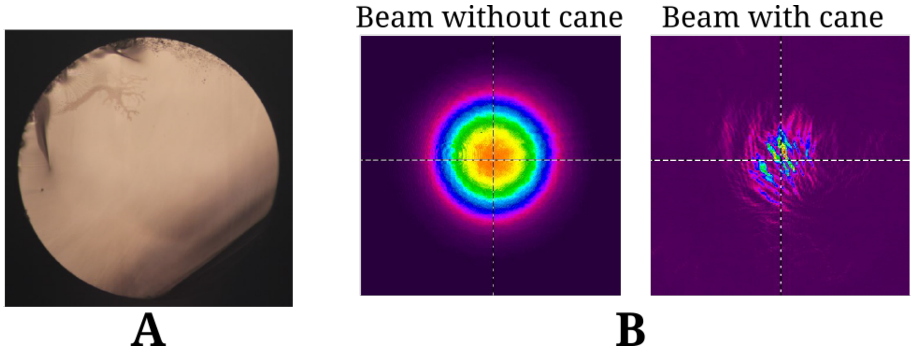

Figure 4.18: A) The cleaved rod showing compositional differences, and B) A comparison between a 1 micron beam passed through free space and through the caned rod

In addition to the planar draw, a 15 mm diameter (drawn down to 1 mm), 70 mm long rod cane was produced and used for transmission purposes to determine quality of the glass. Figure 4.18A shows the caned rod displaying compositional differences, while B shows a comparison between a 1 µm laser beam profile which has been captured after passing through free space, and after passing through a rod of the phosphate glass. The beam passing through the rod is significantly distorted, splintering into messy ripples. A second glass production aiming to improve the index and transmission problems was requisitioned in an attempt to rectify these issues.

4.6.4 Trial 2

A second iteration of the phosphate glass fabrication was commissioned, with matching specifications but targeting an improved homogeneity. When supplied, initial inspection of the bulk glass appeared visually improved from the first stage. Some striations were visible toward the very edges of the glass blocks, but these could be avoided during dicing. The glass was analysed using Glass Refractive Index Measurement (GRIM) in which small sections of glass are submerged in liquids of known indexes and changes with temperature. When viewed through a microscope, the glass slivers become transparent when their indexes are matched by the liquid used. The doped and undoped variants were found to have indices of 1.5338 and 1.5311 at 25°C, respectively. The index difference did not lie within the desired $\delta\eta$ of <0.002, but the index profile would be of the correct orientation to allow guiding.

Transmission measurements through differing lengths of glass were collected using a photospectrometer, as shown in Figure 4.19. By normalising the data, absorption lengths were calculated for the 800 nm and 880 nm features by comparing lengths which returned absorption lengths of 2.58±0.1 cm and 7.11±0.5 cm at each respective wavelength. Absorption lengths were calculated using the Beer-Lambert law [80]. For an input power $\mathrm{P_I}$, and output power $\mathrm{P_O}$, the relationship can be defined as:

$$P_O = P_I * e^{-\alpha L} \tag{4.1}$$

Where α is the absorption coefficient and L is the sample length. This can be rearranged to obtain:

$$\alpha = -ln(\frac{P_O}{P_I})/L \tag{4.2}$$

Absorption length is given by the inverse of the absorption coefficient. For a series of known lengths and transmissions, an average absorption length can be calculated. Three different lengths of glass were tested using samples polished in house and recorded with a spectrometer. One cube of 9.5 mm face width and a longer, rectangular cuboid of face widths 19.6 mm (long dimension) and 9.6 mm (short dimension) provided the test lengths. Ideally at least three different lengths at set intervals of length would be tested. However, material was limited for this project, resulting in two testing lengths of similar values (9.5 and 9.6 mm). The absorption lengths calculated should therefore only be taken as rough calculations, with greater precision required for a final product.

The long absorption lengths would present difficulty in a planar device pumping in the 880 nm regime. Typically, a device length three times that of the absorbtion length is desired to maximise absorption in a single pass. As such, a device of least 21cm would be required. An active planar device could still be imagined using a double-pass setup with an 11cm device length. In order to pass the pump beam without clipping at the edges of the cane in the wide axis, the following device was proposed based on pumping with a diode stack. By guiding in the direction of higher M^2, the axis of greater beam quality is able to propagate freely through the core medium, making use of the large mode area. For an M^2 of 14 and device length of 11cm, a beam waist of 635 µm is required to produce a Rayleigh range the length of the device for the pump wavelength (808 nm). Accommodating for 99% of power in a Gaussian beam, this requires a width

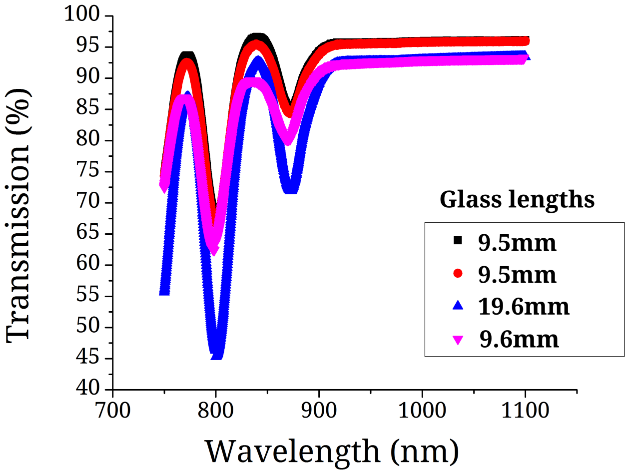

Figure 4.19: Transmission tests on a different lengths of the Nd:phosphate glass

of $\pi * \omega_0$, or 2-3 mm. A cane of target dimensions of 350x3000 µm was therefore chosen as the goal.

Assuming the aspect ratio is maintained during the draw, this allows for a preform of dimensions 2.3x20 mm. In order to maximise absorption, the cladding layers would need to be reduced as much as possible relative to the core. A cladding thickness of 450 µm with a core of 1.38 mm was proposed, and polishing work began on samples to achieve this. Similarly, for 800 nm pumping, identical dimensions could be applied, reducing the length of the device.

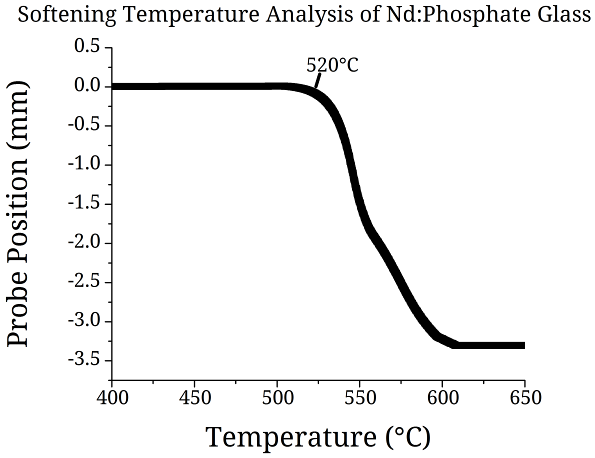

Figure 4.20: Probe pressure test to identify the softening temperature of the Nd:Phosphate glass. The probe position is recorded as temperature is increased

Before fibre drawing, the glass was given a three-point pressure test to discover the softening temperature of the glass. A small sample of glass is set on top of two contact points a few cm apart. A probe is then gently pressed down into the surface of the sample with a force of 500 mN. The sample is then heated at a rate of 10°C/min. The probe position is tracked during this time. The softening point ($T^{7.6}$) can be seen as the glass begins to give under the probe's pressure. Based on Figure 4.20, the glass can be seen to clearly soften at around 520-530°C. This temperature region was set as the target for fusing of preforms and fibre draws in order to achieve necking in the preform.

4.6.4.1 Nd:Phosphate draw

A test draw was planned using only the core, Nd-doped phosphate material, in order to investigate the glass properties at fibre dimensions. Two draws were conducted, one using a 10x10x75 mm square preform, and another with a 2.55x22.3x60 mm planar preform. A draw temperature of 700°C was found suitable based on the material's characteristics recorded previously and experience from previous attempts.

Figure 4.21: Captured images of the cleaved Nd:Phosphate draws. The full cross section of the planar structure proved too large to capture under 10x magnification. An edge and central region are shown instead

The cleave images in Figure 4.21 show that the square rod held its shape well. The chip visible in the top left corner occured during the cleaving process. The planar preform displays some bowing across the length of the sample, with thickness varying from a minimum calculated value of 347.6 µm to a maximum thickness of 421 µm at the edges, or a calculated radius of curvature of 1000m. This curvature, while slight, could act detrimentally on the guiding characteristics of the of the rod when attempting to make full use of the width. This problem could be corrected through use of a larger coil and susceptor during drawing, in order to maintain a more uniform heat profile across the width of the planar preform.

Transmission measurements were run on the drawn square rod to test if the glass was suitable for further investigation. Testing a 48 mm caned segment, an intrinsic loss of -0.11 dB/cm was recorded at 1 µm. Furthermore, some distortion of the transmitted beam profile was visible. Due to the low dopant concentration within the glass (and therefore gain), the glass was not deemed suitable for using in amplifier or oscillator devices and progression of the project with this glass was halted.

4.6.5 Analysis & conclusion

Through use of custom-made phosphate soft glass, the fibre caning process was demonstrated successfully from materials characterisation and preparation to a three-layer cane. The capability to take an unknown glass and, following short characterisation on the glass transition temperature and fusing trials, develop a planar preform and draw demonstrates the simplicity of the fabrication method developed in this chapter. The phosphate glass had ideal drawing characteristics, having a low softening temperature, closely matched between the two variants, with no signs of crystallisation indicating a wide stability range. However, the glass itself was found substantially lacking with regards to optical characteristics. This was believed to be a fault of the simplified batch fabrication process employed. A more industrialised fabrication method was promised to improve the optical properties of the glass.

The first batch phosphate resulted in an inverse index profile, which would frustrate guiding within the core. In addition, the homogeneity issues present within the glass were visible to the naked eye. Initially it was hoped that homogeneity may improve during following caning of the glass, however no improvement was noted, with cleave inspections and transmissions measurements clearly identifying inhomogeneous material throughout the undoped glass. The neodymium dopant was also seen to cluster within the glass, leading to regions of discolouration. Not only would this distort the transmitted beam, it would also likely reduce the localised concentration in the remaining glass. As such, even if a clear section could be identified, the wt.% concentration would be below expected. The second batch of the glass, though improved at the visual inspection level, still had clear grouping of neodymium towards the edges of the material. When tested optically, intrinsic losses within the material proved too severe to progress work further.

Given an improvement in material quality, this area of the project is also open to a number of alternate improvements. The 0.3wt.% concentration of neodymium used within this project should be increased to closer to 1wt.%, with the device length reducing closer to 3cm. The appeal of this design structure is in the mass production of small, short length amplifying devices. Based on one-axial guidance, the advantages of the planar structure come from a high aspect ratio, making use of a larger gain region, which allows for higher-power before detrimental thermal effects begin to occur.

With a low dopant concentration, a longer device is necessitated, making it difficult to avoid clipping of the beam at the edges of the unguided axis for both pump and probe. In addition, increasing the dopant concentration allows a more reasonable ratio between core and cladding material, reducing the requirement of such a thin cladding layer, which proved difficult to achieve with a good standard of polish without damage. For a final device, an outer coating layer would be required, both to improve guiding of the pump within the cladding, and to improve durability. Without polymer coating, the fibre remains extremely brittle, prone to fractures and contamination at the surface. Some preliminary coating trials were run on-site following the cane process, but ideally the coating stage would be conducted within the draw itself, pulling the cane through a polymer coating bucket before UV curing. It is believed that with these improvements, a bonded three-layer planar fibre could be produced, creating an appealing, mass-produced, small-scale amplifier, should appropriate glass be sourced for use.

4.7 Conclusion

In this chapter a novel approach to the production of planar fibres has been detailed. The fibre characteristics are defined simply through the production of an appropriate preform. Through simple methods of glass-saw dicing, fusing and direct bonding on the macroscopic scale, preforms can be developed without equipment-heavy requirements of methods such as MCVD or other more commonly used preform production techniques. The fibre caning process and preform production have both been improved through each trial. By inspecting the resulting cleaved facets from each draw, the key factors of influence have been identified at each stage. Ensuring sharp, well defined edges for the preform was noted to assist in maintaining the preform shape during the draw.

The twisting problem encountered during the draw, while not catastrophic for the production of short-length devices, results in the loss of a portion of the drawn material, and can cause issues with the feed through the cane puller itself. This was rectified through practical application of the alignment rod, improving the yield of the process. The effective improvement through use of direct bonding has been confirmed via the interface quality. Fusing of preform samples has the potential to produce void-free interfaces, but is highly unreliable, prone to large air-bubbles appearing. While this can allow for void-free regions in a two-piece draw, a three-layer structure requires an additional fusing stage, doubling the risk of voids appearing over the desired area. Direct bonding mitigates this issue, producing minimal voids when conducted cleanly, albeit with the requirement of more stringent polishing and cleaning.

Using a custom phosphate glass, the full process, excluding a direct bonded preform, was conducted, demonstrating the creation of an effective manufacturing of the fibre draw. Forgoing problems arising from material faults, the majority of problems encountered during the project have been rectified. The curvature of the resulting cane, witnessed most prominently in the final Nd:phosphate draw, remains a pressing concern, exacerbated by an increasing aspect ratio. However, it is believed that should a well defined preform of multiple layers be produced in combination with a larger coil and susceptor, this would alleviate the problem. Current preform designs were at the size limit of the susceptor used, resulting in the edges of the preform not being heated to the same temperature.

Should a larger susceptor be applied, an even heating should result in the well-defined planar structure being maintained, as seen on the other draws. A final bonded stage was not tested using the phosphate glass and would require additional work when compared to the fused preforms, necessitating a separate bonding stage for each face with excellent polishing. However, with a suitable material this would not present additional complications and could be imagined as the next step in rounding out testing of the process.

Material issues hampered progression to a final, active device, due to inhomogeneity and intrinsic losses ultimately limiting further work in this project. Nevertheless, this report has established the manufacturing process as effective, adaptable to different dimensions and capable of a high throughput. Pending the acquisition of operative glass and the improvements detailed previouisly, the creation of small-scale, active devices could be imagined using direct bonding in the production of planar preforms.

Chapter 5

Nd:YAG to sapphire bonding for active devices

5.1 Background

Direct bonding has been demonstrated in the joining of dissimilar materials for active devices for over 20 years [3], however there has been very little reported in the literature about how this process is actually achieved. Two companies in the US have dominated the market in producing composite structures based upon the direct bonding approach with few, if not no, other suppliers of such devices. In recent years there have been several groups reporting room temperature direct bonding of various materials [81, 27, 34] all with the aim of enhancing the optical functionality of a certain materials through the combination of key features, such as thermal or physical properties. In addition, modern bonding research has extended to joining of complicated interfaces such as AR-coated interfaces [5] or multi-layered bonds [28] to improve efficiency of cooling or pumping. However, these works are limited in dimensions and make little effort to interrogate the environmental resilience of bonded composites.

In this work, development of chemical and plasma-assisted methods is presented for activating two oxide crystals followed by their direct bonding without any active agent to join them, relying instead upon van der Waals forces initially before a thermal anneal consolidates the bond strength. In this project, YAG and 1.3at.% Nd:YAG crystals are bonded to sections of sapphire wafer, with the primary goal of creating a bonded composite resistant to a variety of environmental conditions and harsh machining processes, as this would allow post-bond tailoring of the composite to desired dimensions. The intimate contact of direct bonding lends itself to use in heat-spreading, and particular interest for the YAG-sapphire bond lies in cryogenic applications, where the thermal conductivity of sapphire ($\sim 1000\,\mathrm{Wm^{-1}K^{-1}}$ @77 K [82]) begins to rival that of room temperature diamond $>1500\,\mathrm{Wm^{-1}K^{-1}}$ @300 K) [83]. Following successful production of a sturdy bond, Nd:YAG crystals were processed to suitable dimensions, diced and coated before preliminary tests were undertaken to demonstrate feasibility for active devices.

The primary mechanism behind direct bonding relies on the macroscopic dispersion van der Waals forces. Through suitable activation stages, this can be enhanced via the presence of longer-range hydrogen bonds. Post-bonding, annealing treatments can then be conducted to develop covalent bonds between surfaces, depending on the materials in question. For this project, chemical-assisted direct bonding, coupled with high temperature annealing, was chosen to maximize the potential bond strength. In addition, a plasma-activated approach was also investigated, developing the bond through extended annealing to produce similar strengths. The presence of alumina in both materials allows for the development of oxygen-rich surfaces through chemical activation, which in turn can be developed into high-strength, covalent bonds through annealing stages. An appropriate anneal was determined for each activation route to achieve the required bond strength and resistance to liquid ingress for subsequent mechanical dicing and polishing processes.

5.2 Surface inspection

As detailed previously in Chapter 2, to facilitate direct bonding, surfaces to be joined require precision polishing to the nanometer scale. Typically, a flatness of at least $\frac{\lambda}{10}$ (@633 nm) with an RMS roughness of <1nm is desired for successful bonding. Samples used in bonding were segments of diced 660 µm-thick sapphire wafers, ∅12.8 mm x 3 mm thick Nd:YAG and ∅12.7 mm x 4 mm YAG. Initial bonds were conducted using single-side polished (SSP) sapphire, before progressing to double-side polished (DSP) sapphire.

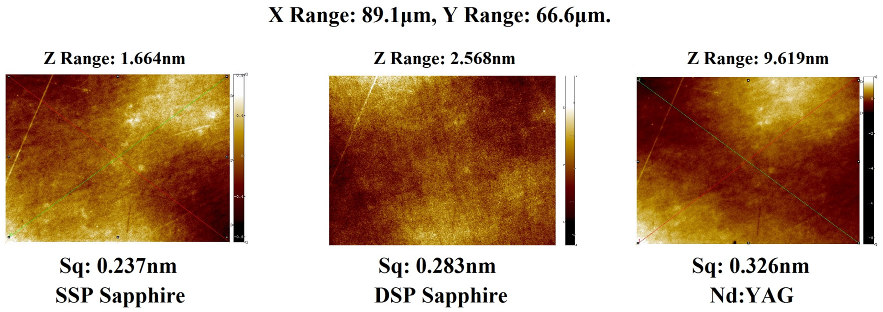

Figure 5.1: 100x magnification images of SSP sapphire, DSP sapphire and Nd:YAG polished faces, captured on a white light interferometer. S_q is the surface RMS roughness

Sapphire and YAG surfaces were inspected using a Zescope white light interferometer at 100x magnification. Figure 5.1 shows 2D surface maps for the SSP sapphire, DSP sapphire and Nd:YAG material, where S_q is the RMS roughness for each. All samples exhibited RMS roughnesses of <0.5 nm. Some pits were present on a small number of the YAG faces, but were localised to a few nm and did not rise around the edges so were not considered to inhibit bonding. Measurements were taken at the centre and four edge regions on the samples. At the time of experimentation, capability to measure the long range flatness of samples was not present. Attempts were made to inspect the surfaces at 2.5x magnification and stich together images, however this resulted in artificial curvature being added to the surface maps and as such could not be relied upon. Based on suitably low RMS roughnesses, the surfaces were deemed suitable for bonding.

5.3 Developing the bond

5.3.1 Initial stages - HF treatment

Bonding was conducted in a class 1000 (or ISO 6) cleanroom facility, with contact made under a class 100 (ISO 5) laminar flow bench. Initial bonds were conducted between the SSP sapphire and Nd:YAG samples, using the hydrophobic - HF treatment described in Chapter 3.7. At this stage, the plasma stage consisted only of O_2 plasma applied for 1 minute. This short O_2 process was initially used as a simple cleaning stage before further literature research led to an O_2 and N_2 activation process being introduction. Following the 5 minute dip in 1% HF, samples were rinsed thoroughly with DI water and placed into contact.

The sapphire wafers provided a base onto which the Nd:YAG samples were lowered. Optical contact did not form immediately, but by shifting the Nd:YAG gently on the surface, a region was found at which the Nd:YAG locked in a position, and a spontaneous contact wave spread over the interface in seconds. It is believed that the fluctuations in each surface may prevent close enough contact at all places on the sapphire surface, but when a suitable region of sapphire is located, the vdW and dipole forces then pull the two faces together, spreading the contact. Any attempts to apply pressure by hand led to flexing of the sapphire layer, separating the two materials. When released, the contact wave spread across the interfaces once more. The ease of separation showed how weak the initial optical contact formed was.

The bonded pieces were left under in a spring-loaded jig (Logitech BJ2 Thin Section Bonding Jig) under ∼2kg mass on a flat surface for around 20 hours. The jig force was not believed to be a crucial part of the bonding process, instead acting as a way to secure the bonds and potentially limit voids by maintaining a close contact between bonding faces. Figure 5.2 shows two bonded pieces before and after an annealing process. Both bonding interfaces were largely void-free, but inconsistent. One interface displayed a central void, and the other a small void at the bond edge. The bonded samples were then ramped to 350°C at 3°C/min, annealed for 8 hours before ramping to RT at the same rate. Neither bond showed any visual change during annealing.

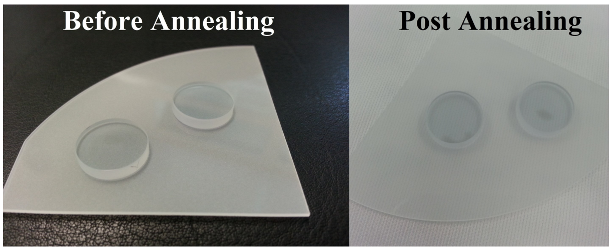

Figure 5.2: Direct bonded Nd:YAG and sapphire before and after 350°C annealing. Each bond interface appears majority clear, with a central void visible in one and toward the edge in the other

5.3.2 Enhancing strength & plasma activation

Bonded Nd:YAG to sapphire composites from the initial HF-bonded approach were subjected to a submersion trial to assess the bond's capability to survive dicing and polishing procedures. While submersion in water did not show any immediate effects, a short ultrasonic treatment of 5 minutes led to separation of the bond. It was therefore determined that the current bonding procedure was unsuitable for dicing and polishing of samples. Based on the requirement for higher temperatures in hydrophobic bonding of silicon wafers - detailed in Chapter 2.2.3 [47] - the annealing time and temperature were increased to 50 hours at 800 °C. The longer time was chosen to give additional time for any trapped water to escape the bond, maximising strength. In addition, the plasma cleaning process was extended to include an N_2 stage as detailed in the short plasma activation described in Chapter 3.7. The N_2 plasma was introduced based on activation procedures described in literature [30].

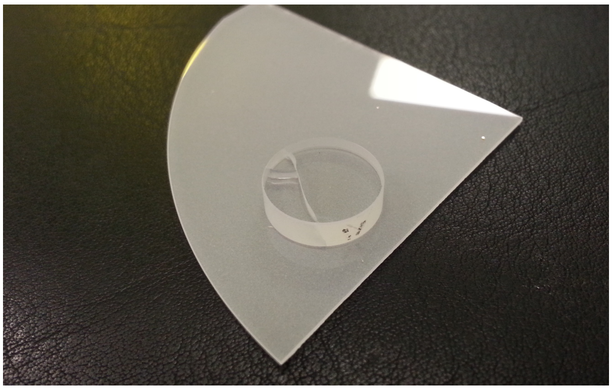

Figure 5.3: Direct bonded YAG and sapphire. The bulk YAG has fractured from stresses during heating but the bond has held underneath

Multiple YAG to sapphire and Nd:YAG to sapphire bonds were conducted using the updated cleaning and bonding procedures. Voids arising from contaminants were still present at the bond interfaces, but the frequency and size of debonded areas improved via adjustments to the bonding procedure. Following annealing, one of the YAG pieces had fractured as shown in Figure 5.3. While fractures are not desired in either material, the bond was maintained on either side of the fracture, indicating either a strength above that of the bulk YAG or a flaw in the YAG leading to a stress fracture. Fracturing was likely caused by difference in CTE between the two materials. When heated rapidly, stress fractures can occur in one material. The fractures appear more commonly around voids in the bond interface, likely due to minor differences in orientation for the bonded regions on either side leading to stress on the connecting bulk material.

The thickness of the YAG and Nd:YAG samples prohibited dicing with the equipment available. Therefore, following the improvements to the bond strength a number of the Nd:YAG samples were worked down to a thickness of 450 µm, polished to the same specification as before. Two bonds were completed using the HF approach for these samples. Bonding was successful, but due to mishandling of the sample, bonding faces were touched while being brought together. As a result voids from contaminants were introduced to the bonds. These bonds were prepared for dicing tests.

In addition to the HF-bonding approach, a purely plasma-bonded method was tested for the YAG/sapphire bond, using the short plasma activation detailed in Chapter 3.7 as the final activation stage. This approach was chosen as a balance between the HF activation and extremely hydrophilic Piranha etch which was deemed unsuitable. Contacting between surfaces was achieved spontaneously after shifting on the surface, then the contact wave was encouraged to spread across the surface by gentle rolling of pressure over the bond area. With no requirement for acid treatment, handling of samples was drastically reduced in difficulty, reducing the quantity of voids present in the bonds. Figure 5.4 shows a comparison between the two bonding approaches. Annealing methods were initially kept the same between activation methods, ramping at 1°C/min to 800°C before a 50 hour dwell and ramp down at 1°C/min.

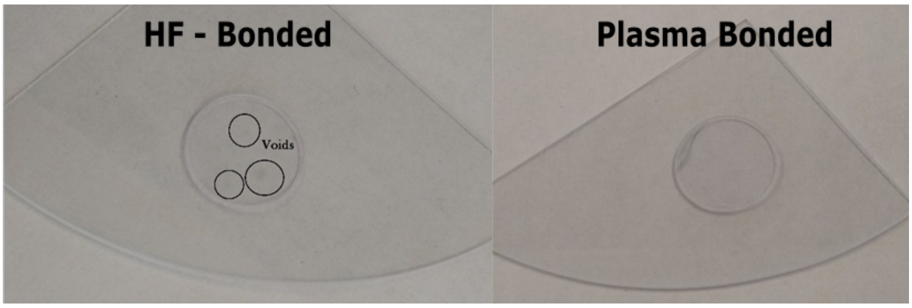

Figure 5.4: Nd:YAG/sapphire bonds activated via HF and Plasma. The plasma-activated bond shows far fewer voids and contaminants at the interface

5.4 Robustness performance trials

5.4.1 Ultrasonic submersion

The fractured YAG-sapphire bond conducted using the HF approach (Figure 5.3) was then tested in a series of ultrasonic trials to observe its resistance to liquid and agitation while submerged. First, the bond was subjected to an extended DI water rinse and nitrogen dry. No visual change was noted. Inspection was focused around a region of contaminants at the edge of the bond, close to the major fracture line visible in Figure 5.3, as these were expected to be potential weak points to allow liquid access. The bonded sample then underwent a 5 minute, and then 10 minute DI water submersion. Again, no change was noted. The composite was subjected to five minutes submersion in an ultrasonic DI water bath. Once again, no change was observed, surpassing the previous bond type.

Finally, the composite was submerged in an ultrasonic IPA bath for 10 minutes. Figure 5.5 shows a microscope image of a debonded edge region before and after the IPA ultrasonic bath. The solvent shows a clear outline in the second image, but is restricted to the debonded region, showing no signs of damaging the bond further. After a short rest at room temperature, the solvent fully evaporated from the region. The plasma-activated approach was also tested under the same conditions, also showing no deterioration from submersion. Both methods were deemed suitable for resistance to liquids.

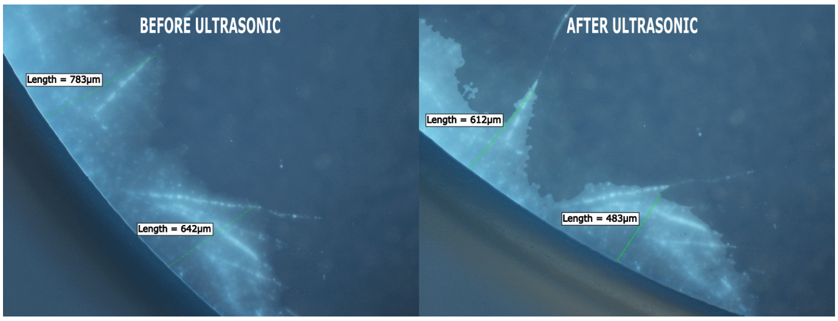

Figure 5.5: Microscope inspection of a debonded region in the YAG-sapphire interface before and directly after 10 minutes submersion in an ultrasonic IPA bath. The liquid enters surface flaw and contaminant lines but does not progress beyond the already debonded region

5.4.2 Cryogenic cooling

A HF-activated bond was subjected to cryogenic temperatures to test the durability of the bond and potential for use in these regimes. The fractured YAG-sapphire bond was used once, with fracture flaws once again noted as potential failure points. The bond was first cooled by resting upon a metal frame which stood within a bath of liquid nitrogen. The temperature of the sample was monitored via a thermocouple on the sapphire surface, close to the YAG. Cooling was produced by adding more liquid nitrogen to the bath, resulting in a staggered temperature reduction, dropping rapidly with each input of liquid nitrogen. A minimum temperature of -161°C was reached and maintained for several hours. The bond was held in an open air environment which acted as a limiting factor for this temperature. During the first cooling stage, no change was noted at the bond interface.

While adding additional liquid nitrogen, a small quantity was accidentally poured into direct contact with the bonded composite. This resulted in large amounts of condensation forming across the composite, as well as a large thermal shock. When inspected following this, debonded regions had appeared in multiple locations at the bond edge. Figure 5.6A shows the bonded piece displaying fringe patterns in the failed regions. It is believed that this deterioration would not have occurred without the thermal shock or condensation.

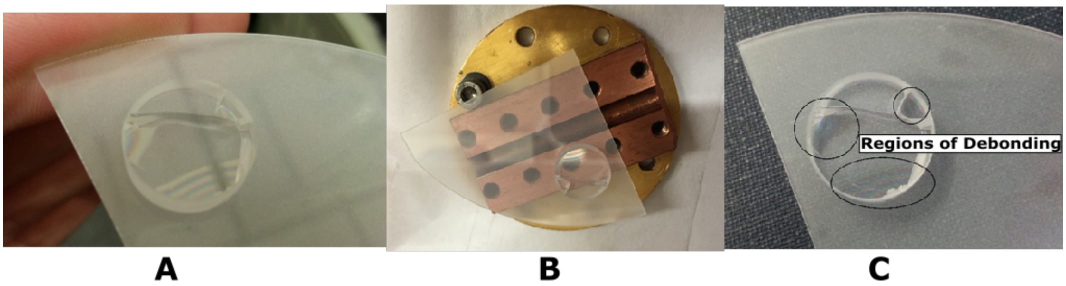

Figure 5.6: A) YAG-sapphire bond after damage from liquid nitrogen and condensation. B) The YAG-sapphire bond mounted onto the copper plate for cooling, and C) the YAG-sapphire bond following the vacuum chamber cooling. Highlighted regions show no further deterioration of the bond

A second test was conducted by mounting the bonded sample to a copper plate and in a liquid nitrogen dewar, enclosing the composite in a vacuum. The bond was cooled via conductance through the copper plate connected to the cold finger of the liquid nitrogen dewar. The liquid was added gradually to produce a more consistent cooling rate. The bond fidelity was observed by camera during cooling. Figure5.6B shows the sample attached to the copper plate. After lowering to -184°C, the sample was left to warm to room temperature over a number of days. Inspection revealed little change caused by the cooling procedure, with no increase in the debonded regions, as shown in Figure5.6C. It is therefore believed that, provided isolation from condensation or extremely sharp thermal shock, this bonding technique is suitable for cryogenic environments. Figure 5.7 shows the recorded cooling rates for each trial. Mounting within a vacuum isolated cryostat is recommended to create a smoother rate of cooling and avoid condensation forming on the bonded composite.

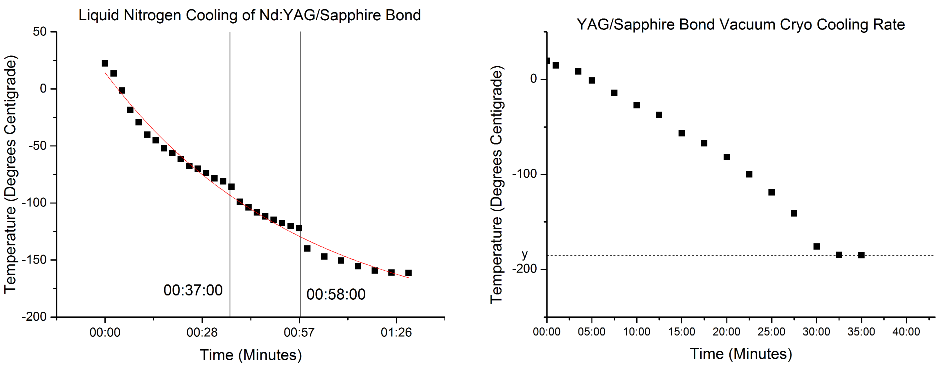

Figure 5.7: Temperature over time for the two cryo-cooling trials. The first, open-air trial produced a staggered exponential rate (vertical lines mark the addition of liquid nitrogen), while the second, vacuum chamber cooling provided a roughly linear rate to a lower minimum temperature

5.4.3 Bond dicing

A final test of the bond's mechanical robustness came through dicing of the bonded composites. Two bonds, one treated via HF and the other plasma were diced using a Disco Automated Dicing machine. The HF-bonded piece held a number of voids at the interface, while the plasma piece was largely void-free. The HF-bonded composite was diced into a 6x8 mm rectangular piece and showed no signs of deterioration, as shown in Figure 5.8. The plasma piece, however, failed across a large portion of the diced piece, and all sections cut away from the main piece also failed as bonds. As the blade diced through the material, liquid was able to enter the interface between the two surfaces, creating either a large void originating at the diced edge, or separating the two samples entirely. The current HF-based activation was deemed suitable for achieving the strength required to dice samples.

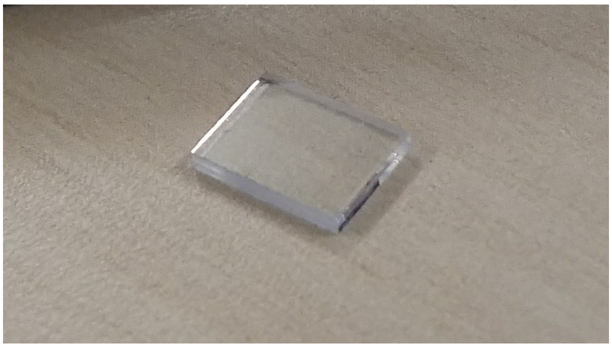

Figure 5.8: The HF-bonded composite, diced to dimensions 8x6 mm

In order to develop the plasma bond process to a suitable strength, another bonded piece was given a second annealing stage at 800°C for 40 hours under a light mass (~2kg), once again ramping at 1°C/min. The bond interface showed one debonded region towards to edge of the bond, and as such dicing was ordered such as to remove and avoid this region acting as a failure point. The dicing direction and order are shown in Figure 5.9A, where the first cut is designed to isolate the weaker region. Following the additional annealing stage, the plasma bond process was found to produce a suitable strength to withstand dicing. The resulting 5x5 mm piece is shown in Figure 5.9B. Ideally multiple bonds would be conducted using the plasma procedure to ensure bonds would reliably withstand dicing, but due to time and sample constraints this was not possible during the course of this project.

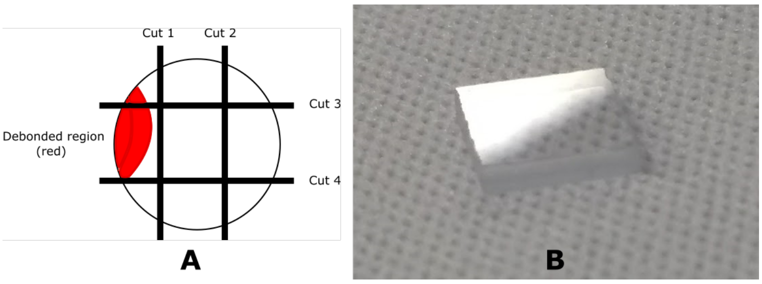

Figure 5.9: A) The dicing plan for the ∅12.8 mm plasma-bonded Nd:YAG to avoid sensitive regions and B) The diced, 5x5 mm bonded composite

5.5 869nm pumped 1064nm laser oscillator

To further test the capabilities of the bonded composite, a laser cavity was built around the composite, using the Nd:YAG layer as a gain medium. The composite's resistance to localised heating through heatspreading benefits of the bonded sapphire layer were investigated by pumping with a 869 nm-locked diode-laser array (bar) to produce a 1.064 µm laser. The aim was to create an optical structure that would capture and guide the slow-axis-dimension of the diode-laser beam, and as such form a pump waveguide, while at the same time provide sufficient thickness in this axis to allow a laser mode to pass unfettered, essentially a 1-dimensional version of mm-diameter crystal rods [84].

5.5.1 Sample preparation & cavity design

Following successful dicing, end facets of the 8x6 mm Nd:YAG-sapphire composite were polished in-house using cast-iron plate for lapping and a polyurethane plate for fine polishing The bonded composite was mounted in line with a blank YAG piece, such that the end facets created a symmetrical front of YAG-sapphire-YAG. It was hoped that this would minimise rounding at the interface edge between the two materials, which erode at different rates due to their toughness. Images of the polished faces were captured at 40x magnification, as shown in Figure 5.10. The interface is clearly visible as a void-free line between the two materials. The dicing process results in some minor chip damage to the outer corner of each material, visible at each edge. This could be removed via re-lapping and polishing of the large faces but would result in thinning of each layer.

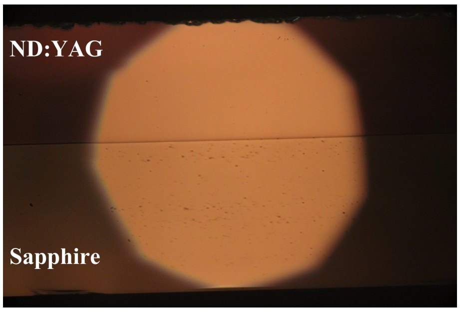

Figure 5.10: 40x magnifcation image of the NdYAG\sapphire end facet following polishing. A brief solvent wipe was given to the faces before inspection, however small specks on the polished faces are visible (largely on the sapphire face). These are attributed to dirt or residue from the polishing process

The large face of the sapphire layer of the bonded composite was soldered to a copper heatsink. The structure was end-pumped using a 50 W diode-laser-bar, (19 emitters, 50% fill-factor 9.5 mm bar-width), wavelength locked to 869nm via a Volume Bragg Grating (VBG) to match an in-band absorption line of Nd:YAG. The diode bar and VBG were found to wavelength-lock most effectively at 25°C, with its temperature maintained by a water cooling system. Figure 5.11A shows the setup, with the slow axis in the plane of the schematic and the fast axis normal to it. The fast (and slow) axis (FAC/SAC) collimated diode-laser output was focused by an aspheric cylindrical lens of numerical aperture (NA, defining the range of acceptance angles of light into the lens of guide) 0.55, L1, f = 10 mm, through the in-coupling dichroic mirror M1, into the 450 µm-thick Nd:YAG layer, which has a numerical aperture of 0.47. Defining the tangential axis as the one guided in the YAG layer, the sagittal axis was unconditioned after the FAC, that is it was allowed to propagate 200 mm before reaching the medium, with a ~1 mm second-moments full-width in the sample.

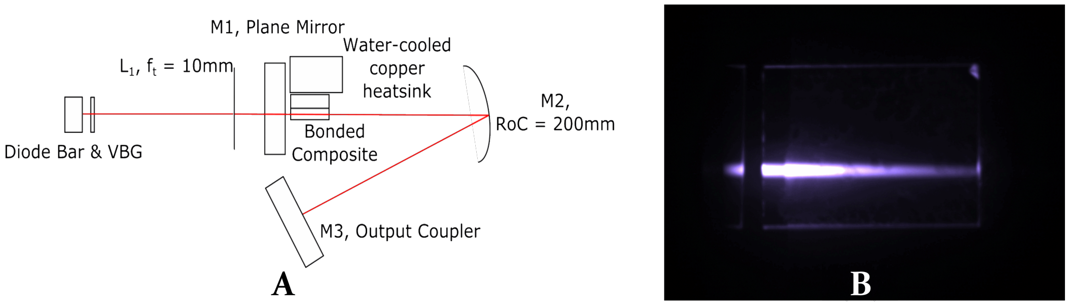

Figure 5.11: A) Oscillator setup for the bonded composite laser. A VBG-locked 869nm diode bar pumps the Nd:YAG layer for the 1064nm laser cavity. And B) Fluorescence from the top of the lasing composite, viewed through a long-pass filter to reject the pump light

Mounted on a 6-axis stage, the position of the bonded composite was adjusted to optimize the pump-launch. A simple V-cavity configuration was set up with M2, the turning mirror (which had a 200 mm radius of curvature), angled at ~17° in the tangential plane.

A flat 85% reflective output coupler (OC) mirror, M3, was positioned in order to maximize the lasing output. This preliminary configuration, was primarily configured to test the quality of the bond and realise laser output. Lasing on the dominant 1064nm line, the beam at the OC, was reimaged via a telescope system onto a CCD camera, enabling the cavity modes to be assessed. Figure 5.11B shows the lasing composite viewed from the top face through an RG1000 long-pass filter, with the 1064nm fluorescence clearly visible across the Nd:YAG length.

By measuring the laser output power while increasing the diode bar driving current, an initial slope efficiency of 12.5% was recorded using a 15% transmission (T) OC. Due to the index step between Nd:YAG (1.82 @ 869nm) and air, Fresnel reflections would result in a loss of around 8.5% at each interface, assuming normal incidence. In order to mitigate this issue and improve efficiency, the sample was unmounted in order to deposit an AR coating of MgF_2 on each end facet (in-house). Figure 5.12 shows the coated end facets under a 10x microscope objective. The coating appears to have adhered well to the majority of the surface, with a targeted thickness of one quarter of the pump wavelength (~220nm). The composite was then remounted to the copper heatsink.

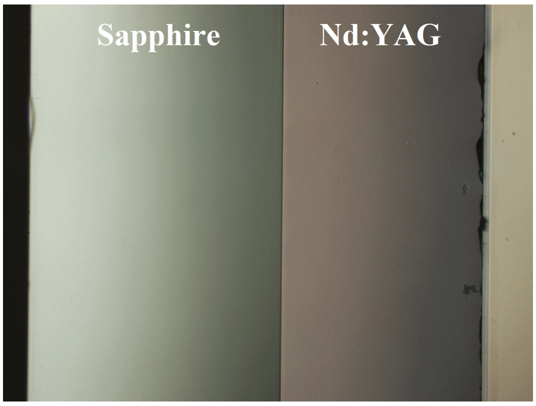

Figure 5.12: 10x microscope inspection of the AR-coated end facet. The AR coating appears as a coloured tint on both faces. No damage is visible to the coating

5.5.2 Laser measurements

With the composite returned to the oscillator, telescope arrangement was constructed to re-image the beam at the OC. Using a 350 mm and 60 mm lens, the beam waist was re-imaged at 0.17x reduction. The beam size around the waist was then recorded for increasing power levels. By comparing the beamsize and beam quality factor (M^2) at M3 with an ABCD model for the laser cavity, the thermal lens within the crystal could be predicted at each power level [85]. Due to the one-dimensional heat flow within the crystal, the tangential and sagittal planes were expected to exhibit differing thermal lensing characteristics, with a more pronounced lens appearing in the tangential plane. However, the beam size in the tangential plane proved difficult to record precisely.

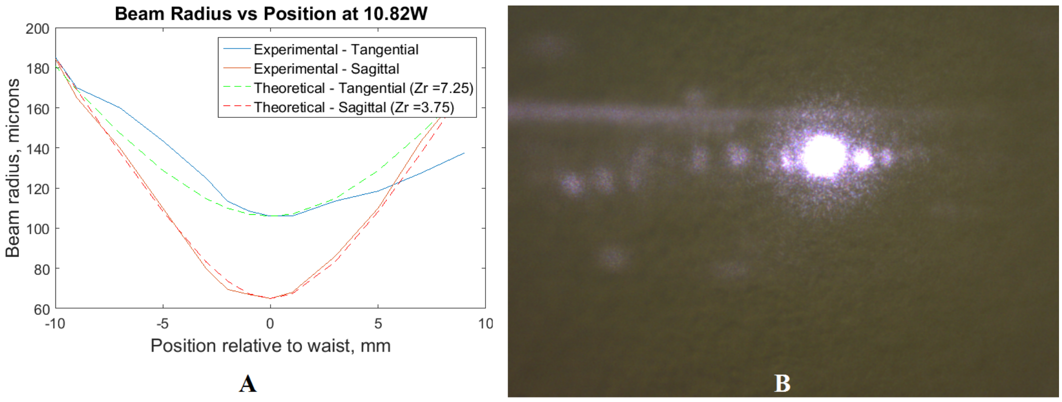

A **B**

Figure 5.13: A) Beam size measurements about the re-imaged waist for each axis with a theoretical fit for Rayleigh ranges (Zr) and B) A captured image of the laser output showing significant additional output around the primary beam

Figure 5.13A shows the recorded beam sizes about the waist for each plane (at ∼11 W input power), along with theoretical plots based on the beam waist size and measured Rayleigh range (Zr) [86]. In the sagittal plane, the experimental results match well with theory. However, in the tangential plane, the experimental beam size shows aberrations about the waist. This behaviour was matched across the full power range, making recording the minima locations in the tangential axis difficult.

When viewing the output beam, a significant amount of additional power is visible outside of the main beam, as shown in Figure 5.13B, which shows multiple additional beams and diffraction effects to either side. As such, it was not possible to predict the thermal lens in the tangential plane of the crystal. The excess light visible was attributed to the high gain from the doping concentration causing large amounts of amplified spontaneous emission (ASE) within the crystal, as well significant diffraction from end facet curvature.

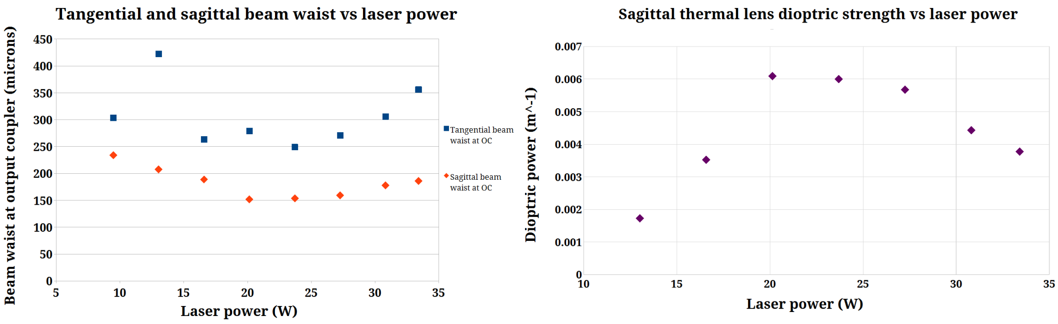

A **B**

Figure 5.14: A) Beam waist size for the tangential and sagittal axis at the OC with increasing laser power. B) Thermal lens strength in the sagittal axis vs incident diode laser power. A clear drop is noted beyond 20.4W of incident laser power

The beam size at the output coupler was modelled for increasing thermal lens dioptric strength. The recorded beam minima and M^2 were then used to calculate the corresponding beam sizes at the output coupler for each power level, and therefore the thermal lens strength. However, the results did not match the theory based on the current cavity design. For low power levels, the experimental beam size exceeded the theoretical model, but thermal lens strength increased with power as expected. However, beyond 20.4W input power, the thermal lens strength appears to reduce again, as shown in Figure 5.14. Due to the aberrations noted, the calculated tangential beam radius fluctuates wildly, but the sagittal beam shows a clear downward trend during the first four readings shown in Figure 5.14A. When converted to calculated thermal lens strength in Figure 5.14B, it appears to show the lens effect decreasing as power rises beyond 20.4W.

From these results it was clear that the current theoretical model did not accurately represent the cavity, indicating some form of additional optical power in the cavity. Due to the simple cavity design, this was assumed to be due to the end facets. Measurements of the facet quality and form were made with a white light interferometer and stylus profiler to see if the lensing effect could be attributed to surface curvature.

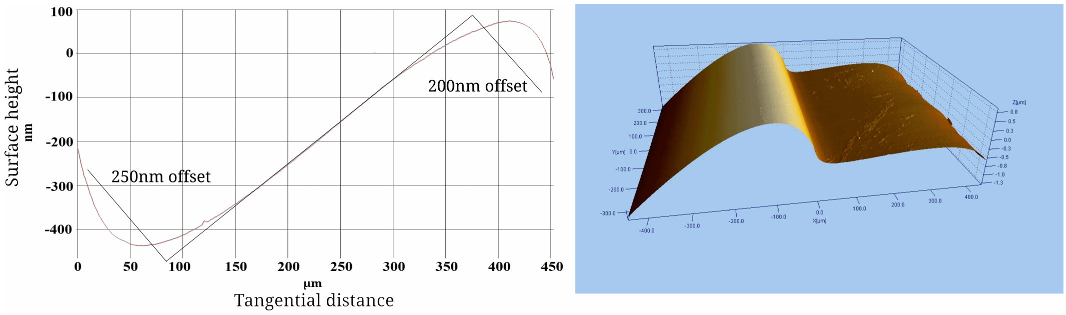

A **B**

Figure 5.15: A) 2D surface profile across 450 µm on the YAG surface (as the tangential axis of the beam would see upon exit), with offset at each edge listed, and B) 3D surface map of the bonded composite end facet covering an area of 900 µm x 600 µm. The interface is clearly visible as a large rise between the left-hand, sapphire side and the right-hand YAG. Both profiles were captured with a white light interferometer

The surface maps in Figure 5.15A and B show a clear distortion across the YAG surface. The difference in toughness between sapphire and YAG causes the two materials to lose material at different rates during the polishing process, resulting in a steep curvature at the sapphire edge. While efforts were made to counteract this by packing the composite between additional YAG pieces during polishing, an improved method is clearly required to obtain a suitably flat surface. The measured facet curvature would create distortions in the cavity unaccounted for by the model.

An attempt was made to account for the facet curvature by modelling the end facets of the crystal as a negative lens of f=-100 mm (combining both facets into one). While this

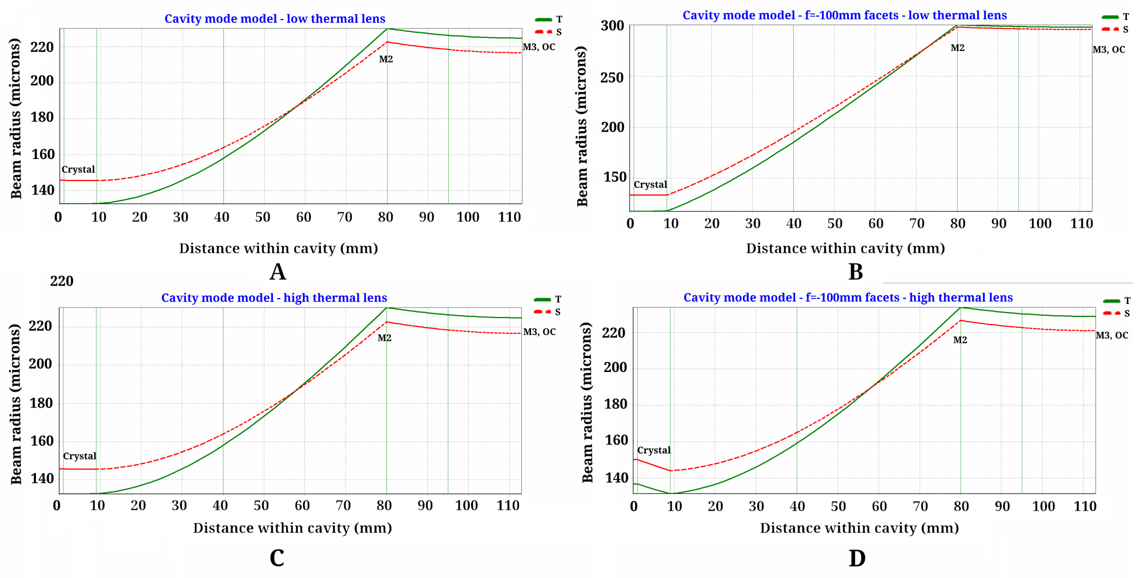

Figure 5.16: Models of the cavity mode for low (A and B) and high (C and D) thermal lens strengths, and with (B and D) and without (A and C) an f=-100 mm lens at the crystal facet

increased the theoretical beam size at low powers (and minimal lensing), it didn't account for the drop in dioptric power with high pump powers. The beam size within the cavity was modelled using software combining standardized ABCD ray propagation matrices for cavity elements (free space, thin lens, mirrors and propagation in a higher index medium) [87]. As shown in Figure 5.16, models for the cavity, both with and without the f=-100 mm lens, predict an increasing reduction in beam radius as thermal lens strength (inverse of focal length) increases. The surface shape recorded did not match that of a parabolic thin lens, and as such it is unsurprising that this failed to account for the higher order features. The warped surfaces are expected to have an impact on the light present outside of the main beam, splaying light in different directions depends on which part of the crystal face is hit, which would effectively degrade the measured beam quality and make it difficult to obtain clear data to compare with the model.

To identify how much power lay outside of the primary laser beam, the laser power was recorded again with increasing pump power, with a pinhole positioned in front of the detector. The pinhole was centred on the primary output beam using an IR card at low powers. Two sets of laser vs pump power curves were recorded, one with a pinhole set to to approximately 1cm diameter to isolate the expected Gaussian output beam from the diffraction, and one with the pinhole opened to capture all of the laser output from the cavity. The primary beam could not be precisely separated from the secondary diffracted beams so the pinhole width was set fairly wide to capture as much of the central beam while blocking the extraneous beams visible through an IR viewer. The power entering the crystal was then recorded by measuring both the power arriving at the crystal position and the power reflected via Fresnel. By angling the crystal slightly, the

Fresnel reflection which remained despite the coating could be captured by the detector. Then, the incident power was recorded by removing the crystal and replacing it with the detector, directly behind the input mirror, M1. By subtracting the power lost in the initial Fresnel reflection from the incident power, the power entering the YAG crystal was calculated.

Figure 5.17 shows the recorded laser values, producing slopes of 20.4% and 31.8% with and without the pinhole, respectively. Plotted across the linear portion of the graph, the opened pinhole results in a significantly higher slope efficiency, increasing by around 11%. The difference between each reading showed that 34% of the total power originated from outside the central beam. A clear tail-off in the slope is also visible for both lines above 20W of incident power, corresponding to the point at which the cavity modelling broke down regarding the recorded thermal lens. This was believed to be clipping of the beam at the edge of the crystal and the overlapping heatsink, due to the thermal lens causing expansion of the beam. This effect, with a portion of the beam reflecting off the gold-coated copper heatsink, could further account for the inability to match experimental values for beam size to the theoretical cavity.

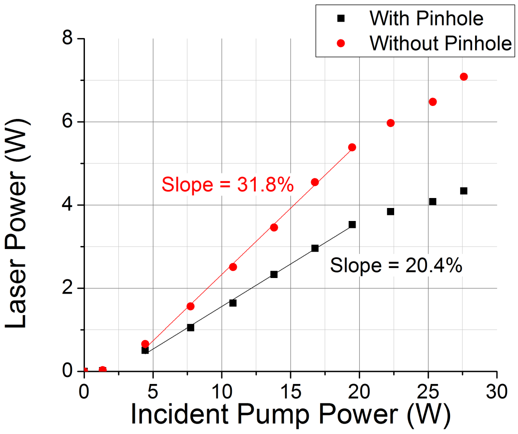

Figure 5.17: Measured laser output against incident pump power. The laser power was recorded once using a pinhole to isolate only the central beam and again without the pinhole

5.5.3 Analysis & improvement routes

Development of a 1.064 µm laser oscillator has demonstrated that the developed process for the sapphire to Nd:YAG bond has potential for use in high-power active devices. The bond showed no signs of damage with 27W of incident pump power focused into the 450 µm active layer with a ∼1 mm wide beam. The high concentration (1.3at.%) of Nd and its resulting heat-load shows the bond is capable of operating under a heavy localised heating, with the sapphire as a heat spreading layer. Producing an output of over 7 W with 4 W in the central beam, the bonded YAG/sapphire composite shows great potential. However, a significant number of refinements are required to advance work in this area.

Producing an ideal end device would require a three-layer, sapphire-Nd:YAG-sapphire bonded composite. In this approach, heat-extraction would be both doubled and create a symmetrical heat-distribution across the active layer, with improved thermal lens effects from the material's $\frac{dn}{dT}$ and allowing for simpler predictions of lensing effects within the cavity. Double sided bonding would increase the production time of such a composite however, requiring the initial bond to be completed and annealed before the remaining YAG face to be bonded was re-polished to a suitable flatness.

Double side-bonding in a single stage was attempted, however it was found that the rear-face of the thin YAG distorted during the bond, reducing it's ability to contact to the second sapphire piece. This problem could be avoided with thicker YAG but thereby defeats the waveguiding and thin-heatspreading properties. An alternate method could be envisaged involving strong pressure applied to the surfaces during bonding to ensure close contact, however this may lead to fracturing of the materials during annealing stages due to restricted expansion. Following bonding, greater care is also required during the end-facet polishing stages. To provide a symmetrical distribution of pressure, it is proposed to sandwich the YAG layer between additional place-holder sapphire pieces during polishing.

The combination of dimensional, material and polishing improvements would work in combination to reduce the significant optical power noted outside of the central beam, likewise improving the slope efficiency of the laser. Regarding the cavity, in the current design in the sagittal plane, mode overlap between the pump and laser is believed to be poor, with the pump collimated to around 1 mm full width, while the laser mode occupies a waist radius close to 140 µm. Combined with polishing improvements, the beam size within the crystal could be more accurately optimised to maximise the mode overlap. This would, once more, reduce effects from ASE and improve the laser efficiency.

With bonding and post-processing refined, the end device could also be improved by adjusting the dimensions of the gain material. A longer crystal (extended in the 8 mm direction) of lower dopant concentration would increase the absorption length, providing a more even heat distribution across the length of the bond and maximising the benefits of the tightly-bonded, sapphire layer and planar structure. In the current design the majority of heat is front-loaded within the crystal, with an-asymmetrical profile in the tangential plane. With all of these improvements taken into account, a reliable technique to produce robust and resilient bonds between YAG and sapphire and utilise the resulting composites into optimised, high-power active systems could be realised.

5.6 Conclusion

This project has successfully developed two approaches to direct bond the dissimilar materials of YAG and sapphire, producing bonds with excellent resilience to a wide variety of environmental conditions and mechanical factors. By refining the activation and annealing process through subsequent iterations, the HF and plasma bonds have been enhanced to show resistance to liquid ingress during ultrasonic agitation, survival at elevated and cryogenic temperatures ranging from 800°C to -180°C, and the strength to withstand abrasive mechanical processes such as dicing and polishing which can be applied to optimise devices following initial production.

The HF-activated approach produced the most resilient bond, capable of dicing after a single annealing stage and tested over the greatest temperature range. The bonded composites even showed signs of strength exceeding that of bulk YAG, maintaining the bond even as the main bulk fractured. However, the nature of handling hazardous acids combined with the rapid transfer required between activation and bonding often resulted in an interface displaying a significant number of voids. While these voids did not induce failure during processing, they could potentially reduce the thermal conductance across the interface or result in optical losses, as well as reducing the potential yield from each bond. The plasma-activated approach produced a reliably clearer interface, but resulted in a weaker bond until annealed for twice as long as the HF-approach. Combining the correct activation and annealing steps, both routes provided versatile bonds to allow for use in a wide variety of scenarios. The HF activation was established as reliably producing a high-strength bond, but with repeated testing of the plasma activation, the cleaner interface combined with the lack of a requirement for a dangerous acid would make this a preferred route.

Through construction of a laser cavity with the active composite as the gain medium, the bond has been tested to survive localised heating through incident power of 27 Watts, with a maximum laser power recorded of over 7 Watts. As the bonded composites demonstrate suitability for use in high-power devices, the efficiency of a direct-bonded laser gain medium could be improved drastically through the material, dimensional and design refinements discussed previously. With the potential to implement a bonded composite in cryogenic temperature laser systems, these avenues offer clear applications to apply the effective and repeatable bonding process demonstrated in this chapter between YAG and sapphire.

Chapter 6

Direct bonding zinc selenide to diamond

6.1 Introduction

Diamond is proving an increasingly important material in optical and electronic devices due to its excellent non-linear (Raman) [88, 89], mechanical and thermal properties. Diamond's unrivalled thermal conductivity ($>1500Wm^{-1}K^{-1}$@300K) [83] is over 50 times greater than that of sapphire ($27\mathrm{Wm^{-1}K^{-1}}$) [90] , making it an ideal material for heatspreading. In addition, diamond's hardness renders it extremely resistant to wear or indentation damage, offering an appealing structural support for more fragile materials.

Zinc selenide (ZnSe) has been demonstrated as an excellent host medium for use in mid-infrared laser operation when doped with chromium or iron [91]. Recent advances with Cr:ZnSe lasers have pushed output powers to 140W in a disk architecture, but significant efforts are required to mitigate the strong thermal lensing effects [92] that arise from ZnSe's high thermo-optical coefficient ($\frac{dn}{dT}$) of $70 \times 10^{-6}\mathrm{K}^{-1}$ [90]. In contrast to diamond, ZnSe suffers from an extremely low mechanical hardness (Knoop 120, compared with diamond's Knoop 5,700-10,400) and has significantly lower thermal conductivity ($18\mathrm{Wm^{-1}K^{-1}}$@298K) [90]. Combination of the two materials is therefore of interest for engineered media, allowing diamond to compliment ZnSe's optical properties through both thermal and mechanical protection. Moreover, the refractive indices of diamond and zinc selenide (2.394 and 2.503 at 1 µm, respectively) [93, 94] make waveguide structures an appealing prospect.

A ZnSe/diamond waveguide could be constructed with a relatively high numerical aperture and a pump-guiding structure with excellent mode selection capabilities [95]. Critically, for example, a Cr:ZnSe waveguide laser with a pump wavelength around 2 µm and emission between 2-3 µm, can be conceived where a diamond cladding could act to provide additional loss for higher-order modes, leading to improved mode selection designs for mid-IR operation. For power-scaling Cr:ZnSe mid-IR lasers, the thin-disk architecture is another promising approach [96], where the heatspreading potential of diamond would provide exceptional performance. However, the mid-infrared absorption of diamond would frustrate operation in the case that the diamond were intra-cavity. As such, the design would require a high-reflectance mirror between the thin-disk and heat spreading diamond substrate. While this is the typical design methodology for traditional Yb-doped thin-disk lasers, direct bonding of diamond to a suitable terminating layer (such as Al_2O_3) in the mirror coating would be required.

Combining diamond and ZnSe presents difficulties due to the notable difference in coefficients of thermal expansion, which limit elevated temperature procedures. Direct bonding has proven a versatile approach, demonstrating success in bonding of diamond to dissimilar materials [97, 98, 54]. In this chapter, joining of diamond to ZnSe is achieved at room temperature, using a plasma-assisted direct bond to produce a void-free, optically lossless and thermally conductive interface. The activation and bonding of both ZnSe and diamond are tested in rigorous trials, starting with bonding of sapphire to ZnSe before advancing to diamond.

To demonstrate the bond's potential for heatspreading in an active waveguide, durability over a range of temperatures and ramp rates was investigated. Localized heating, via an optical pumping scheme, demonstrated that for composite ZnSe/diamond, the thermal lens strength was diminished by several orders of magnitude compared to the bare substrate alone.

6.2 Surface inspection

As discussed in the previous Chapters 2 and 3, direct bonding relies on intimate contact between surfaces. In most cases, a nanometer-scale separation must be achieved in order to facilitate successful bonding, requiring stringent polishing and cleaning routines. Diamond, ZnSe and sapphire faces to be bonded were inspected prior to bonding using a white light interferometer at 5x- (effective 2.5x) and 50x+ (effective 100x) magnifications.

Supplied ZnSe windows and sapphire wafers were flat to $<\lambda/10$, while diamond was polished to $\sim \lambda/5$ (@633 nm). Fig. 6.1 shows 2D surface maps of each material under 100x magnification, including their S_q, the RMS roughness recorded for each. When inspected at 100x magnification, the diamond surface shows clearly separated plateaus of differing heights. Diamond was inspected and bonded on the growth side, where the grain size is nominally 1/5th of the thickness (500 µm for the samples tested) and the surface S_q was lower. Stylus profiler and AFM measurements were attempted to confirm that these plateaus were not an artifact of grain regions showing different refractive indices,

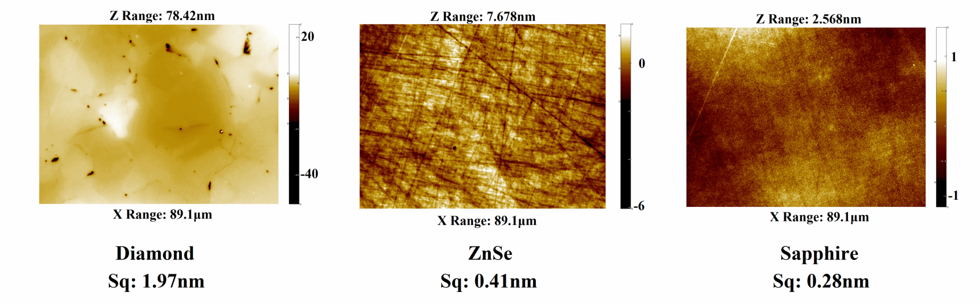

Figure 6.1: Surface maps for diamond, ZnSe and sapphire, where S_q is the RMS roughness at 100x magnification

however stylus profile measurements were unable to be compared due to vibrational fluctuations on the order of 10-20 nm masking the surface height shifts. AFM recorded a larger surface roughness of 3.4 nm, but was not conducted in a clean room environment which could lead to contaminants registering in the image. It proved difficult to obtain satisfactory images through AFM, and as such the surface topology was not able to be confirmed. Fortunately, diamond's poorer surface quality could be counteracted by a greater Hamaker constant [54], increasing the van der Waals force produced during bonding. Therefore, provided the appropriate activation, the diamond surface quality was found suitable for bonding.

6.3 Bonding trials

Before attempting to bond ZnSe and diamond directly, each material was tested in multiple activation processes to identify a suitable approach. Due to the wide availability of well-polished sapphire wafers, ZnSe-sapphire bonding was tested. Following the success in bonding sapphire to sapphire and Nd:YAG (Chapter 5), a hydrophilic approach was targeted. As a material of low chemical resistance, ZnSe is unsuitable for submersion in HF as conducted in the YAG-sapphire bonding, and as Figure 6.2 shows, a test piece identified Piranha etch as unsuitable too, inducing severe damage and discolouration to the surface.

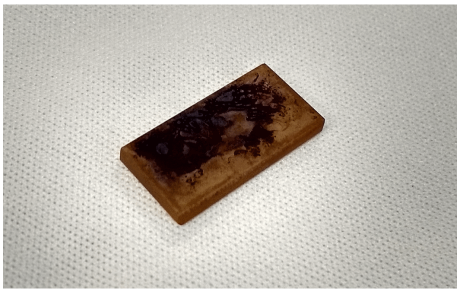

Figure 6.2: Damaged ZnSe following Piranha etch submersion

Plasma activation was therefore considered the most appropriate activation route. The short plasma treatment detailed in Chapter 3.7, which involved 30s of O_2 plasma followed by 1 minute of N_2, was tested on a ZnSe substrate, with surface profiles captured directly before and after. Minimal change in surface roughness was noted, with RMS roughnesses recorded as 0.66 nm and 0.63 nm, respectively.

6.3.1 First contact

A first contact test was made using only solvent cleaning. The ZnSe was cleaned by wiping with acetone before ultrasonic cleaning in acetone, IPA and DI water. The sapphire wafer was given the same cleaning procedure, then submerged in heated piranha etch for 20 minutes. When initial contact was attempted, it was noted that the ZnSe remained fairly hydrophobic despite solvent cleaning, with water beading on the surface rather than wetting. No contact was formed initially, even with pressure applied. A small amount of DI water as added to the bond. After a short period of gently movement, the capillary forces helped hold the two surfaces together. ZnSe-sapphire contacted pieces were then placed into the spring pressure jig, where the bond appeared to develop further.

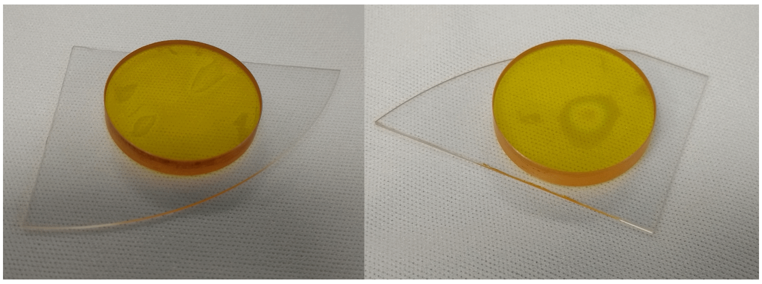

Figure 6.3: 4 mm thick ZnSe contacted with 660 µm sapphire following an ultrasonic solvent clean

It was noted that when pressure was applied, even gently while moving, scratches developed on the ZnSe surface. The two contacted samples are shown in Figure 6.3. A large number of voids are present, arising from contaminants and scratches on the ZnSe surface. Contact failed to occur around any of the damage sites, suggesting surface warping. One contacted sample was placed in a plasma asher for 30s O_2 plasma, followed by 60s N_2 plasma. The asher heats the samples and often encourages water to escape from the bond, separating the samples if poorly held. The bonded piece appeared to survive the sharp rise to >70°C without any change of interface. However, after both samples were left for 72 hours at rest, both samples had deteriorated severely, likely due to continued water evaporation from the interface. The widely spread fringes visible in Figure 6.4 indicated a poor contact was formed, and minor flexing of the sapphire wafer saw big fluctuations in the bond region. The poor contact was not unexpected given the lack of an activation stage to render ZnSe hydrophilic.

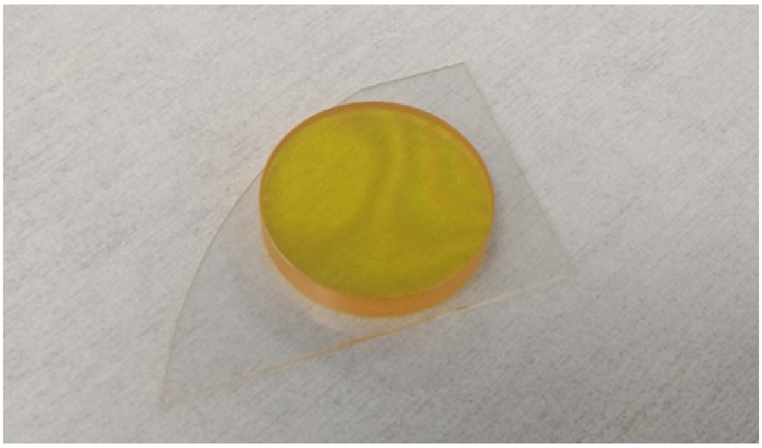

Figure 6.4: The ZnSe-sapphire bond showing significant reduction in the bond region following 72 hours at rest

6.3.2 Contact angles

Hydrophilic activation processes were tested on both ZnSe and diamond to find suitable approaches. To judge the effect, water droplet contact angles were recorded before and after treatments. Diamond and ZnSe are both not super hydrophilic materials, and following an acetone wipe measured average contact angles of 40±3.6° and 70±2.9°, respectively.

6.3.2.1 180°C sulphuric acid

Boiling sulphuric acid is a common method for cleaning diamond, as well as in hydrophilic surface activation. A heated sulphuric acid bath was tested to activate the diamond surface. Sulphuric acid was heated to 180°C before submerging the diamond samples for 1 hour. A first trial of this approach saw significant change, with the water wetting to the surface (<5°). However, repeated testing showed unreliable results, with sometimes only a marginal reduction seen. It is believed that the unreliability may have arisen through an unstable temperature for the acid. It proved difficult to sustain a temperature of 180°C, with temperature recorded to fluctuate between 160 and 180°C. In addition, at temperatures this high, the sulphuric acid began to boil off, releasing a large quantity of vapour. Figure 6.5 shows a comparison between diamond samples with and without treatment. While some success was seen in developing a hydrophilic surface state through this approach, the long treatment time required with aggressive acids meant this route was ultimately halted in favour of the successful plasma activation.

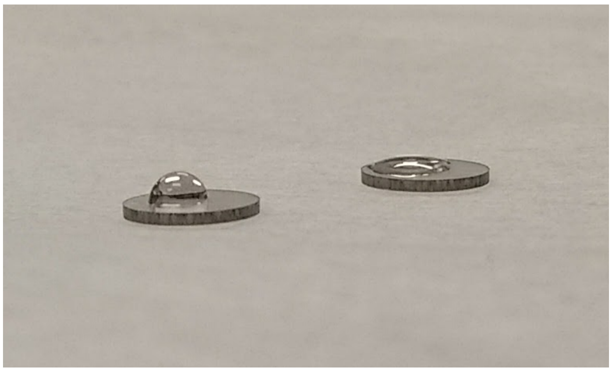

Figure 6.5: Comparison of water deposited on an untreated and sulphuric acid treated diamond surface

6.3.2.2 Plasma activation

Both ZnSe and diamond were subjected to short plasma treatments (short and long plasma treatments were detailed previously in Chapter 3) following a brief acetone wipe. The ZnSe contact angle was reduced to 7.5±0.8°, while diamond was reduced to 8.2±0.7°. It was noted that even a single wipe to the surface using clean-room grade wipes on plasma or sulphuric activated samples would result in a sharp increase in contact angle to around 30°. When combined with a preceding ultrasonic solvent clean, the water then wet to the ZnSe surface completely, with an angle <5. Diamond, as much tougher material, was expected to be more resistant to plasma bombardment than the softer ZnSe. Adding an additional long plasma treatment also reduced the diamond angle to <5°. Figure 6.6 shows water droplets deposited on ZnSe with and without plasma activation. The plasma-treated surface sees the water completely wet to the hydrophilic surface.

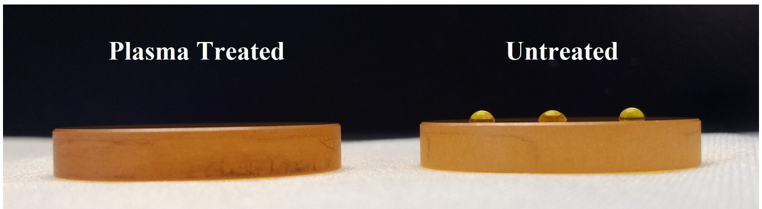

Figure 6.6: Water droplets placed on plasma-treated and untreated ZnSe. The activated surface becomes strongly hydrophilic

To test the lasting effect of the plasma treatment, ZnSe samples were treated by the plasma activation, then left for period of time either submerged in DI water or at rest in atmosphere. The contact angle was recorded after 5 and 15 minutes submerged in DI water, and after 1 hour in atmosphere, as shown in Figure 6.7. Contact angles below 5° were below measurement threshold and were set to 2.5°. Minimal change was noted after 5 minutes submerged, with the angle rising to around 11° at the end of the hour. It is clear, then, that the surface becomes less active over time, but the process is relatively slow compared to the bonding procedure. Of far more pressing concern is the risk of any contaminant attaching itself to the highly active surface directly after activation. It is of paramount importance to conduct bonding as soon as possible following treatment. With plasma activations identified to render each material hydrophilic, bonding trials began.

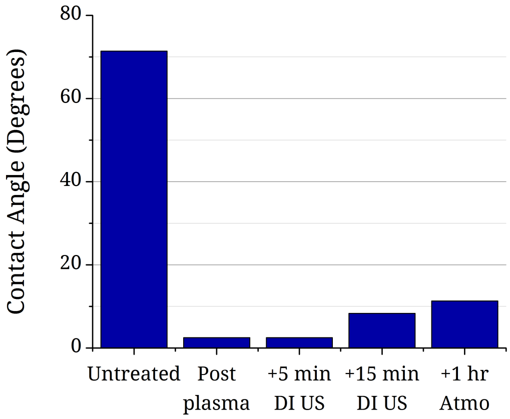

Figure 6.7: ZnSe contact angles recorded before at instalments after plasma treatment

6.3.3 ZnSe-sapphire bonding

Two ZnSe samples were prepared for contact with sapphire, using ultrasonic solvent cleaning. The ZnSe was kept in DI water while waiting for the final 20 minute Piranha Etch treatment of the sapphire, then run through short plasma treatment. Neither sample contacted spontaneously, but when a small quantity of DI water remaining from the ZnSe DI water bath was applied to the interface accidentally, one piece gripped, producing a clear, void free interface across the entire surface. The second piece, however, would not grip until shifted around to help the majority of the water evaporate from the bond. The interface showed different hues, indicating a weak bond held purely by the water. Both pieces were put into a pressure jig and loaded to approximately 2kg of mass.

Inspected after 24 hours, the weaker bond had begun to dislocate at the edges as water evaporated. The clear bond piece, however, showed little to no change. The two bonds are shown in Figure 6.8. Following a further 24 hours, no change was noted.

6.3.4 ZnSe-diamond bonding

Based on the previous results, a plasma assisted bond was tested between ZnSe and diamond. Both samples were wet-cleaned with ultrasonic acetone, IPA and DI water baths. Both ZnSe and diamond were then dried and given a short plasma treatment.

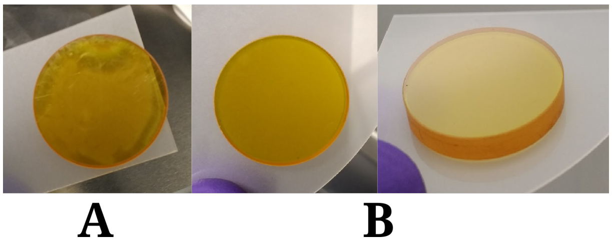

Figure 6.8: A) A poor ZnSe-sapphire bond showing shrinkage at the edges, and B) Two images of a clear, void-free ZnSe-sapphire bond

The ZnSe was then removed and placed in a DI water bath while the diamond was given a further, long plasma treatment. Contact was made within 10 minutes of treatment to reduce the chance of contamination. The ZnSe sample was then dried using a nitrogen line and the diamond sample placed into contact. As expected due to the diamonds poorer surface quality, no spontaneous contact occurred. However, when a small quantity of water (∼50 µl) was applied to the interface again, a contact wave spread rapidly across the surface. DI water saturates the surfaces with OH bonds, then capillary forces draw the faces together as it evaporates, bringing them into the short-range regime of hydrogen and van der Waals forces. Bonded samples were then left under a 2.5kg weight for at least 24 hours. Figure 6.9 shows the bonded ZnSe and diamond sample.

Inspection revealed a clear interface with two small voids visible toward the edge of the bond. The bonding process was confirmed by successfully conducting several further diamond to ZnSe bonds in the same manner. In addition to the diamond to ZnSe composite, diamond to sapphire bonding was conducted using a similar approach. A diced segment of a 0.67 µm-thick sapphire wafer was used as a substrate material. Successful contact was achieved over half of the bond area, displaying a clear interface.

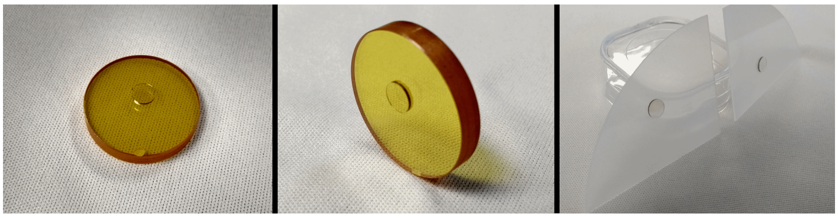

Figure 6.9: 500 µm thick diamond bonded to 4 mm thick ZnSe and 660 µm thick sapphire wafers

The diamond appeared to have stuck rigidly on the ZnSe, unable to be moved by force applied to the side via tweezers. A couple of small, unbonded lines were barely visible at the bond interface. It was hoped that the constriction applied by the surface tension of the small quantity of water will have helped draw the surfaces close enough that the high Hamaker constant of diamond would play an effect in holding the parts together through van der Waals forces. The bonded pair were left in the pressure jig and were inspected after over 50 hours. No change was noted at the interface, as shown in Figure 6.10. After a further five weeks, the bonds showed no difference. The lack of any deterioration indicated that the bond was not reliant on remaining water at the interface, as evaporation over this time would have weakened the bond.

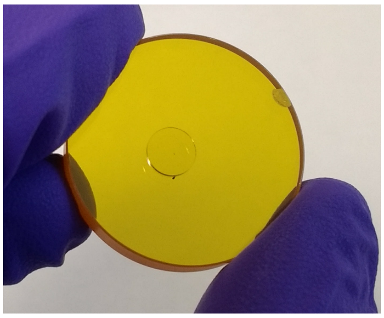

Figure 6.10: The ZnSe-diamond bond showed no change after 50 hours under pressure

The second bond conducted using this technique produced similar results, but with one unbonded region apparent after contact at the edge of the bond, highlighted in Figure 6.11. A small line was noted at the opposite edge, indicating a flaw in the ZnSe surface. The surrounding remained bonded, however, and no change was noted after an extensive rest period of several weeks. The repeatability of the bonding process demonstrates a successful route for achieving ZnSe to diamond contact had been established.

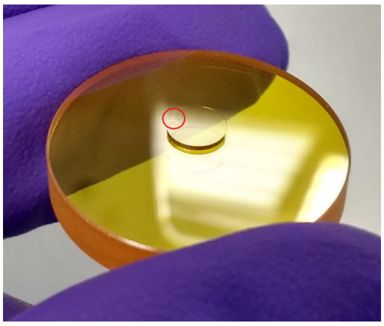

Figure 6.11: A minor flaw was visible in the second ZnSe-diamond bond, highlighted in the red circle as a the lighter shaded region

6.4 ZnSe-diamond composite temperature trials

With a bonding procedure confirmed, trials were conducted to test the composite's limits. Difference in CTE can cause severe stress between bonded materials, and diamond and ZnSe have vastly different CTEs of 1x10^{-6}/°C (at 300K) [99] and 6.8x10^{-6}/°C (at 283K) [100], respectively. As such, the bond is unsuitable for the high-temperatures seen in other direct bonding methods [34].

6.4.1 80°C heating

A series of trials were conducted to test the composite's resistance to temperature change and different ramp rates. One composite was first heated to 80°C in 5°C increments on a hot plate, with a visual inspection at each step. The temperature was measured by a thermocouple close to the diamond on the ZnSe surface. No change was observed up to 55°C, at which point the bond area shrank slightly from the edges. By 80°C an unbonded ring was clearly visible around the central bond, as shown in Figure 6.12A. Sharp, dark-lined 'hard' edges developed around the remaining bonded area, forming a hard barrier to the bond edge. The composite was then held at 80°C for eight hours to test durability. No further degradation was noted. Cooling to room temperature also saw no change to the bonded region, beyond softening of the sharp bond edge lines. Considering the vast difference in CTE, the bond performed above expectations over this temperature range, indicative of diamond's large Hamaker coefficient assisting the bond.

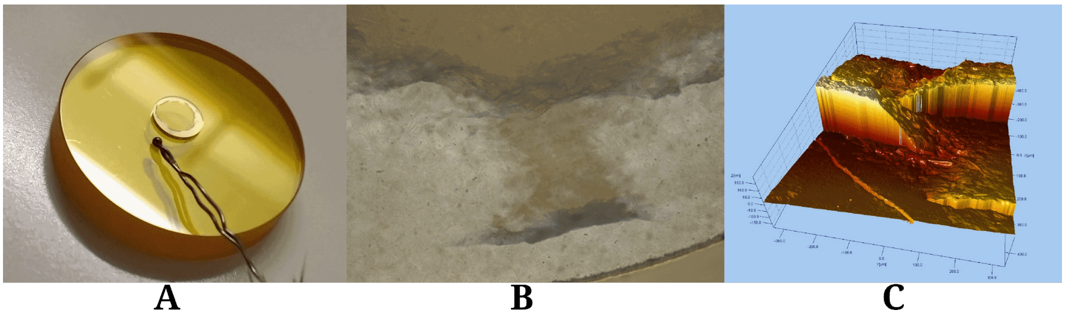

Figure 6.12: A) The diamond/ZnSe composite at 80°C, B) A 10x microscope inspection of the failed bond region and C) A 3D surface map (area of 700 µm x 900 µm, vertical scale of 300 nm) of the ZnSe surface following debonding

The same bond was then heated in an oven environment, ramping to 80°C at 1°C /min before dwelling for 30 minutes. During heating of the sample it was initially believed that the bond expanded during heating, appearing much closer to the edges of the diamond sample, with smaller, partially bonded regions disappearing (believed to have been enveloped). In order to inspect this further, the heating process was recorded to observe the bond behaviour and images captured were compared, as shown in Figure 6.13. It was discovered that the bond region did not expand, instead that a shift in colour, believed to be the start of interference fringes, at the edge of the diamond sample (unbonded region) gave the appearance that the diamond piece was smaller, making the bond look comparatively larger. The small spots of bonded region shown in the RT image are seen to disappear in the heated image, instead showing a band around the lower edge which gives the appearance of a bonded region. Upon cooling, the bond reverted to its previous state, including the smaller contact regions. A longer, 8 hour anneal was also tested, with no noted change.

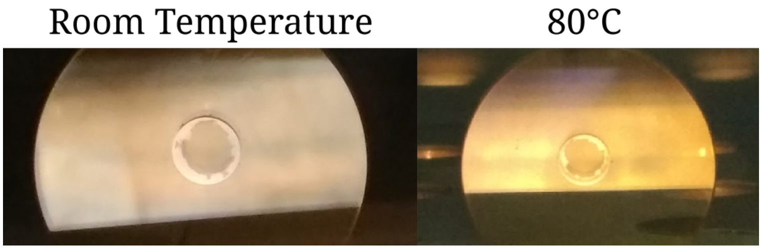

Figure 6.13: The bonded composite at room temperature and 80°C (slightly rotated)

6.4.2 Ramp rates

The composite was then subjected to rapid changes in the 20-80°C range using a Rapid Thermal Annealer (RTA). The bonded sample was ramped from room temperature to 80°C at rates of 1, 2, 5 and 10°C/minute. As before, heating to 80°C caused the bond region to shrink at the outer edges. However, no further damage was observed at the bonding interface due to increases in ramp rate, demonstrating the bond is resistant to sharp changes in environmental temperature.

The ZnSe-sapphire bond with clear interface was also tested at a rate of 10°C/min, showing no deterioration at all. Because sapphire and ZnSe differ less in CTE, higher temperature annealing of the ZnSe-sapphire bond was tested to 500°C. However, this proved too close to the decomposition temperature of ZnSe and caused the material to change structure, clouding over entirely to become opaque.

The ZnSe-diamond bond was then heated with the intention of inducing failure. From 80°C, the bond was heated in instalments of 10-20°C, inspecting after each. At 100°C, the bond was noted to deteriorate further in a notably interesting way. Regions which had formed a hard edge as seen by eye did not retract during heating, resisting the change. As shown in Figure 6.14A, deterioration occurred at gaps between these regions, presumably allowing air into the shifting surface regions and separating the bond.

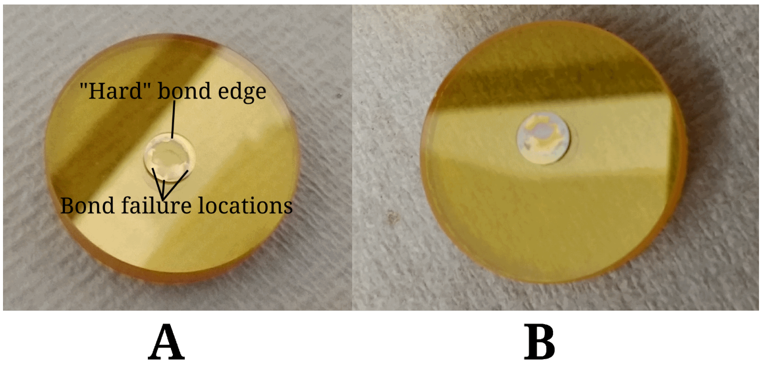

Figure 6.14: A) The ZnSe-diamond composite at 100°C, bond failure occurs in the gaps between 'hard' bond edges, and B) the composite at 145°C, by which point nearly all clarity at the interface has now been lost

The bond was then heated beyond 100°C to induce complete failure. As temperature was increased to 120°C, colour became clearly visible within the debonded regions, developing into a clear interference patterns as the separated regions warped from heating. The debonded area spread to reduce the bonded area seen in the above image by half, though the hard bond edge remained stable. At 145°C the bond began to fail entirely, losing nearly all clarity, as shown in Figure 6.14B.

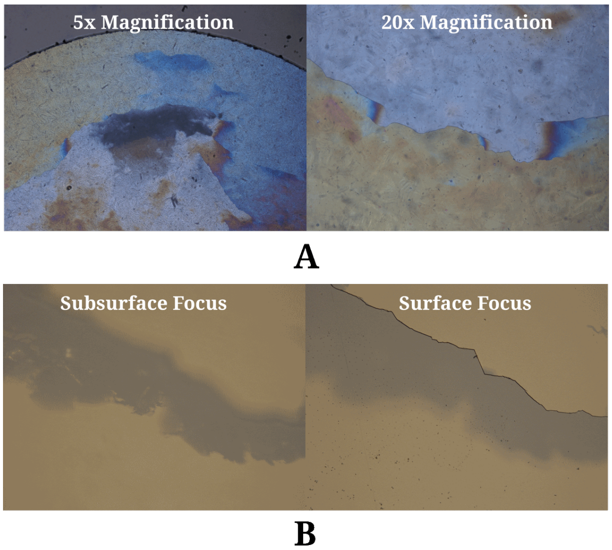

Figure 6.15: A) Microscope images at 5x and 20x magnification looking through the damaged bond interface. Regions of different colour are separated by 'hard' bond lines, and B) Microscope images of a 'hard' line on the ZnSe surface following separation. The subsurface damage is visible near these regions

At this stage it was noted that decomposition of the ZnSe had begun to occur, staining the surface it was placed upon. Due to the mild toxicity of ZnSe, the experiment was cooled until a more suitable environment was available in which to heat the bond. Despite the majority failure of the bond, the two pieces remained together and a clear visual difference was apparent between the fully separated edge regions (appearing grey) and the partial contact areas (appearing coloured). Microscope images were captured of the interface, as shown in Figure 6.15A. The 'hard' bond lines made clear barriers between regions of differing colour (indicating differences in gap height).

6.4.3 Bond separation

After a few days left at RT, a small volume of acetone applied to the interface of the heating-damaged sample during cleaning proved sufficient to separate the two pieces. The ZnSe face was inspected under a microscope. As Figure 6.15B shows, the 'hard' bond edges have a clear height step and show subsurface damage. After bringing the bond to its failure point, a white light interferometer was used to inspect these lined regions. It was noted that these were locations where the ZnSe surface had warped, distorting the bulk substrate to maintain contact with the diamond, as shown in Figure 6.12B and C. It is believed that a crystal grain had been pulled out from the ZnSe surface, maintaining contact with the diamond. Step heights of several hundreds of nanometers were recorded, as shown in Figure 6.16. These occur as the bond strength resists the separation of the two surfaces during annealing. In these regions, the bonding forces have overcome the bulk strength of the polycrystalline ZnSe substrate, causing damage to the surface instead of separating. The corresponding diamond surface was also inspected with the interferometer but having undergone an acetone cleaning stage, no attached ZnSe was noted.

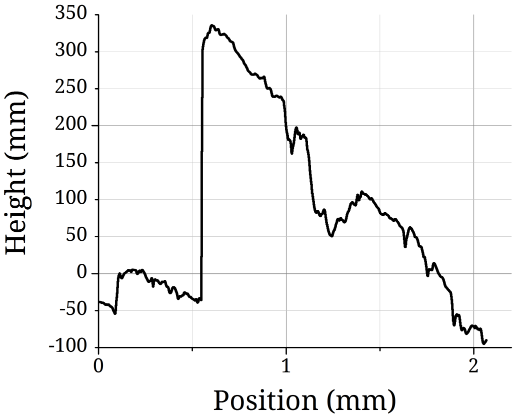

Figure 6.16: A 2D surface profile of ZnSe recorded across a ‘hard’ bond line following bond failure

6.4.4 Elevated temperature bond

Practical use of bonded composites can occur in a variety of environments. In an attempt to expand the temperature range of application, an elevated temperature bond was trialled. The logic behind this was that if the bond were conducted at a higher temperature, this would act as the ‘natural’ temperature of the bond, where it would experience the least stress, the upper temperature limit would therefore be raised by a corresponding amount. Bonding was attempted with samples heated on a hot plate to 80°C directly after activation and during contact.

Unfortunately, bonding at this temperature was not viable due to the rapid evaporation of water from the bond. The added water would escape rapidly from the bond interface, allowing air to enter. While the two pieces held together, the interface appeared patchy, with lighter regions indicating the presence of air gaps, as shown in Figure 6.17. This spread across the bond within 5 minutes, leaving a poor bond interface. From this it was concluded that, due to the requirement of water at the interface, 80°C bonding was not suitable for this process.

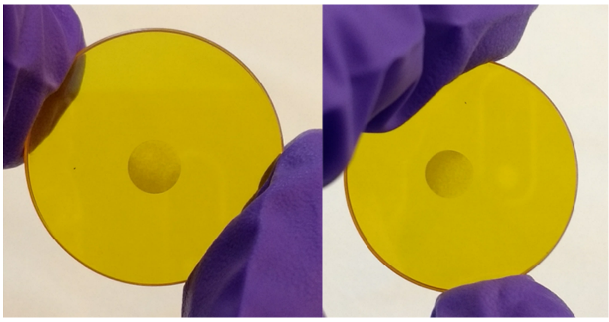

Figure 6.17: A ZnSe-diamond bond attempted at 80°C producing a poor interface

6.4.5 ZnSe-diamond bond cooling trials

A new bonded composite was cooled by resting over a liquid nitrogen bath on a metal frame, as shown in Figure 6.18A. A nitrogen flow was maintained over the sample to stop condensation forming and restrict the rate of cooling. A minimum temperature of -40°C was recorded, cooling rapidly through the addition of liquid nitrogen. The bond was held between -20 and -15°C for 10 minutes. The bond was inspected after returning to room temperature and noted to have suffered minor degradation around the edges of the bonded region, as shown in Figure 6.18. This behaviour mirrors the degradation witnessed with increasing temperature, with the exception of developing hard edges to the bonded region. As with the heated bond, the bond did not recover over this region, retaining the reduction in the bonded area. From this and the heating trials it was established that the composite maintained a majority clear interface over the range -40 to 80°C.

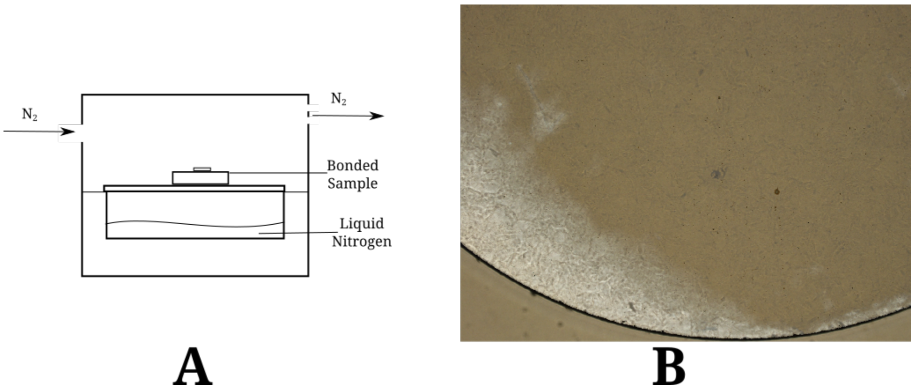

Figure 6.18: A) The liquid nitrogen cooling setup in which the bonded sample rests on a metal frame above the nitrogen bath, and B) Microscope inspection of the bond at 5x magnification following cooling to -40°C. Shrinking of the bonded region is noted along the edges

6.5 Optical transmission trials

With the ZnSe-diamond bond survival well characterised over a range of temperatures, optical trials were conducted next to investigate any distortions caused by the bond interface. Samples were inspected using a simple interferometer setup shown in Figure 6.19A. The interference pattern over a mm diameter region was captured with and without the ZnSe-diamond composite in one beam path. Any air gaps at the bond interface would be expected to distort the resulting pattern. Figure 6.19B shows no distortion was visible in the interference fringes, with reduction in visibility caused by the strong Fresnel reflection losses as the input and exit faces.

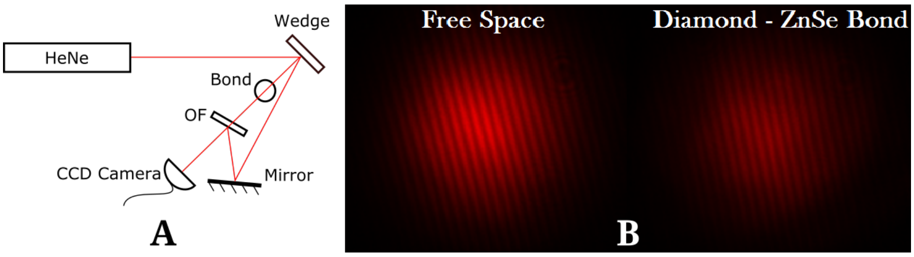

Figure 6.19: A) HeNe interferometer setup for inspecting bond interface optical distortions. One path travels through the bond before recombining with the freespace beam reflected off an Optical Flat (OF), and B) Interference patterns with both beams in free space travel and with one beam passing through the bonded composite

A 1.064 µm Nd:YAG laser was then used to record the composite's optical transmission. By using both clear and damaged section of the bonds, it was possible to compare transmission between the clear and separated regions. Table 6.1 shows the recorded transmission values. In addition, Fresnel reflections for each material were measured at small angles of incidence (taking care to block subsequent reflections), and theoretical values based on the previously listed refractive index for each material were calculated. The recorded results fall in line with those predicted theoretically, with the exception of the failed bond. In this case, the Fresnel calculation is based on four reflections arising from an intermediate air gap. However, in reality the failed region contains areas that remain partially bonded, which could increase the overall transmission and causing discrepancy in results. Additionally, any air gaps could be sub-wavelength in thickness, allowing light to tunnel through.

Table 6.1: Measured and theoretical transmissions at 1.064 µm for bare ZnSe, the ZnSe-diamond composite and a region of failed bond

Region	ZnSe	Clear Bond	Failed Bond
Calculalted transmission from Fresnel Reflections (%)	67.5±3.9	68.7±3.4	46.4±3.9
Measured transmission (%)	65.7±1.5	67.4±0.9	54.8±0.9
Theoretical transmission based on index (%)	66.6	67.8	46

6.6 Localised heating trial

For end use in an active laser system, the primary purpose of bonding the diamond layer was to provide a heat spreading layer in direct contact with the active (Cr or Fe) doped ZnSe. To this end, an investigation in the heat spreading benefits of the bonded diamond layer was conducted. Locally heating a section of the ZnSe surface, the intent was to replicate the heating induced in an active device. A comparison was conducted between bare ZnSe and the bonded ZnSe-diamond composite. In order to simulate absorption heating, a 445 nm diode laser beam was used as 455 nm lies close to ZnSe's bandgap of 2.7ev (459nm) and therefore sees high absorption

A 445 nm diode laser beam was collimated by a lens (L1), f=8 mm, before being focussed by a second lens (L2), f=25 mm, to an approximately 30 µm x 140 µm (radius) waist just within the ZnSe surface. The absorption coefficient at 445 nm was determined to be more than 77 cm^{-1}. To maximise the thermal load density, the 445 nm beam waist was positioned just within the sample's surface, adjusted for the maximum thermal lens.

A 1064 nm laser was directed through the rear ZnSe face to overlap with the region heated by the 445 nm laser on the front surface. The beam was focussed by a lens (L3), f=200 mm, to a radius of 140 µm. The reflection off this face was captured by a lens (L4), f=150 mm, and focused onto a Spiricon CCD positioned at the Fourier plane of the lens, as shown in Fig. 6.20A.

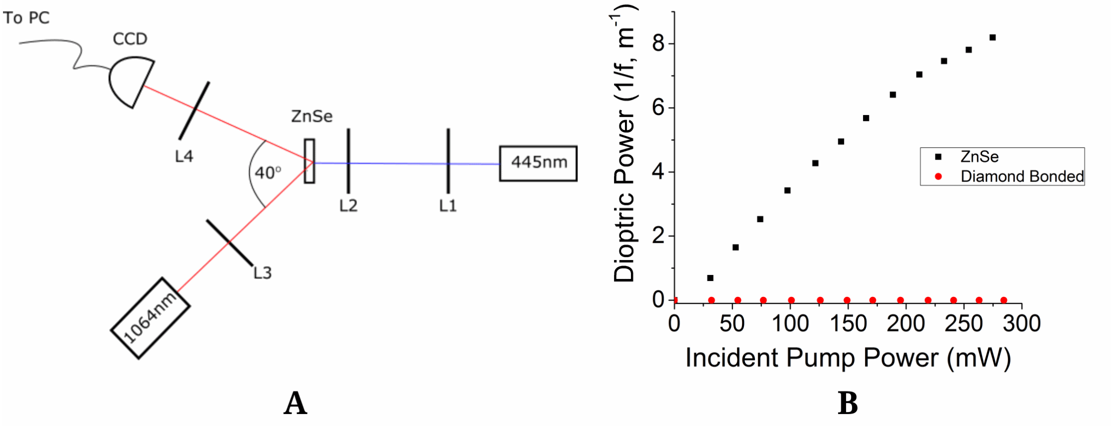

Figure 6.20: A) Pump-probe setup design to compare thermal lensing in bonded and unbonded ZnSe, and B) Optical power of induced thermal lens with increasing laser power

The incident 445 nm pump power was raised to 300mW while recording the probe beam diameter. This was then repeated within an area covered by the 500 µm-thick diamond layer. The optical path difference introduced by the diamond layer was recorded as 720 µm for the 445 nm pump wavelength. The sample was repositioned to locate the region of smallest pump radius before increasing the power again. A maximum thermal lens dioptric power of $8.2\,\mathrm{m}^{-1}$ was observed for bare ZnSe [101]. When scanned within the diamond-bonded region, no thermal lens was detected within the limits of our setup. Figure 6.20B shows the optical power (in diopters) of the thermal lens detected for both regions tested.

6.7 Conclusion

In this chapter bonding of ZnSe to diamond and sapphire was realised. The bonding procedure was developed by testing multiple activation routes before settling on a plasma approach. The short treatment time allows for flexibility in activation, tailoring the duration to each material involved. Using water as an intermediary, and the action of capillary forces to assist, the poorer surface quality of diamond was mitigated, producing a clear, void-free bonding process. Despite large CTE differences, the bond resists -40 to 80°C temperatures, developing 'hard' bond lines as the ZnSe strives to retain contact, dissociating from the bulk.

Optical transmission experiments through the bonded region proved that there was an intimate contact between respective surfaces. When compared to bare ZnSe, a localized heating trial demonstrated exceptional heat spreading with a diamond cap, reducing the observed thermal lens at least two orders of magnitude in our setup. Several engineered optical structures based on such composites can be envisaged for active and passive devices using this technique. Expanding beyond the ZnSe-diamond composite, the process developed was also demonstrated to be adaptable, allowing contact between ZnSe and sapphire, as well as sapphire and diamond. Both these routes hold interest for future research. The repeatable technique for joining dissimilar materials demonstrated shows clear future promise in optical applications and more. Future interest could be directed toward expanding the temperature survival range as well as bonding large scale pieces including wafers.

Chapter 7

Conclusion and future work

7.1 Thesis summary

Reported in this thesis was work conducted to develop direct bonding for use with dissimilar materials for optical applications. The thesis aims to present the advantages of the direct bonding technique before applying it to a selection of material combinations and post-processing techniques. The direct bonding process was developed from the ground up, with stages determined based on available literature for the technique, along with rigorous testing of each process.

Chapter 1 introduced the field of direct bonding from first discovery of the joining phenomenon by Desagulier [11]. A comprehensive review of direct bonding's evolution through history was presented, stretching as far back as 1665. Influential work and the gradual increase in interest was covered, along with the modern transfer in academia and industry from silicon wafer bonding to joining of dissimilar materials. The wide variety of state of the art bonding techniques was then presented, covering the basics of each technique while comparing the current results of each. Finally, the format for the rest of the thesis was covered.

In Chapter 2 the principles behind different techniques used throughout this project were explained in detail. The process of fibre caning was covered, detailing the equipment used, explaining the principles of glass transition temperatures, analysis techniques such as differential thermal analysis and preform production methods.

The underlying science behind direct bonding was then covered. The different interaction forces which contribute to joining materials are covered, including hydrogen, covalent and van der Waals bonds. The importance of Hamaker coefficients and the intimate, nanometre-scale contact requirements between surfaces to be bonded were also explained. The overarching principles of bonding methodologies investigated were then listed, from activation stages to the annealing processes which strengthen bonds by transferring to rigid, covalent bonds. Finally, the details of characterisation tools such as the white light interferometer and microscope, along with the manufacturing equipment such as polishing stages and furnaces were catalogued.

Chapter 3 delved into the development of direct bonding at the Optoelectronic Research Centre. A hydrophilic approach to bonding amorphous borosilicate glass was established through iterative improvements to the steps and apparatus used. Early bonds showed poor interface qualities with only 50% clear to a eye inspection. Through repeated trials contaminants at the interface were reduced until interfaces showed over 95% clarity. The final bond process produced clear interfaces with minimal voids and bond strength enough to survive mechanical dicing after a 350°C annealing stage. No interface line was visible by eye on the diced face, showing that the two bonded samples had effectively combined into one homogeneous medium.

For dissimilar, crystalline materials, a highly resilient bonding technique was created using either hydrofluoric acid or plasma activation. Understanding of the activation procedures was gained through repeated trials, introducing the plasma cleaning stage to both activation methods and improving handling of the samples during the final, joining stages. Using a 50-hour or longer anneal at 800°C, bonds proved strong enough to survive not just ultrasonic cleaning, but harsh environmental changes, mechanical dicing and polishing too. Alternate activation methods that were trialled were also detailed, before summarising the full and final bonding processes developed during the project in clear and detailed steps for future use.

Chapter 4 applied direct bonding to the manufacturing of fibre preforms which were drawn into planar structures at fibre dimensions. Fusing and bonding were tested as methods to produce the preform, establishing direct bonding as the most reliable method for creating a void-free interface. Damage induced by dicing was avoided by facing faces to be bonded upwards, towards the blade. Several fibre structures were caned in iterative improvement trials, with each draw cleaved and inspected via microscope to look for air holes at the interface. While problems were encountered in the draw process due to twisting and handling of the cane material, these were overcome through the introduction of a guiding rod which was hung from the preform and fed directly into the cane puller. The trials demonstrated that the planar structure and aspect ratio were maintained as bonded and machined for the preforms.

A three-layer, planar structure was successfully created using fusing and caning of two custom neodymium doped phosphate glasses. While poor material characteristics (inhomogeneity, intrinsic loss, inverted core-cladding index profile) hindered the project from being progressed further, the full production method was conducted, demonstrating the potential for a small-scale large mode area fibre amplifier for higher energy/peak powers at 880 and 808 nm should suitable materials be determined.

Chapter 5 focussed on the work developing and characterising the bonding between YAG and sapphire. A resilient bond was produced through both HF and plasma-activated bonding. Initially attempts were made to produce a hydrophobic activation before it was determinined that hydrophilic route would provide a more resilient bond. Difficulties encountered such as bonds separating during annealing or dicing were overcome by testing multiple activation stages like sulphuric acid, plasma and HF to find the best treatment. HF and plasma were determined as the best routes for activation. Initially weak bonds which separated during ultrasonic cleaning were strengthened by increasing the temperature and annealing time to 800°C and 50 hours for HF-activated bonds, with an additional 50 hours for plasma activation. Both HF and plasma proved suitable for creating bonds resilient enough to survive dicing, with plasma activation producing a clearer bond interface but requiring a longer annealing process.

The resulting composites were annealed at extreme temperatures of up to 800°C, cooled to cryogenic temperatures of -184°C and survived dicing and polishing across the interface, showing remarkable resilience. An 8 mm long bonded Nd:YAG and sapphire composite was used as the gain element in a 1.064 µm laser which was pumped with over 20 W of incident power (in a ~0.45 mm cross section) and produced an output of over 7 W. The efficiency of this device was limited by a large amount of diffraction visible in the output beam (believed to be caused by clipping of the expanding pump beam on the heat sink at higher powers), as well as poor effectiveness of the anti-reflection coating and non-parallel end facets. The high doping concentration also led to front-loading of the heat profile in the composite making it less able to take advantage of the planar structure. However, the trial demonstrated the Nd:YAG/sapphire laser holds strong potential for cryogenic, high power waveguide applications, albeit requiring a number of refining steps.

In Chapter 6, the bonding process developed for ZnSe and diamond, along with ZnSe to sapphire and diamond to sapphire was demonstrated using a water-assisted, plasma-activated approach. The primary achievement of this part of the project was joining of two materials of vastly different CTEs and mechanical properties. To achieve this, multiple activation procedures were tested including heated sulphuric acid and plasma activation in an effort reduce surface contact angles and produce super hydrophilic bonding faces. Plasma was chosen as the most effective method, with diamond samples receiving an extended activation to reduce contact angles below 5°. The development of the bonded procedure was detailed, including the introduction of a water droplet to the bonding faces directly prior to contact. This method reliably developed a bond between faces which wouldn't contact spontaneously, finalising a complete bonding procedure for ZnSe and diamond.

The temperature survival range of the bonded diamond-ZnSe composite was then tested through heating and liquid nitrogen cooling. The temperature range and heating rates showed the bond was resilient to rapid changes from -40 to 80°C. The diamond-bonded composite was then tested in a localised heating trial. Using a pump-probe setup, the thermal lens induced by a focussed blue diode laser was recorded for the diamond-bonded composite and compared with bare ZnSe. The thermal lens dioptric power recorded in the bare ZnSe ($8.2\,\mathrm{m}^{-1}$) was completely eliminated in the diamond-bonded sample, clearly demonstrating the heat spreading potential of the direct bonded diamond layer.

7.2 Future work

7.2.1 Direct bonding for planar fibre preforms

The work reported in this thesis demonstrated the capability to produce a planar-structured, fibre-scale device for use in active laser devices. However, material constraints and deficiencies restricted development at the final stages. Despite two attempts at production, the phosphate glass produced for the project did not meet the requirements to progress due to inhomogeneity of the glass, clumping of the neodymium dopant and incorrect index profiles causing loss or impeding the waveguide design.

To advance the planar waveguide production, improving the glass homogeneity is essential for both cladding and core to allow for pump and laser guiding, reducing intrinsic losses in the glass can also be complimented through a higher doping concentration. Due to the planar design guiding only in one axis, short devices are required to keep the device within the Rayleigh range and minimise clipping of the pump beam towards each end of the device. Therefore, a higher doping concentration is required. Increasing the neodymium quantity requires homogeneity to be improved to stop the bulkier neodymium from clumping within the glass as observed in this project.

The index profiles of the core and cladding also need suitable refractive indices to support total internal reflection, with closely matched values (as specified during this project) to inhibit higher order laser mode guidance. The glass would therefore need a thorough characterisation, ensuring it meets the standards required by an end device both before and after the fibre draw. Finally, the curvature noted in the draw was believed to be due to the temperature gradient in the tower susceptor. A larger susceptor could provide a more even heat profile, reducing the effect. This could also allow for a greater aspect ratio, reducing the risk of clipping of the pump beam and allowing for better heat extraction through the thin axis.

With these problems accounted for, a proposed next step would be producing a three-layer preform via direct bonding, conducting each bonding stage separately using a low temperature anneal. Repolishing of the second bonding face may be required after annealing the first bond. The three layer preform could then be drawn as demonstrated in the phosphate glass draws, producing large quantities of material to be cleaved into short segments. For an end device, coating to reduce risk of damage to the outer face is desired, however this would require adapting the fibre caning process or developing a coating procedure post-draw. Following end facet polishing the short devices could then be tested when built into an amplifier setup for a diode bar with cladding pumping, as well as constructing an oscillator around the bonded, caned and cleaved segments.

7.2.2 Nd:YAG to sapphire bonding for active devices

Some clear steps are available to further the Nd:YAG to sapphire bonding investigation. While a bond of remarkable resilience was developed, the efficiency of the 1.064 µm laser oscillator was lower than believed to be possible due to a number of reasons. These included the diffraction visible in the output beam, poor AR coating and choice of doping concentration. If the project were to be continued, the first step would be to acquire YAG doped with a lower concentration of neodymium. To truly take advantage of the heat-spreading benefits of the sapphire layer and planar structure, a longer device of lower doping concentration should be produced. This would create a more even heat profile across the length, instead of front-loading the absorption of the pump - and therefore the heat load as well - within the crystal.

A three layer composite is also suggested as a logical progression. With sapphire bonded to both sides of the gain medium, heat can be extracted uniformly across the thin dimension of the device, face cooling both sides to truly take advantage of the planar structure. This would require bonding and annealing of one side before re-polishing the alternate face to be bonded using the same process. Following this, greater care must be taken in polishing the final composite's end facets as the significant curvature noted on the end faces was believed contribute to the large power noted outside of the central beam. Faces to be polished should be packed in with like materials (sapphire with sapphire etc.) to minimise rounding at the edges as material is worn away. Only once faces are confirmed to be flat should an AR coating be applied. With these steps conducted, the 1.064 µm laser trial could be repeated and compared to the initial test in efficiency. Following this, a 9XX amplifier setup could be designed as an alternate trial. Finally, a cryogenic temperature trial could be conducted to observe how the laser operation improves with sapphire's increase in thermal conductivity. The real advantage of the Yag-sapphire bond would be in the production of high power laser oscillators at cryogenic temperatures

From the perspective of bonding, an assessment regarding the yield of each bonding technique and routes by which to increase this (larger area bonding) are suggested, along with a qualitative assessment for the strength of bonds using a tensile or shear test method. Ideally, a flexure strength test could be conducted as described in Section 2.2.4, however this would require many samples to be produced and bonded for the sole purpose of strength testing. Comparison should be made between HF and plasma activated bonds as well recording strength with increasing annealing times to determine the optimal activation and annealing processes to maximise bond strength.

7.2.3 Direct bonding zinc selenide to diamond

The zinc selenide to diamond bond was conducted as a hydrophilic process, with the addition of a water droplet to the interface. While it is believed that water evaporates from the bond over time, it has not yet been tested if a layer of water remains at this interface. Zinc selenide is typically used as a host medium in active devices operating in the mid-IR range. Due to water's absorption spectrum in this band, it is suggested that the absorption of a ZnSe piece bonded using the technique developed here should be characterised.

Following this, chromium or iron doped ZnSe should be acquired to test if bonding works similarly to materials for an active device. To test the new material, the same trial as conducted with the blue diode could be tested once more with absorption more representative of an active device. Finally, could pieces of diamond and ZnSe be acquired of the exact required dimensions, a planar waveguide device could be built, bonding a two or three layer structure for trialling. The dimension would need to be well defined and then precisely aligned during bonding as the inability to undergo high temperature annealing to increase strength precludes mechanical polishing or similar processing following the bonding stage. Given an additional sapphire layer, a thin disk design could also be built. For that reason, ZnSe to sapphire bonding, which was briefly tested in this project, should be trialled further. The two materials have much closer thermal expansion coefficients so the temperature survivability range should be thoroughly investigated once more.

Due to diamond's absorption in the infra red, bonding with an intermediate layer is of interest for the ZnSe-diamond combination. As such a bond conducted with a thin, sapphire or dielectric layer should be tested. An end device could be envisaged of a thin disk layer using doped ZnSe bonded to diamond via a thin intermediate layer of sapphire. In addition, bonding of different surface areas and sample thickness should be trialled, including diamond wafers where the low thickness could help alleviate the poor surface quality's impact on bonding strength.

Finally, as with the YAG-sapphire bonds assessment of the yield for bonding processes, along with a qualitative assessment of the strength of bonds produced should be conducted. A comparison should be conducted between room temperature and 80°C annealed bonds to see if the strength of the bond can be increased through heating even at low temperatures.

References

[1] Q-Y. Tong, G. Cha, R. Gafiteanu, and U. Gosele. Low temperature wafer direct bonding. *Journal of microelectromechanical systems*, 3(1):29–35, 1994. ISSN 1057-7157.

[2] W. P. Maszara. Silicon-on-insulator by wafer bonding: A review. *Journal of the Electrochemical Society*, 138(1):341–347, 1991.

[3] C. T. A. Brown, C. L. Bonner, T. J. Warburton, D. P. Shepherd, A. C. Tropper, D. C. Hanna, and H. E. Meissner. Thermally bonded planar waveguide lasers. *Applied Physics Letters*, 71(9):1139–1141, 1997. doi: doi:http://dx.doi.org/10.1063/1.119846. URL `http://scitation.aip.org/content/aip/journal/apl/71/9/10.1063/1.119846`.

[4] D. P. Shepherd, C. L. Bonner, C. T. A. Brown, W. A. Clarkson, A. C. Tropper, D. C. Hanna, and H. E. Meissner. High-numerical-aperture, contact-bonded, planar waveguides for diode-bar-pumped lasers. *Optics Communications*, 160(13):47–50, 1999. ISSN 0030-4018. doi: http://dx.doi.org/10.1016/S0030-4018(98)00653-1. URL `http://www.sciencedirect.com/science/article/pii/S0030401898006531`.

[5] H. Ichikawa, K. Yamaguchi, T. Katsumata, and I. Shoji. High-power and highly efficient composite laser with an anti-reflection coated layer between a laser crystal and a diamond heat spreader fabricated by room-temperature bonding. *Optics Express*, 25(19):22797–22804, 2017. doi: 10.1364/OE.25.022797. URL `http://www.opticsexpress.org/abstract.cfm?URI=oe-25-19-22797`.

[6] K. Hara, K. Takayanagi, S. Matsumoto, M. Nakajima, and I. Shoji. Fabrication of a new walk-off compensating BBO periodic structure by use of the room-temperature-bonding technique. In *Nonlinear Optics*, OSA Technical Digest (CD), page NMA5. Optical Society of America. doi: 10.1364/NLO.2011.NMA5.

[7] R. Hooke. *Micrographia*, volume 1. Allestry, The Royal Society, 1665.

[8] G. B. Airy. Vi. on the phnomena of Newton's rings when formed between two transparent substances of different refractive powers. *Philosophical Magazine*, 2

(7):20–30, 1833. ISSN 1941-5966. doi: 10.1080/14786443308647959. URL http://dx.doi.org/10.1080/14786443308647959.

[9] R. Eisenschitz and F. London. Uber das Verhaltnis der van der waalsschen krafte zu den homoopolaren Bindungskraften. *Zeitschrift fur Physik*, 60(7):491–527, 1930. ISSN 0044-3328. doi: 10.1007/bf01341258. URL https://doi.org/10.1007/BF01341258.

[10] H. C. Hamaker. The London van der waals attraction between spherical particles. *Physica*, 4(10):1058–1072, 1937. ISSN 0031-8914. doi: http://dx.doi.org/10.1016/S0031-8914(37)80203-7. URL http://www.sciencedirect.com/science/article/pii/S0031891437802037.

[11] D. Dowson. *History of tribology.* Longman, London ; New York, 1979. ISBN 0582447664.

[12] Lord Rayleigh. A study of glass surfaces in optical contact. *Proceedings of the Royal Society of London. Series A - Mathematical and Physical Sciences*, 156(888):326–349, 1936. doi: 10.1098/rspa.1936.0151. URL http://rspa.royalsocietypublishing.org/content/royprsa/156/888/326.full.pdf.

[13] G. Wallis and D. I. Pomerantz. Field assisted glass metal sealing. *Journal of Applied Physics*, 40(10):3946–3949, 1969. doi: 10.1063/1.1657121. URL http://aip.scitation.org/doi/abs/10.1063/1.1657121.

[14] M. Shimbo, K. Furukawa, K. Fukuda, and K. Tanzawa. Silicon to silicon direct bonding method. *Journal of Applied Physics*, 60(8):2987–2989, 1986. doi: 10.1063/1.337750. URL http://aip.scitation.org/doi/abs/10.1063/1.337750http://aip.scitation.org/doi/pdf/10.1063/1.337750.

[15] E. Yablonovitch, D. M. Hwang, T. J. Gmitter, L. T. Florez, and J. P. Harbison. Van der waals bonding of GaAs epitaxial liftoff films onto arbitrary substrates. *Applied Physics Letters*, 56(24):2419–2421, 1990. ISSN 0003-6951. doi: 10.1063/1.102896. URL http://aip.scitation.org/doi/10.1063/1.102896.

[16] U. Gosele and Q. Y. Tong. Semiconductor wafer bonding. *Annual Review of Materials Science*, 28:215–241, 1998. ISSN 0084-6600. doi: 10.1146/annurev.matsci.28.1.215. URL http://www.annualreviews.org/doi/abs/10.1146/annurev.matsci.28.1.215.

[17] J. Haisma, B. A. C. M. Spierings, U. K. P. Biermann, and A. A. Vangorkum. Diversity and feasibility of direct bonding - a survey of a dedicated optical-technology. *Applied Optics*, 33(7):1154–1169, 1994. ISSN 0003-6935.

[18] J. Haisma. Direct bonding: retrospect and outlook. *Philips Journal of Research*, 49(12):171–177, 1995. ISSN 0165-5817. doi: http://dx.doi.org/10.

1016/0165-5817(95)82010-8. URL http://www.sciencedirect.com/science/article/pii/0165581795820108.

[19] Jan Haisma and G. A. C. M. Spierings. Contact bonding, including direct-bonding in a historical and recent context of materials science and technology, physics and chemistry: Historical review in a broader scope and comparative outlook. *Materials Science and Engineering: R: Reports*, 37(12):1–60, 2002. ISSN 0927-796X. doi: http://dx.doi.org/10.1016/S0927-796X(02)00003-7. URL http://www.sciencedirect.com/science/article/pii/S0927796X02000037.

[20] J. Haisma, N. Hattu, J. T. C. M. Pulles, E. Steding, and Jan C. G. Vervest. Direct bonding and beyond. *Applied Optics*, 46(27):6793–6803, 2007. ISSN 1559-128X; 2155-3165. doi: 10.1364/ao.46.006793. URL http://www.opticsinfobase.org/DirectPDFAccess/F42A54C3-963C-360E-8C8A3742D496874F_141849/ao-46-27-6793.pdf?da=1&id=141849&seq=0&mobile=no.

[21] J. Haisma, J. J. C. Groenen, and P. W. de Haas. Non-silicon applications of direct bonding. *Philips Journal of Research*, 49(12):151–163, 1995. ISSN 0165-5817. doi: http://dx.doi.org/10.1016/0165-5817(95)82008-6. URL http://www.sciencedirect.com/science/article/pii/0165581795820086.

[22] P. H. Chiang and J. M. Song. Influence of pretreatment on copper direct bonding. In *2016 International Conference on Electronics Packaging (ICEP)*, pages 489–492. doi: 10.1109/ICEP.2016.7486875. URL http://ieeexplore.ieee.org/ielx7/7481053/7486763/07486875.pdf?tp=&arnumber=7486875&isnumber=7486763.

[23] Akira Sugiyama and Yasunaga Nara. Improved direct bonding method of Nd:YVO4 and YVO4 laser crystals. *Ceramics International*, 31(8):1085–1090, 2005. ISSN 0272-8842. doi: http://dx.doi.org/10.1016/j.ceramint.2004.11.009. URL http://www.sciencedirect.com/science/article/pii/S0272884204005073.

[24] H. Takagi, R. Maeda, T. R. Chung, N. Hosoda, and T. Suga. Effect of surface roughness on room-temperature wafer bonding by Ar beam surface activation. *Japanese Journal of Applied Physics*, 37(7R):4197, 1998. ISSN 1347-4065. URL http://stacks.iop.org/1347-4065/37/i=7R/a=4197.

[25] T. Suga, T. Matsumae, Y. Matsumoto, and M. Nakano. Direct bonding of polymer to glass wafers using surface activated bonding method at room temperature. *2012 3rd IEEE International Workshop on Low Temperature Bonding for 3D Integration*, pages 161–161, 2012. doi: 10.1109/ltb-3d.2012.6238098. URL http://ieeexplore.ieee.org/ielx5/6231711/6238032/06238098.pdf?tp=&arnumber=6238098&isnumber=6238032.

[26] K. Takeuchi, M. Fujino, and T. Suga. Direct bonding and debonding of glass wafers for handling of ultra-thin glass sheets. In *2016 International Conference on Electronics Packaging (ICEP)*, pages 298–301. doi: 10.1109/ICEP.2016.7486833. URL `http://ieeexplore.ieee.org/ielx7/7481053/7486763/07486833.pdf?tp=&arnumber=7486833&isnumber=7486763`.

[27] K. Imura, M. Kawaji, T. Yaguchi, and I. Shoji. New fabrication technique of quasi-phase-matched devices by use of the room-temperature-bonding. In *Advances in Optical Sciences Congress*, OSA Technical Digest (CD), page JWA14. Optical Society of America. doi: 10.1364/NLO.2009.JWA14.

[28] L. Zheng, A. Kausas, and T. Taira. Drastic thermal effects reduction through distributed face cooling in a high power giant-pulse tiny laser. *Optical Materials Express*, 7(9):3214–3221, 2017. doi: 10.1364/OME.7.003214. URL `https://www.osapublishing.org/ome/abstract.cfm?uri=ome-7-9-3214`.

[29] D. Pasquariello, M. Lindeberg, C. Hedlund, and K. Hjort. Surface energy as a function of self-bias voltage in oxygen plasma wafer bonding. *Sensors and Actuators A: Physical*, 82(13):239–244, 2000. ISSN 0924-4247. doi: http://dx.doi.org/10.1016/S0924-4247(99)00338-6. URL `http://www.sciencedirect.com/science/article/pii/S0924424799003386`.

[30] C. Rothhardt, J. Rothhardt, A. Klenke, T. Peschel, R. Eberhardt, J. Limpert, and A. Tunnermann. BBO-sapphire sandwich structure for frequency conversion of high power lasers. *Optical Materials Express*, 4(5):1092–1103, 2014. doi: 10.1364/OME.4.001092. URL `http://www.opticsinfobase.org/ome/abstract.cfm?URI=ome-4-5-1092`.

[31] D-L. Li, Z-G. Shang, S. Q. Wang, and Z-Y. Wen. Low temperature Si/Si wafer direct bonding using a plasma activated method. *Journal of Zhejiang University, SCIENCE C (Computers & Electronics)*, 14(4):244–251, 2013. ISSN 1869-1951. doi: 10.1631/jzus.C12MNT02. URL `https://link.springer.com/article/10.1631/jzus.C12MNT02`.

[32] U. I. Can and B. Bayram. Plasma-activated direct bonding of patterned silicon-on-insulator wafers to diamond-coated wafers under vacuum. *Diamond and Related Materials*, 47:53–57, 2014. ISSN 0925-9635. doi: 10.1016/j.diamond.2014.06.002. URL `http://www.sciencedirect.com/science/article/pii/S0925963514001204`.

[33] C. Wang, Y. Wang, Y. Tian, C. Wang, and T. Suga. Room-temperature direct bonding of silicon and quartz glass wafers. *Applied Physics Letters*, 110(22):221602, 2017. doi: 10.1063/1.4985130. URL `http://aip.scitation.org/doi/abs/10.1063/1.4985130`.

[34] C. Rothhardt, M. Rekas, G. Kalkowski, R. Eberhardt, and A. Tunnermann. New approach to fabrication of a Faraday isolator for high power laser applications. *Fiber Lasers IX: Technology, Systems, and Applications*, 8237, 2012. ISSN 0277-786X. doi: 10.1117/12.908550. URL `http://proceedings.spiedigitallibrary.org/proceeding.aspx?articleid=1277388`.

[35] J. Fan, G. Y. Chong, and C. S. Tan. Study of hydrophilic si direct bonding with ultraviolet ozone activation for 3D integration. *ECS Journal of Solid State Science and Technology*, 1(6):P291–P296, 2012. ISSN 2162-8769. doi: 10.1149/2.026206jss. URL `http://jss.ecsdl.org/content/1/6/P291.full.pdf`.

[36] J. R. Vig and J. LeBus. UV/Ozone cleaning of surfaces. *Parts, Hybrids, and Packaging, IEEE Transactions on*, 12(4):365–370, 1976. ISSN 0361-1000. doi: 10.1109/TPHP.1976.1135156. URL `http://ieeexplore.ieee.org/ielx6/8217/25231/01135156.pdf?tp=&arnumber=1135156&isnumber=25231`.

[37] C. S. Tan, A. Fan, K. N. Chen, and R. Reif. Low-temperature thermal oxide to plasma-enhanced chemical vapor deposition oxide wafer bonding for thin-film transfer application. *Applied Physics Letters*, 82(16):2649–2651, 2003. ISSN 0003-6951. doi: 10.1063/1.1569657. URL `http://aip.scitation.org/doi/abs/10.1063/1.1569657`.

[38] K. Ljungberg, A. Soderbarg, S. Bengtsson, and A. Jauhiainen. Characterization of spontaneously bonded hydrophobic silicon surfaces. *Journal of the Electrochemical Society*, 141(2):562–566, 1994. ISSN 0013-4651. doi: 10.1149/1.2054767. URL `http://jes.ecsdl.org/content/141/2/562.short`.

[39] G. A. C. M. Spierings, J. Haisma, and T. M. Michelsen. Surface-related phenomena in the direct bonding of silicon and fused-silica wafer pairs. *Philips Journal of Research*, 49(12):47–63, 1995. ISSN 0165-5817. doi: http://dx.doi.org/10.1016/0165-5817(95)82003-5. URL `http://www.sciencedirect.com/science/article/pii/0165581795820035`.

[40] C. B. E. Gawith, A. Fu, T. Bhutta, P. Hua, D. P. Shepherd, E. R. Taylor, P. G. R. Smith, D. Milanese, and M. Ferraris. Direct-uv-written buried channel waveguide lasers in direct-bonded intersubstrate ion-exchanged neodymium-doped germano-borosilicate glass. *Applied Physics Letters*, 81(19):3522–3524, 2002. doi: http://dx.doi.org/10.1063/1.1519103. URL `http://aip.scitation.org/doi/10.1063/1.1519103`.

[41] I. Mukhin, E. Perevezentsev, and O. Palashov. Fabrication of composite laser elements by a new thermal diffusion bonding method. *Optical Materials Express*, 4(2):266–271, 2014. ISSN 2159-3930. doi: 10.1364/ome.4.000266. URL `https://www.osapublishing.org/ome/abstract.cfm?URI=ome-4-2-266`.

[42] D. H. Gwo. *Ultra-precision bonding for cryogenic fused-silica optics*, volume 3435 of *Proceedings of the Society of Photo-Optical Instrumentation Engineers (Spie)*, pages 136–142. Spie-Int Soc Optical Engineering, Bellingham, 1998. ISBN 0277-786X 0-8194-2890-6. doi: 10.1117/12.323731. URL http://proceedings.spiedigitallibrary.org/data/Conferences/SPIEP/45398/136_1.pdf.

[43] N. L. Beveridge, A. A. van Veggel, L. Cunningham, J. Hough, I. W. Martin, R. Nawrodt, S. Reid, and S. Rowan. Dependence of cryogenic strength of hydroxide catalysis bonded silicon on type of surface oxide. *Classical and Quantum Gravity*, 30(2):025003, 2013. ISSN 0264-9381. URL http://stacks.iop.org/0264-9381/30/i=2/a=025003.

[44] R. Douglas, A. A. van Veggel, L. Cunningham, K. Haughian, J. Hough, and S. Rowan. Cryogenic and room temperature strength of sapphire jointed by hydroxide-catalysis bonding. *Classical and Quantum Gravity*, 31(4):045001, 2014. ISSN 0264-9381. URL http://stacks.iop.org/0264-9381/31/i=4/a=045001.

[45] S. Sinha, K. E. Urbanek, A. Krzywicki, and R. L. Byer. Investigation of the suitability of silicate bonding for facet termination in active fiber devices. *Optics Express*, 15(20):13003–13022, 2007. doi: 10.1364/OE.15.013003. URL http://www.opticsexpress.org/abstract.cfm?URI=oe-15-20-13003.

[46] P. Bastock. Gallium lanthunum sulphide differential thermal analysis, Optoelectronics Research Centre, University of Southampton, 2014.

[47] Q. Y. Tong and U. Gosele. *Semiconductor Wafer Bonding: Science and Technology*, volume 1. John Wiley & Sons, Incorporated, 1999. ISBN 0471574813.

[48] W. H. Keesom. The second virial coefficient for rigid spherical molecules, whose mutual attraction is equivalent to that of a quadruplet placed at their centre. *Koninklijke Nederlandse Akademie van Wetenschappen Proceedings Series B Physical Sciences*, 18:636–646, 1915. URL http://www.dwc.knaw.nl/DL/publications/PU00012540.pdf.

[49] V. A. Parsegian. *Van Der Waals Forces: A Handbook for Biologists, Chemists, Engineers, and Physicists.* Cambridge University Press, New York, 2006. ISBN 0-521-54778-4.

[50] C. C. Da-Roz A. L. Leite, F. L. Bueno and O. N. Ziemath, E. C. Oliveira. Theoretical models for surface forces and adhesion and their measurement using atomic force microscopy. *International Journal of Molecular Sciences*, 13(10), 2012.

[51] J. Israelachvili. *Intermolecular & Surface Forces.* Academic Press, second edition, 1991. ISBN 0-12-375181-0.

[52] Y. A. Gu. Experimental determination of the Hamaker constants for solid-water-oil systems. *Journal of Adhesion Science and Technology*, 15(11):1263–1283, 2001.

[53] L. Bergstrom. Hamaker constants of inorganic materials. *Advances in Colloid and Interface Science*, 70:125–169, 1997. ISSN 0001-8686. doi: 10.1016/s0001-8686(97)00003-1. URL `http://www.sciencedirect.com/science/article/pii/S0001868697000031`.

[54] H. Lee, H. E. Meissner, and O. R. Meissner. Adhesive-free-bond (AFB) CVD diamond/sapphire and CVD diamond/YAG crystal composites. *SPIE Proceedings: Laser Source and System Technology for Defense and Security II*, 6216, 2006.

[55] K. Song and D. Le. Bond energies - average bond energy, 2015. URL `http://chemwiki.ucdavis.edu/Theoretical_Chemistry/Chemical_Bonding/General_Principles/Bond_Energies`. Accessed: 15-07-2017.

[56] A. Sugiyama, H. Fukuyama, T. Sasuga, T. Arisawa, and H. Takuma. Direct bonding of Ti : sapphire laser crystals. *Applied Optics*, 37(12):2407–2410, 1998. ISSN 0003-6935. doi: 10.1364/ao.37.002407. URL `https://www.osapublishing.org/ao/abstract.cfm?uri=ao-37-12-2407`.

[57] G. Kalkowski, C. Rothhardt, P. J. Jobst, M. Schurmann, and R. Eberhardt. Glass direct bonding for optical applications. *ECS Transaction*, 50(7):399–405, 2012. doi: 10.1149/05007.0399ecst. URL `http://ecst.ecsdl.org/content/50/7/399`.

[58] H. Shinohara, Y. Takahashi, J. Mizuno, and S. Shoji. Surface hydrophilic treatment of polyurea film realized by vacuum ultraviolet light irradiation and its application for poly(methylmethacrylate) blood analysis chip. *Sensors and Actuators B: Chemical*, 132(2):374–379, 2008. ISSN 0925-4005. doi: http://dx.doi.org/10.1016/j.snb.2007.09.072. URL `http://www.sciencedirect.com/science/article/pii/S0925400507007939`.

[59] A. Hozumi, H. Inagaki, and T. Kameyama. The hydrophilization of polystyrene substrates by 172-nm vacuum ultraviolet light. *Journal of Colloid and Interface Science*, 278(2):383–392, 2004. ISSN 0021-9797. doi: http://dx.doi.org/10.1016/j.jcis.2004.06.005. URL `http://www.sciencedirect.com/science/article/pii/S0021979704005144`.

[60] G. Kalkowski, M. Rohde, S. Risse, R. Eberhardt, and A. Tunnermann. *Direct Bonding of Glass Substrates*, volume 33 of *ECS Transactions*, pages 349–355. 2010. ISBN 1938-5862 978-1-60768-173-1. doi: 10.1149/1.3483524. URL `http://ecst.ecsdl.org/content/33/4/349`.

[61] Y. Xu, C. Wang, Y. Dong, L. Li, K. Jang, K. Mawatari, T. Suga, and T. Kitamori. Low-temperature direct bonding of glass nanofluidic chips using a two-step plasma surface activation process. *Analytical and Bioanalytical Chemistry*, 402(3):1011–1018, 2012. ISSN 1618-2642. doi: 10.1007/s00216-011-5574-2. URL `https://link.springer.com/article/10.1007%2Fs00216-011-5574-2`.

[62] A. U. Alam, M. M. R. Howlader, and M. J. Deen. Oxygen Plasma and humidity dependent surface analysis of silicon, silicon dioxide and glass for direct wafer bonding. *Ecs Journal of Solid State Science and Technology*, 2(12):P515–P523, 2013. ISSN 2162-8769. doi: 10.1149/2.007312jss. URL `http://jss.ecsdl.org/content/2/12/P515.full.pdf`.

[63] Y. Kurashima, A. Maeda, and H. Takagi. Characterization of bonding interface prepared by room-temperature Si wafer direct bonding using the surface smoothing effect of a Ne fast atom beam. *Microelectronic Engineering*, 118(0):1–5, 2014. ISSN 0167-9317. doi: http://dx.doi.org/10.1016/j.mee.2014.01.005. URL `http://www.sciencedirect.com/science/article/pii/S0167931714000070`.

[64] S. H. Christiansen, R. Singh, and Ulrich Gosele. Wafer direct bonding: From advanced substrate engineering to future applications in micro/nanoelectronics. *Proceedings of the IEEE*, 94(12):2060–2106, 2006. ISSN 0018-9219. doi: 10.1109/JPROC.2006.886026.

[65] G Kalkowski, S Risse, C Rothhardt, M Rohde, and R Eberhardt. Optical contacting of low-expansion materials. In *SPIE Optical Engineering+ Applications*, pages 81261F–81261F–7. International Society for Optics and Photonics.

[66] S. Wasserman, M. Snir, H. Dodiuk, and S. Kenig. Transmission and mechanical properties of optical adhesives. *The Journal of Adhesion*, 27(2):67–81, 1989. ISSN 0021-8464. doi: 10.1080/00218468908050594. URL `http://dx.doi.org/10.1080/00218468908050594`.

[67] J. M. Bennett and L. Mattsson. *Introduction to Surface Roughness and Scattering*. Optical Society of America, Washington, D.C., 1989. ISBN 1-55752-609-5.

[68] B. Ma, H. Kuwae, A. Okada, W. Fu, S. Shoji, and J. Mizuno. Low temperature direct bonding of single crystal quartz substrates for high performance optical low pass filter using amorphous SiO2 intermediate layers. In *2016 IEEE 29th International Conference on Micro Electro Mechanical Systems (MEMS)*, pages 25–28. doi: 10.1109/MEMSYS.2016.7421548.

[69] A. N. Korsgaard and T. Rafael. Drop shape analysis for determination of dynamic contact angles by double sided elliptical fitting method. *Measurement Science and Technology*, 28(4):047003, 2017. ISSN 0957-0233. URL `http://stacks.iop.org/0957-0233/28/i=4/a=047003`.

[70] M. E. Karaman, D. A. Antelmi, and R. M. Pashley. The production of stable hydrophobic surfaces by the adsorption of hydrocarbon and fluorocarbon carboxylic acids onto alumina substrates. *Colloids and Surfaces A: Physicochemical and Engineering Aspects*, 182(13):285–298, 2001. ISSN 0927-7757. doi: http://dx.doi.org/10.1016/S0927-7757(00)00821-9. URL `http://www.sciencedirect.com/science/article/pii/S0927775700008219`.

[71] D. Megias-Alguacil, E. Tervoort, C. Cattin, and L. J. Gauckler. Contact angle and adsorption behavior of carboxylic acids on -Al2O3 surfaces. *Journal of Colloid and Interface Science*, 353(2):512–518, 2011. doi: 10.1016/j.jcis.2010.09.087. URL http://www.sciencedirect.com/science/article/pii/S0021979710011604.

[72] M. Sozzi, A. Rahman, and S. Pissadakis. Demonstration of negative refractive index photosensitivity mechanism in a phosphate glass optical fibre using 248nm, 500fs laser radiation. In *CLEO/Europe and EQEC 2011 Conference Digest*, OSA Technical Digest (CD). Optical Society of America. URL http://www.opticsinfobase.org/abstract.cfm?URI=CLEO_Europe-2011-CM3_1.

[73] K. Kalli, C. Riziotis, A. Posporis, C. Markos, C. Koutsides, S. Ambran, A. S. Webb, C. Holmes, J. C. Gates, J. K. Sahu, and P. G. R. Smith. Flat fibre and femtosecond laser technology as a novel photonic integration platform for optofluidic based biosensing devices and lab-on-chip applications: Current results and future perspectives. *Sensors and Actuators B: Chemical*, 209(0):1030–1040, 2015. ISSN 0925-4005. doi: http://dx.doi.org/10.1016/j.snb.2014.12.003. URL http://www.sciencedirect.com/science/article/pii/S0925400514015457.

[74] A. N. Abramov, M. V. Yashkov, A. N. Guryanov, M. A. Melkumov, D. A. Dvoretskii, I. A. Bufetov, L. D. Iskhakova, V. V. Koltashev, M. N. Kachenyuk, and M. F. Torsunov. Fabrication and optical characterization of silica fibers with a chromium- and alumina-doped core. *Inorganic Materials*, 50(12):1283–1288, 2014. ISSN 0020-1685. doi: 10.1134/s0020168514110016. URL https://link.springer.com/article/10.1134/S0020168514110016.

[75] C. Brunet, P. Vaity, Y. Messaddeq, S. LaRochelle, and L. A. Rusch. Design, fabrication and validation of an OAM fiber supporting 36 states. *Optics Express*, 22(21):26117–26127, 2014. ISSN 1094-4087. doi: 10.1364/oe.22.026117. URL https://www.osapublishing.org/oe/abstract.cfm?uri=oe-22-21-26117.

[76] K. P. W. Dissanayake, H. A. Abdul-Rashid, A. Safaei, A. Oresegun, N. Shahrizan, N. Y. M. Omar, Z. Yusoff, M. I. Zulkifli, S. Z. Muhamad-Yassin, K. A. Mat-Sharif, and N. Tamchek. Fabrication and characterization of a gallium co-doped erbium optical fiber. *2014 IEEE 5th International Conference on Photonics (ICP). Proceedings*, pages 113–115, 2014. doi: 10.1109/icp.2014.7002327. URL http://ieeexplore.ieee.org/document/7002327/.

[77] J. R. Marciante, V. V. Shkunov, and D. A. Rockwell. Semi-guiding high-aspect-ratio core (SHARC) fiber amplifiers with ultra-large core area for single-mode kW operation in a compact coilable package. *Optics Express*, 20(18):20238–20254, 2012. ISSN 1094-4087.

[78] J-H. Jean and T. K. Gupta. Crystallization kinetics of binary borosilicate glass composite. *Journal of Materials Research*, 7(11):

3103–3111, 1992. ISSN 0884-2914. URL https://www.cambridge.org/core/journals/journal-of-materials-research/article/crystallization-kinetics-of-binary-borosilicate-glass-composite/16FD8DB9DB5082611F21F3EAE0998E1E.

[79] A. A. S. Lopes, R. C. C. Monteiro, R. S. Soares, M. M. R. A. Lima, and M. H. V. Fernandes. Crystallization kinetics of a bariumzinc borosilicate glass by a non-isothermal method. *Journal of Alloys and Compounds*, 591(0):268–274, 2014. ISSN 0925-8388. doi: http://dx.doi.org/10.1016/j.jallcom.2013.12.086. URL http://www.sciencedirect.com/science/article/pii/S092583881303065X.

[80] J.D. Ingle and S.R. Crouch. *Spectrochemical Analysis*. Prentice Hall, 1988. ISBN 9780138268763. URL https://books.google.co.uk/books?id=1NHvAAAAMAAJ.

[81] T. Kubota, H. Atarashi, and I. Shoji. Fabrication of quasi-phase-matching stacks of GaAs plates using a new technique: room-temperature bonding. *Optical Materials Express*, 7(3):932–938, 2017. doi: 10.1364/OME.7.000932. URL https://www.osapublishing.org/ome/abstract.cfm?URI=ome-7-3-932.

[82] S. Tokita, J. Kawanaka, M. Fujita, T. Kawashima, and Y. Izawa. Sapphire-conductive end-cooling of high power cryogenic Yb:YAG lasers. *Applied Physics B*, 80(6):635–638, 2005. ISSN 1432-0649. doi: 10.1007/s00340-005-1779-4. URL https://doi.org/10.1007/s00340-005-1779-4.

[83] E. Worner, C. Wild, W. Muller-Sebert, R. Locher, and P. Koidl. Thermal conductivity of CVD diamond films: high-precision, temperature-resolved measurements. *Diamond and Related Materials*, 5(6):688–692, 1996. ISSN 0925-9635. doi: http://dx.doi.org/10.1016/0925-9635(95)00390-8. URL http://www.sciencedirect.com/science/article/pii/0925963595003908.

[84] J. Didierjean, M. Castaing, F. Balembois, P. Georges, D. Perrodin, J. M. Fourmigu, K. Lebbou, A. Brenier, and O. Tillement. High-power laser with Nd:YAG single-crystal fiber grown by the micro-pulling-down technique. *Optics Letters*, 31(23):3468–3470, 2006. doi: 10.1364/OL.31.003468. URL http://ol.osa.org/abstract.cfm?URI=ol-31-23-3468.

[85] S. P. Ng and J. I. Mackenzie. Power and radiance scaling of a 946 nm Nd:YAG planar waveguide laser. *Laser Physics*, 22(3):494–498, 2012. ISSN 1054-660X. doi: 10.1134/s1054660x12030140. URL https://link.springer.com/content/pdf/10.1134%2FS1054660X12030140.pdf.

[86] D. Meschede. *Optics, Light, and Lasers: The Practical Approach to Modern Aspects of Photonics and Laser Physics*. Wiley-VCH Verlag GmbH & Co. KGaA, 2017. ISBN 9783527685486. doi: 10.1002/9783527685486.ch2. URL http://dx.doi.org/10.1002/9783527685486.ch2.

[87] P. A. Belanger. Beam propagation and the ABCD ray matrices. *Optics Letters*, 16(4):196–198, 1991. ISSN 0146-9592. doi: 10.1364/ol.16.000196. URL `https://www.osapublishing.org/ol/abstract.cfm?uri=ol-16-4-196`.

[88] V. G. Savitski, S. Reilly, and A. J. Kemp. Steady-state Raman gain in diamond as a function of pump wavelength. *IEEE Journal of Quantum Electronics*, 49(2): 218–223, 2013. ISSN 0018-9197. doi: 10.1109/JQE.2012.2237505.

[89] R. P. Mildren and A. Sabella. Highly efficient diamond Raman laser. *Optics Letters*, 34(18):2811–2813, 2009. doi: 10.1364/OL.34.002811. URL `https://www.osapublishing.org/ol/abstract.cfm?uri=ol-34-18-2811`.

[90] I. T. Sorokina. Cr2+-doped IIVI materials for lasers and nonlinear optics. *Optical Materials*, 26(4):395–412, 2004. ISSN 0925-3467. doi: http://dx.doi.org/10.1016/j.optmat.2003.12.025. URL `http://www.sciencedirect.com/science/article/pii/S0925346704000771`.

[91] J. R. Macdonald, S. J. Beecher, P. A. Berry, G. Brown, K. L. Schepler, and A. K. Kar. Efficient mid-infrared Cr:ZnSe channel waveguide laser operating at 2486nm. *Optics Letters*, 38(13):2194–2196, 2013. doi: 10.1364/OL.38.002194. URL `https://www.osapublishing.org/ol/abstract.cfm?URI=ol-38-13-2194`.

[92] I. Moskalev, S. Mirov, M. Mirov, S. Vasilyev, V. Smolski, A. Zakrevskiy, and V. Gapontsev. 140 W Cr:ZnSe laser system. *Optics Express*, 24(18):21090–21104, 2016. doi: 10.1364/OE.24.021090. URL `https://www.osapublishing.org/oe/abstract.cfm?uri=oe-24-18-21090`.

[93] A. M. Zaitsev. *Optical Properties of Diamond: A Data Handbook*, volume 1. Springer-Verlag, 2001. doi: https://doi.org/10.1007/978-3-662-04548-0.

[94] D. T. F. Marple. Refractive index of ZnSe, ZnTe, and CdTe. *Journal of Applied Physics*, 35(3):539–542, 1964. doi: 10.1063/1.1713411. URL `http://aip.scitation.org/doi/abs/10.1063/1.1713411`.

[95] J. I. Mackenzie. Dielectric solid-state planar waveguide lasers: A review. *IEEE Journal of Selected Topics in Quantum Electronics*, 13(3):626–637, 2007. ISSN 1077-260X. doi: 10.1109/JSTQE.2007.897184.

[96] K. L. Schepler, R. D. Peterson, P. A. Berry, and J. B. McKay. Thermal effects in Cr^2+:ZnSe thin disk lasers. *Ieee Journal of Selected Topics in Quantum Electronics*, 11(3):713–720, 2005. ISSN 1077-260X. doi: 10.1109/jstqe.2005.850570. URL `https://www.cambridge.org/core/journals/journal-of-materials-research/article/crystallization-kinetics-of-binary-borosilicate-glass-composite/16FD8DB9DB5082611F21F3EAE0998E1E`.

[97] I. Shoji, Y. Okuyama, H. Ichikawa, Y. Ariga, and T. Onda. Laser characteristics of Nd:YAG/diamond and Nd:YVO4/diamond composite devices fabricated with the room-temperature-bonding technique. In *Advanced Solid State Lasers*, OSA Technical Digest (online), page ATh2A.14. Optical Society of America. doi: 10.1364/ASSL.2015.ATh2A.14. URL `https://www.osapublishing.org/abstract.cfm?URI=ASSL-2015-ATh2A.14`.

[98] J. Liang, S. Masuya, M. Kasu, and N. Shigekawa. Realization of direct bonding of single crystal diamond and Si substrates. *Applied Physics Letters*, 110(11):111603, 2017. doi: 10.1063/1.4978666. URL `http://aip.scitation.org/doi/abs/10.1063/1.4978666`.

[99] D. J. Pickrell, K. A. Kline, and R. E. Taylor. Thermal expansion of polycrystalline diamond produced by chemical vapor deposition. *Applied Physics Letters*, 64(18):2353–2355, 1994. doi: 10.1063/1.111612. URL `http://aip.scitation.org/doi/abs/10.1063/1.111612`.

[100] C-H. Su, S. Feth, and S. L. Lehoczky. Thermal expansion coefficient of ZnSe crystal between 17 and 1080°c by interferometry. *Materials Letters*, 63(17):1475–1477, 2009. ISSN 0167-577X. doi: http://dx.doi.org/10.1016/j.matlet.2009.03.050. URL `http://www.sciencedirect.com/science/article/pii/S0167577X09002638`.

[101] H. G. Stenhouse, S. J. Beecher, and J. I. Mackenzie. Direct bonding diamond to zinc selenide. *Optical Materials Express*, 7(8):2922–2927, 2017. ISSN 2159-3930. doi: 10.1364/ome.7.002922. URL `https://www.osapublishing.org/ome/abstract.cfm?URI=ome-7-8-2922`.

Publication list

1. H. Stenhouse, S. Beecher, and J. Mackenzie, “Direct bonding diamond to zinc selenide,” Opt. Mater. Express 7, 2922-2927 (2017).
2. H. Stenhouse, S. Beecher, and J. Mackenzie, “Direct Bonding Nd:YAG to Sapphire Wafers,” in Laser Congress 2017 (ASSL, LAC), OSA Technical Digest (online) (Optical Society of America, 2017), paper JM5A.3.
3. H. Stenhouse, S. Beecher, and J. Mackenzie, “Direct Bonding CVD-Grown Diamond to ZnSe and Sapphire,” in Laser Congress 2017 (ASSL, LAC), OSA Technical Digest (online) (Optical Society of America, 2017), paper AW3A.6.

Awards

IPG Best Student Oral Presentation Award “Direct Bonding CVD-Grown Diamond to ZnSe and Sapphire,” in Laser Congress 2017 (ASSL, LAC) - October 2017.